

PURDUE UNIVERSITY
GRADUATE SCHOOL
Thesis/Dissertation Acceptance

This is to certify that the thesis/dissertation prepared

By Keith Cameron Smith

Entitled

Coupled Dynamic Analysis of Flow in the Inlet Section of a
Wave Rotor Constant Volume Combustor

For the degree of Master of Science in Mechanical Engineering

Is approved by the final examining committee:

M. Razi Nalim

Chair

Likun Zhu

Jian Xie

To the best of my knowledge and as understood by the student in the *Research Integrity and Copyright Disclaimer (Graduate School Form 20)*, this thesis/dissertation adheres to the provisions of Purdue University's "Policy on Integrity in Research" and the use of copyrighted material.

Approved by Major Professor(s): M. Razi Nalim

Approved by: M. Razi Nalim

Head of the Graduate Program

11/10/2011

Date

**PURDUE UNIVERSITY
GRADUATE SCHOOL**

Research Integrity and Copyright Disclaimer

Title of Thesis/Dissertation:

Coupled Dynamic Analysis of Flow in the Inlet Section
of a Wave Rotor Constant Volume Combustor

For the degree of Master of Science in Mechanical Engineering

I certify that in the preparation of this thesis, I have observed the provisions of *Purdue University Executive Memorandum No. C-22, September 6, 1991, Policy on Integrity in Research*.*

Further, I certify that this work is free of plagiarism and all materials appearing in this thesis/dissertation have been properly quoted and attributed.

I certify that all copyrighted material incorporated into this thesis/dissertation is in compliance with the United States' copyright law and that I have received written permission from the copyright owners for my use of their work, which is beyond the scope of the law. I agree to indemnify and save harmless Purdue University from any and all claims that may be asserted or that may arise from any copyright violation.

Keith Cameron Smith

Printed Name and Signature of Candidate

11/10/2011

Date (month/day/year)

*Located at http://www.purdue.edu/policies/pages/teach_res_outreach/c_22.html

COUPLED DYNAMIC ANALYSIS OF FLOW IN THE INLET SECTION
OF A
WAVE ROTOR CONSTANT VOLUME COMBUSTOR

A Thesis
Submitted to the Faculty
of
Purdue University
by
Keith Cameron Smith

In Partial Fulfillment of the
Requirements for the Degree
of
Master of Science in Mechanical Engineering

December 2011
Purdue University
Indianapolis, Indiana

For my wife and children.

ACKNOWLEDGMENTS

Many thanks to Dr. M. Razi Nalim for his patience and direction. Thanks also to my colleagues, Purdue University Zucrow Labs, and to Rolls Royce LiberyWorks for access to the rig test data and drawings.

TABLE OF CONTENTS

	Page
LIST OF TABLES	vi
LIST OF FIGURES	vii
LIST OF SYMBOLS	x
ABSTRACT	xi
1 INTRODUCTION	1
1.1 Background	1
1.2 Rolls-Royce Test Rig Description	5
1.3 NASA Combustion Wave Rotor Computer Software	11
1.4 Experimental Test Description	16
1.5 VOLDYN - WRCVC Rig Computer Model Description	18
2 DEVELOPMENT OF THE LUMPED VOLUME DYNAMIC MODEL	21
2.1 Finite Difference Equations	21
2.2 Continuity Equation	23
2.3 Energy Equation	25
2.4 Inlet Air, Nitrogen, and Fuel Flows	27
2.5 Pressure Loss Computation	28
2.6 Exit Flow Characteristic	33
2.7 Lumped Volume Dynamic Model Validation	34
3 NON-DIMENSIONAL FLOW CHARACTERISTIC OF THE WRCVC	38
3.1 Software Modifications for Iteration	38
3.2 Software Modifications for Pressure Sweep	40
3.3 Software Modifications for All other Purposes	45
3.4 SCW1D Sweep Results	47
4 TIMING ANALYSIS OF THE INLET SECTION AND WRCVC ROTOR	60
4.1 Inlet Section Volume Timing Analysis	60
4.2 WRCVC Rotor Timing Analysis	61
5 DYNAMIC MODEL CONSTRUCTION AND EXECUTION	62
5.1 Dynamic Model Construction	62
5.2 Dynamic Model Initialization	62
5.3 Dynamic Model Volume Computation	65
5.4 Dynamic Model Execution	67
5.5 Dynamic Model Results	72

	Page
5.5.1 Airflow Comparison Results	72
5.5.2 Pressure Comparison Results	78
5.5.3 WRCVC Operation Results	92
6 CONCLUSIONS	99
LIST OF REFERENCES	102
APPENDICES	
A EXAM51 COMPUTER PROGRAM LISTING	105
B SUMMARY OF Z. LIGHTNER REFERENCE PAPER	108
VITA	111

LIST OF TABLES

Table	Page
1.1 Test O run 5 fuel configuration.	9
1.2 Analysis pressures tabulated in Elharis (2010).	10
1.3 Test O run 5 timings.	17
3.1 WRCVC rig geometry parameters.	48
3.2 WRCVC non-dimensional input parameters.	49
5.1 Lumped volume dynamic model working stations.	62
5.2 Volume computations for WRCVC rig.	66
5.3 Lumped volume dynamic model execution steps.	67
5.4 VOLDYN computed pressure loss values.	82
Appendix Table	
B.1 Table 7: Non-dimensional mass flow rates.	109
B.2 Table 8: Actual mass flow rates in lbm/sec.	109

LIST OF FIGURES

Figure	Page
1.1 Allison J33 turbojet engine with centrifugal compressor and can combustors.	2
1.2 North American F86E with J47-GE-13 engine.	3
1.3 Rolls-Royce WRCVC high pressure inlet airflow piping (courtesy of Purdue Zucrow combustion laboratories).	6
1.4 Rolls Royce WRCVC rig cross section (courtesy Rolls Royce).	7
1.5 Rolls Royce WRCVC rig fuel delivery section (courtesy Rolls Royce).	8
1.6 Simplified graphic of the VOLDYN control volume.	19
2.1 Drag coefficient - cylinder in crossflow.	31
2.2 EXAM51 model validation results.	37
3.1 High level flowchart for WRCVC cycle computation.	39
3.2 Modified flowchart for SCW1D main program.	40
3.3 Flowchart for RDINPT input subroutine.	41
3.4 Flowchart for FTPSIM solution subroutine.	42
3.5 Flowchart for SCW1D main program, modified for pressure sweep. . .	44
3.6 WRCVC Cold flow condition temperature, density, fuel fraction for the nominal inlet pressure. (A) Inlet opening, normalized to zero angle. (B) Inlet closing. (C) Exhaust opening. (D) Exhaust closing. (1) Expansion fan caused by exhaust opening. (2) Compression wave caused by inlet opening. (3) Hammer shock from exhaust closing. (4) Reflected hammer shock from left end wall. (5) Reflected hammer shock from right end wall.	51
3.7 WRCVC Torch On condition temperature, density, fuel fraction for the nominal inlet pressure.	52
3.8 WRCVC Torch Lit condition temperature, density, fuel fraction for the nominal inlet pressure. (1),(2) Torch location.	53
3.9 WRCVC Firing condition temperature, density, fuel fraction for the nominal inlet pressure. (1) Combustion zone.	54

Figure	Page
3.10 Cold flow sweep results - SCW1D output vs 5th order polyfit.	55
3.11 Torch on sweep results - SCW1D output vs 5th order polyfit.	56
3.12 Torch lit sweep results - SCW1D output vs 5th order polyfit.	57
3.13 Firing condition sweep results - SCW1D output vs 2nd order polyfit. . .	58
3.14 Sweep comparison - polyfit results at conditions.	59
5.1 Lumped volume dynamic model stations 0, 1, and 2.	63
5.2 Lumped volume dynamic model stations 3, 4, and 5.	64
5.3 WRCVC rig venturi upstream stagnation pressure.	68
5.4 WRCVC rig venturi upstream stagnation temperature.	69
5.5 WRCVC rig fuel rail pressure.	71
5.6 WRCVC rig venturi flow rates.	73
5.7 WRCVC rig venturi flow rates - detailed.	74
5.8 VOLDYN Computed mass flow imbalance.	75
5.9 VOLDYN Computed mass flow imbalance - detailed view.	76
5.10 VOLDYN Computed mass flow imbalance - micro view.	77
5.11 VOLDYN computed volume average pressure PS2, and stations 3, 4, and 5 stagnation pressures.	79
5.12 VOLDYN Computed drag forces.	80
5.13 VOLDYN Computed drag losses.	81
5.14 WRCVC rig station 3 stagnation pressure.	83
5.15 WRCVC rig station 3 stagnation pressure - detailed.	84
5.16 WRCVC Cold Flow condition temperature, density, fuel fraction for the nominal inlet pressure, with fuel delivery on.	85
5.17 WRCVC Cold Flow condition temperature, density, fuel fraction for the actual inlet pressure during fuel burp segment.	86
5.18 WRCVC Firing condition temperature, density, fuel fraction for the actual operating inlet pressure.	88
5.19 WRCVC rotor speed vs rig time.	90
5.20 RPM dependent pressure-flow characteristics.	91

Figure	Page
5.21 VOLDYN computation of WRCVC flow vs time.	93
5.22 VOLDYN computation of WRCVC flow vs time - detailed.	94
5.23 VOLDYN computed non-dimensional WRCVC inlet pressure vs time.	95
5.24 VOLDYN computed non-dimensional WRCVC inlet pressure vs time - detailed.	96
5.25 WRCVC Firing condition temperature, density, fuel fraction for the actual operating inlet pressure.	97
5.26 VOLDYN computation of flow vs inlet pressure.	98
Appendix Figure	
B.1 Figure 12: Channel mass flow for various pressure ratios.	110

LIST OF SYMBOLS

Symbol	Units	Description
A	in^2	Cross section area
a	ft/s	Sonic velocity
c_p	$(ft \cdot lb_f)/(lb_m \cdot ^\circ R)$	Specific heat at constant pressure
c_v	$(ft \cdot lb_f)/(lb_m \cdot ^\circ R)$	Specific heat at constant volume
e	$(ft \cdot lb_f)/(lb_m)$	Total energy per unit mass
γ		Specific heat ratio
g_c	$(ft \cdot lb_m)/(lb_f \cdot s^2)$	Gravitational conversion constant = 32.174
g_l	in/ft	Length unit conversion constant = 12
h	$(ft \cdot lb_f)/(lb_m)$	Enthalpy (local)
H	$(ft \cdot lb_f)/(lb_m)$	Enthalpy (total)
M		Local Mach number V/a
m	lb_m	Mass (typically mass in the control volume)
\dot{m}	lb_m / s	Mass flow
p	lb_f/in^2	Pressure (static pressure)
P	lb_f/in^2	Stagnation pressure (total pressure)
R	$(ft \cdot lb_f)/(lb_m \cdot ^\circ R)$	Gas constant
ρ	lb_m/m^3	Density
t	s	Time
T_s	$^\circ R$	Temperature (static temperature)
T_t	$^\circ R$	Stagnation temperature (total temperature)
u	$(ft \cdot lb_f)/(lb_m)$	Internal energy
\vec{u}, V	ft/s	Velocity (1-D, Scalar)
\mathcal{V}	m^3	Volume
y		Cross flow injection angle cosine

ABSTRACT

Smith, Keith C. M.S.M.E., Purdue University, December 2011. Coupled Dynamic Analysis of Flow in the Inlet Section of a Wave Rotor Constant Volume Combustor. Major Professor: M. Razi Nalim.

A wave rotor constant volume combustor (WRCVC) was designed and built as a collaborative work of Rolls Royce LibertyWorks, Indiana University-Purdue University at Indianapolis (IUPUI), and Purdue University, and ran experimental tests at Purdue's Zucrow Laboratories in 2009.

Instrumentation of the WRCVC rig inlet flow included temperature and pressure transducers upstream of the venturi and at the fuel delivery plane. Other instrumentation included exhaust pressures and temperatures. In addition, ion sensors, dynamic pressure sensors, and accelerometers were used to instrument the rotating hardware. The rig hardware included inlet guide vanes directly in front of the rotating hardware, which together with concern for damage potential, prevented use of any pressure transducers at the entrance to the rotor. For this reason, a complete understanding of the conditions at the WRCVC inlet is unavailable, requiring simulations of the WRCVC to estimate the inlet pressure at a specific operating condition based on airflow.

The operation of a WRCVC rig test is a sequence of events over a short time span. These events include introduction of the main air flow followed by time-sequenced delivery of fuel, lighting of the ignition source, and the combustion sequence. The fast changing conditions in the rig inlet hardware make necessary a time-dependent computation of the rig inlet section in order to simulate the overall rig operation.

The chosen method for computing inlet section temperature and pressure was a time-dependent lumped volume model of the inlet section hardware, using a finite difference modified Euler predictor-corrector method for computing the continuity and energy equations. This is coupled with perfect gas prediction of venturi air and fuel flow rates, pressure drag losses at the fuel nozzles, pressure losses by mass addition of the fuel or nitrogen purge, friction losses at the inlet guide vanes, and a correlation of the non-dimensional flow characteristics of the WRCVC. The flow characteristics of the WRCVC are computed by varying the non-dimensional inlet stagnation pressure and the WRCVC's operational conditions, assuming constant rotational speed and inlet stagnation temperature.

This thesis documents the creation of a computer simulation of the entire WRCVC rig, to understand the pressure losses in the inlet system and the dynamic coupling of the inlet section and the WRCVC, so that an accurate prediction of the WRCVC rotor inlet conditions can be computed. This includes the computational development of the WRCVC upstream rig dynamic model, the background behind supporting computations, and results for one test sequence. The computations provide a clear explanation of why the pressures at the rotor inlet differ so much from the upstream measured values. The pressure losses correlate very well with the computer predictions and the dynamic response tracks well with the estimation of measured airflow. A simple Fortran language computer program listing is included, which students can use to simulate charging or discharging of a container.

1. INTRODUCTION

1.1 Background

A wave rotor constant volume combustor (WRCVC) was designed and built as a collaborative work of Rolls Royce LibertyWorks, Indiana University-Purdue University at Indianapolis (IUPUI), and Purdue University. Initial experimental tests on the WRCVC were carried out successfully at Purdue's Zucrow Laboratories in 2009. Alparslan [1] described the WRCVC design and the cycle employed by the rotating hardware. Matsutomi [2] described the WRCVC rig hardware, focusing mostly on the drive assembly, the air systems, the ignition source, and the data acquisition and control systems. Elharis [3] further elaborated on the aerothermal design and provided the model validation of the rig. This WRCRV rig has also been the subject of other papers including a detailed experimental investigation paper by Matsutomi [4] and an analysis of the deflagrative combustion process by Elharis et al. [5].

A WRCVC differs significantly from the combustors used in popular jet aircraft engines in its operation and in its efficiency. The combustor in a jet aircraft engine has evolved over decades, beginning with the "can" design used in both centrifugal compressor engines such as the Allison J33 seen in Figure 1.1 [6] and axial compressor engines, from the early J35 through the very popular J79 engines. These combustors had very poor combustion efficiency, as documented in Graves [7], which could be seen as smoke from unburned fuel on takeoff in Figure 1.2 [8].

Development of more efficient combustors, including annular designs and can-annular (hybrid) designs, began in parallel with can type combustors, with early testing showing significantly higher combustion efficiency, as seen in Zettle [9]. It is possible in modern combustors to achieve nearly 100 percent combustion efficiency,



Figure 1.1. Allison J33 turbojet engine with centrifugal compressor and can combustors.

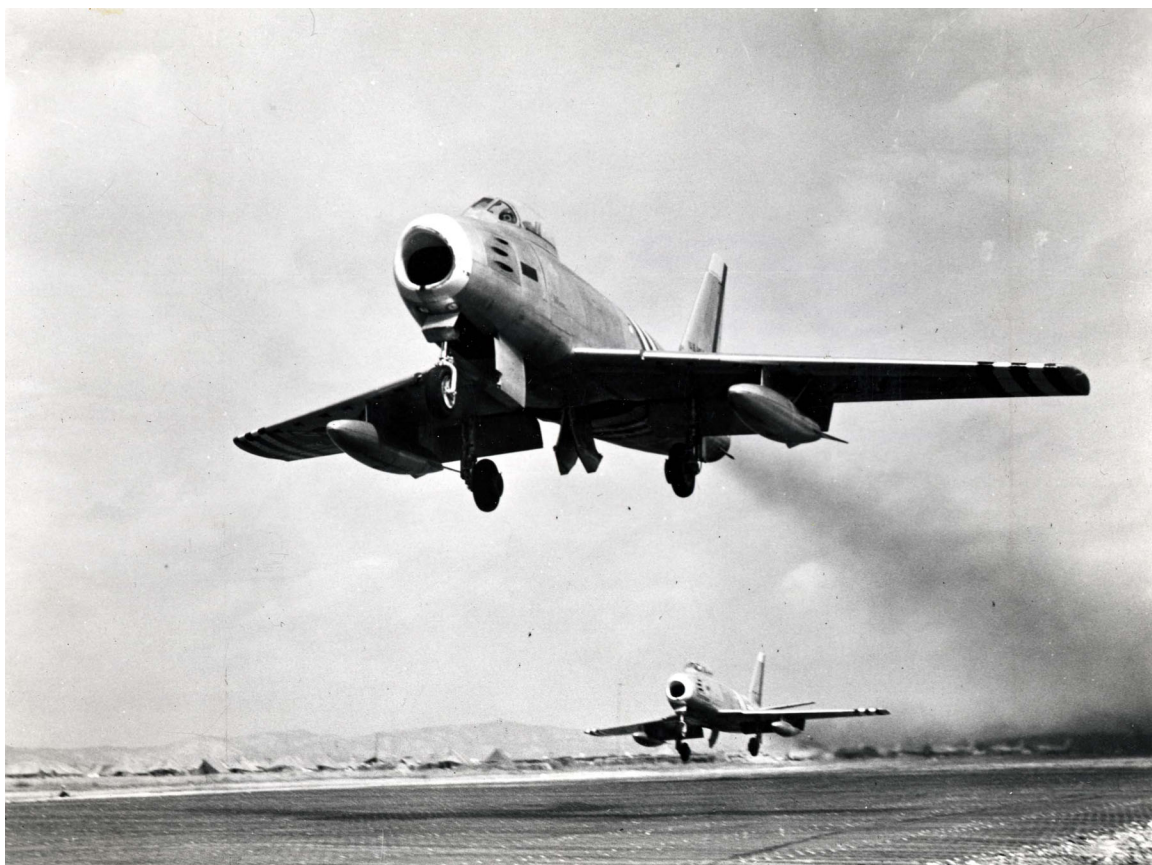


Figure 1.2. North American F86E with J47-GE-13 engine.

meaning that the fuel is completely burned. However, a more fundamental limitation is that all constant-pressure combustors penalize the engine cycle efficiency, because they inherently fail to capture the full work potential of the energy released by combustion of the fuel.

In contrast, a pressure gain combustor, which ideally approximates a constant volume combustion process, the same heat addition is accompanied by a pressure increase. The efficiency benefits of a pressure gain combustor over a constant pressure combustor can be seen in Li [10], which showed a significant increase in overall thermal efficiency for a gas turbine cycle, and in Nalim [11], which showed a significant specific impulse gain at low Mach numbers for a ramjet application.

The WRCVC design mechanically produces a constant volume combustion chamber, by capturing the fuel-air mixture into a flow channel and then blocking the ends of that channel. With proper hardware design, an additional pressure increase of the cold air charge can be seen, and is the main purpose of some wave rotor designs. This second application of the wave rotor has been proposed for use in gas turbine topping cycles, as seen in studies of the Wave Rotor compressor, summarized in Akbari [12]. A third possible application for the wave rotor is to transfer pressure between two flows, such as the exhaust and inlet flows of a piston type internal combustion engine. A modern example of this is the Mazda Compres compressor as described in Akbari [12].

Similar to the wave rotor constant volume combustor cycle is the Otto Cycle internal combustion cycle. An Otto Cycle engine uses a mechanical device, the moving piston, to produce, in theory, a constant volume combustion process, although at high piston speeds the combustion volume is constantly changing. By contrast, a well designed WRCVC should be smaller and lighter than a traditional internal combustion engine of the same power.

Two possible uses for a more thermally efficient combustion process could be stationary generation or flight worthy engines. A perceived lower cost of the WRCVC for use in a transonic ramjet missile, as opposed to the cost of a small turbojet engine, could be an economic driver for WRCVC development.

1.2 Rolls-Royce Test Rig Description

The Rolls-Royce WRCVC test rig hardware was built to support the operation of the WRCVC. The rig supplied the base and drive assembly to spin the WRCVC rotor, a propane-based torch igniter to light the fuel-air mixture in the WRCVC, high pressure air, ethylene fuel, nitrogen purge, and data acquisition systems, as described in Matsutomi [2]. The WRCVC exhaust port was open to atmosphere without any attempt for pressure recovery. In Figure 1.3, the venturi and high pressure inlet airflow piping can be seen in relation to the WRCVC hardware. In Figure 1.4, the rig air inlet, transition duct, fuel delivery area, flow straightener, and WRCVC inlet can be seen. In Figure 1.5, a front view of the fuel delivery area showing the fuel nozzles is shown. Table 1.1 gives detailed placement of the parts in the as-tested configuration. In the test run studied in this thesis, there were 9 fuel delivery tubes, three blanks, two pressure measurement tubes, and one thermocouple, for a total of 15 tubes blocking the flow.

A geometric analysis of the piping and inlet section hardware was performed for this thesis, resulting in a computation of the total volume of the airflow path. Details of this analysis are presented in Section 5.3 and Table 5.2. The total volume of the airflow path downstream of the airflow measurement venturi is used in the mathematical model of the air system. Instrumentation of the inlet section airflow consisted of temperature and pressure measurements upstream of the venturi and at the fuel nozzle plane, which is approximately 16 inches upstream of the WRCVC rotor inlet plane.

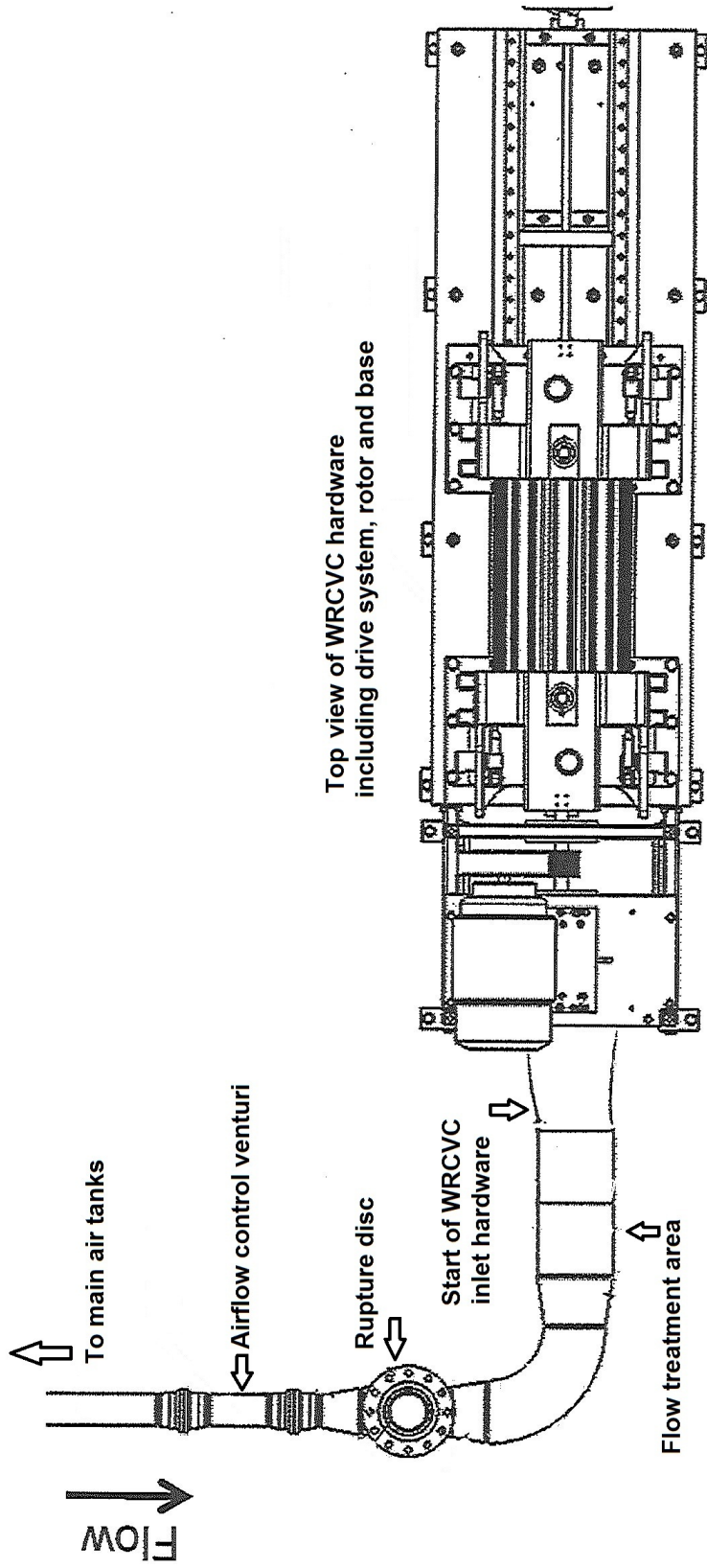


Figure 1.3. Rolls-Royce WRCVC high pressure inlet airflow piping (courtesy of Purdue Zucrow combustion laboratories).

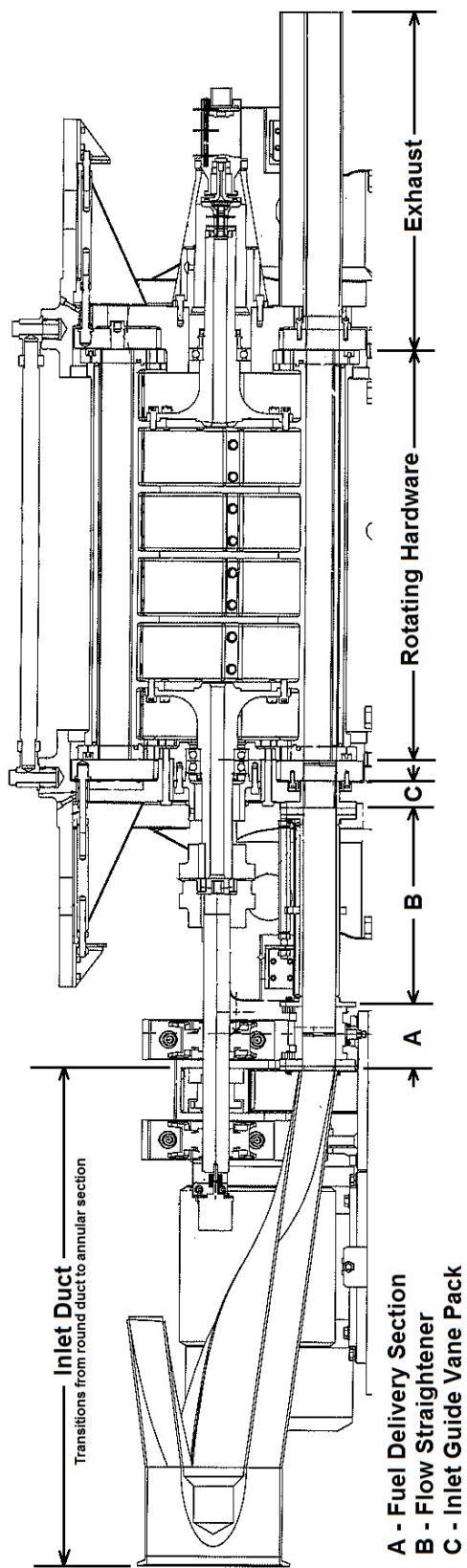


Figure 1.4. Rolls Royce WRCVC rig cross section (courtesy Rolls Royce).

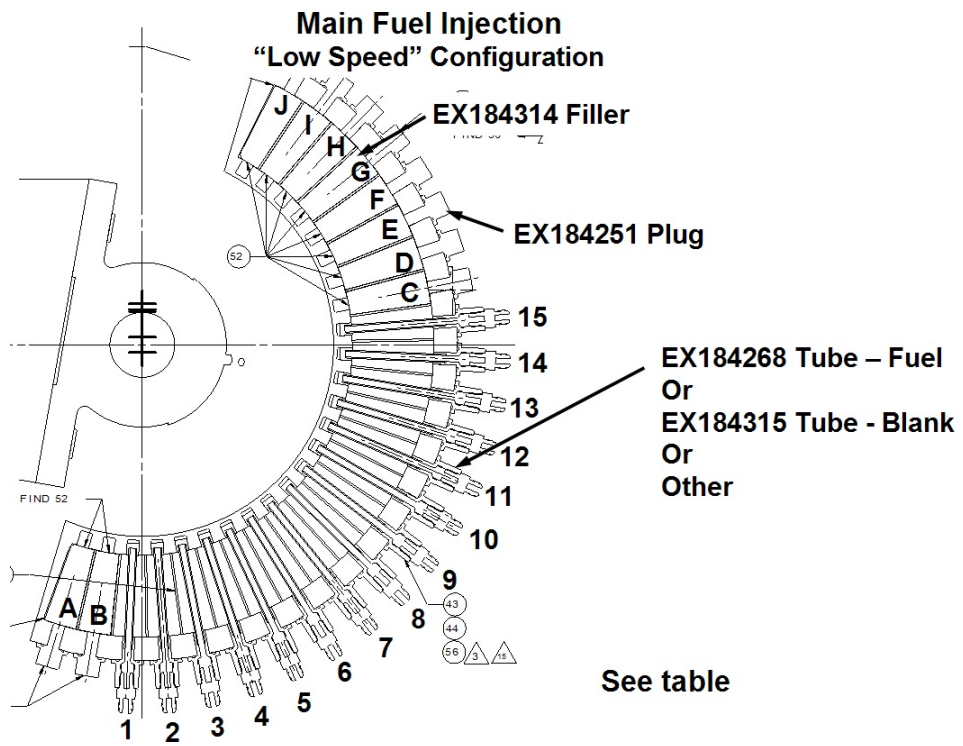


Figure 1.5. Rolls Royce WRCVC rig fuel delivery section (courtesy Rolls Royce).

Table 1.1 Test O run 5 fuel configuration.

Passage Number	EX184314 Filler	EX184251 Plug	EX184268 Fuel Tube	EX184315 Blank Tube	Other List Part Name
A	✓	✓			
B	✓	✓			
1					Inlet Total Press
2				✓	
3			✓		
4			✓		
5			✓		
6			✓		
7			✓		
8			✓		
9			✓		
10			✓		
11			✓		
12					Thermocouple
13				✓	
14				✓	
15					Inlet Total Press
C	✓	✓			
D	✓	✓			
E	✓	✓			
F	✓	✓			
G	✓	✓			
H	✓	✓			
I	✓	✓			
J	✓	✓			

Analyses of the WRCVC performance, including Elharis [3], Elharis [5], and Matsutomi [4], have used measured pressures for various purposes. The first of these analyses, Elharis [3], stated, “Boundary conditions at the rotor channel inlet and exit ends are needed for numerical simulations; however, the pressures and temperatures are not measured at the rotor faces, but at more distant locations. The boundary pressures for the intake and exit sides of the channel are estimated such that the intake mass flow rate in the simulation matches the measured mass flow supplied through the intake port.” This paper acknowledges the difference between the pressures measured at the fuel delivery plane and the pressures required to match airflow rates by computer software models of the WRCVC. The pressures tabulated in this paper are summarized in Table 1.2.

Table 1.2 Analysis pressures tabulated in Elharis (2010).

Reference	Condition	Measured Pressure (psi)	Correlated Pressure (psi)
Case A	Cold	21.23	19.3
	Torch	20.78	19.4
	Firing	20.17	18.4
Case B	Cold	21.52	19.4
	Torch	21.11	19.6
	Firing	20.77	18.5
Case C	Cold	20.08	18.5
	Failed Firing	19.76	18.4

The third of these papers, Matsutomi [4], displayed a time graph of the measured pressure at the fuel delivery plane, labeled “Inlet total pressure measurement.” This graph showed an increase in the measured pressure during the cold-flow fuel mass addition time period, and a decrease in the measured pressure during the firing time period, when the main fuel was burning. This paper stated, “The effect of fuel flow alone can be observed around 198 seconds in the plot. At this point, the fuel flow was activated prior to combustion to release any unwanted fuel accumulation in the fuel

plumbing. The fuel flow rate observed during this period was approximately the same as during the combustion test. During this period, the inlet total pressure increased approximately 1.0 psi from the nominal pressure due to the fuel injection.” The paper further discussed the effect of combustion on the inlet total pressure measurement.

The main purpose of this thesis is to present a time-dependent lumped volume computer simulation of the inlet section, coupled with the WRCVC, to explain both of these pressure observations. This computer simulation can be used in future rig test planning, to more closely predict the operating point of the WRCVC at a specific inlet operating pressure and temperature.

1.3 NASA Combustion Wave Rotor Computer Software

As mentioned in the previous section, analyses of the WRCVC performance have been performed, including Elharis [3] and Elharis [5]. The software used to perform these analyses is a derivative of software developed for generic wave rotor analysis, and documented in Paxson [13], [14], [15], [16], [17], and Nalim [18]. The original code developed by NASA is often referred to as the NASA quasi one-dimensional (Q1D) wave rotor code.

In the paper Paxson [15] the model description is provided in detail. The section regarding the Governing Equations for single passage gas dynamic modeling is repeated verbatim here for reference. For additional detail the referenced papers should be studied.

Governing Equations

The governing equations in the passages are assumed to be of the form

$$\frac{\partial \underline{w}}{\partial t} + \frac{\partial \underline{F}(\underline{w})}{\partial x} = \underline{S}(\underline{w}) \quad (1.1)$$

where

$$\underline{w} = \begin{bmatrix} \rho \\ \rho u \\ \left(\frac{p}{\gamma(\gamma-1)} + \frac{\rho u^2}{2} \right) \end{bmatrix} \quad (1.2)$$

and

$$\underline{F} = \begin{bmatrix} \rho u \\ \frac{p}{\gamma} + \rho u^2 \\ u \left(\frac{p}{\gamma-1} + \frac{\rho u^2}{2} \right) \end{bmatrix} \quad (1.3)$$

These equations have been non-dimensionalized using a reference state p^* , ρ^* , and a^* , where a^* is the speed of sound, and the ratio of specific heats, γ . In this form the perfect gas law may be written as $p = \rho T$. The distance has been scaled by the passage length, L , and the time has been scaled using the wave transit time, $\frac{L}{a^*}$. For all of the results to be presented, the reference state is the wave rotor inlet stagnation state (port 1 in Fig 1). The source vector $\underline{S}(\underline{w})$ accounts for viscous effects (i.e. friction), heat transfer from the passage walls to the gas, and leakage from the passages to the hollow center cavity of the rotor and to the ports. Leakage is assumed to occur only at the ends of any passage. Thus, for the intermediate region where there is no leakage the source vector may be written as

$$\underline{S}^{int} = \begin{bmatrix} 0 \\ \sigma_2 |\rho u|^{0.75} u \\ \frac{\sigma_2}{\gamma-1} \left(\frac{D_h}{2h} \right) Pr^{-\frac{2}{3}} (T - T_{wall}) |\rho u|^{0.75} \end{bmatrix} \quad (1.4)$$

where D_h is the passage hydraulic Diameter, h is the passage height, Pr is the Prandtl number, T is the gas static temperature, and T_{wall} is the passage wall temperature. The term σ_2 is a semi-empirically derived constant based on the passage geometry and reference conditions:

$$\sigma_2 = -5.448 \left(\frac{L}{D_h} \right)^{1.081} \left(\frac{\rho^* a^* L}{\mu} \right)^{-0.3953} \quad (1.5)$$

The dynamic viscosity is assumed constant. The third term of the source vector in Eqn. 4 (1.4) is derived from the Reynolds-Colburn heat transfer, skin friction analogy with heat transfer assumed to occur only from the upper and lower surfaces of the passage and not from the sides.

For the ends of the passage where leakage occurs, the source vector is written as

$$\underline{S}^{leak} = \underline{S}^{int} + \begin{bmatrix} -C_D \cdot \gamma_2 \left(\frac{2\delta_{leak}}{h\Delta x} \right) \sqrt{p\rho} \cdot f \left(\frac{p_{cav}}{p} \right) \\ 0 \\ -C_D \cdot \frac{\gamma_2}{(\gamma-1)} \left(\frac{2\delta_{leak}}{h\Delta x} \right) T^0 \sqrt{p\rho} \cdot f \left(\frac{p_{cav}}{p} \right) \end{bmatrix} \quad (1.6)$$

where the function $f \left(\frac{p_{cav}}{p} \right)$ is the well known St. Venant's orifice equation, p_{cav} is the pressure of the gas in the rotor center cavity, δ_{leak} is the gap between the rotor and casing endwall, Δx is the non-dimensional grid spacing used in the computational scheme to be described below (it is assumed that the leakage gap is much smaller than the grid spacing), $\gamma_2 = \sqrt{\frac{2}{\gamma-1}}$, T^0 is the gas stagnation temperature, and C_D is the seal discharge coefficient, assumed here to be 0.8. If the cavity pressure is greater than cell pressure then the pressure ratio in Eqn. 6 (1.6) is inverted, the sign changes, and p , ρ , and T^0 become those of the rotor center cavity.

Eqn. 1 (1.1) is integrated numerically using the following Lax-Wendroff technique described in Ref. 1:

$$\underline{w}_i^{n+1} = \underline{w}_i^n - \left(\underline{f}_{i+1/2}^n - \underline{f}_{i-1/2}^n \right) \frac{\Delta t}{\Delta x} + \underline{s}_i^n \Delta t \quad (1.7)$$

where the numerical flux estimate $\underline{f}_{i+1/2}^n$ is

$$\underline{f}_{i+1/2}^n = \frac{\underline{F}_{i+1}^n + \underline{F}_i^n}{2} - \frac{\Phi_{i+1/2}^{Roe}}{2} + \frac{\Delta t}{4} \left([A]_{i+1}^n \cdot \underline{S}_{i+1}^n + [A]_i^n \cdot \underline{S}_i^n \right) \quad (1.8)$$

and the numerical source \underline{s}_i^n is

$$\underline{s}_i^n = \frac{1}{2} (3 \cdot \underline{S}_i^n - \underline{S}_i^{n-1}) \quad (1.9)$$

The term $\underline{\Phi}_{i+1/2}^{Roe}$ in Eqn. 8 (1.8) refers to the flux limited dissipation based on Roe's approximate Riemann solver for equation 1 (1.1) without a source vector. The matrix $[A]$ is the Jacobian of the flux vector \underline{F} . The superscript n indicates the discrete temporal index $n\Delta t$, and the subscript i indicates the spacial index $i\Delta x$. Unless otherwise stated all results to be presented in this report used a ratio of $\frac{\Delta t}{\Delta x} = 0.3$, with $\Delta x = 0.02$. The leakage term, Eqn. 6 (1.6), is applied to the first and the last cell in the computing domain.

Paxson's paper also provides the method for computing the wall temperature for each computational cell of each passage using a lumped capacitance model, as well as a method for computing the center cavity gas state. These methods were refined in Paxson [16], presenting the same wall temperature computation with a heat flow schematic. Paxson's papers provide the equations for computing endwall leakage; this has been expanded in the current version to include computation of leakage between channels. Also in this latter Paxson paper, the effect of a finite opening time for the channel to the inlet flow was described, which is considered an improvement over the assumption of an instantaneous opening and closing of the passage. The version of SCW1D used for this thesis did not include the species computations used in Elharis [19].

The original software for analysis of wave rotor performance consists of three Fortran modules, encompassing the boundary condition computations, the Roe's characteristic scheme for the Euler equations, and the input/output/control software. In the original form, the software uses a fixed input and output format, and iteration is done by interactively specifying the normalized boundary pressures, temperatures, and rotor speed.

In order to increase the speed with which analyses can be performed, organizational changes to the original Fortran program were required. Changes to the program were made in order to increase the speed of computation, to improve the security of the data used by the program, to allow multiple paths of program development, to include conversion between physical properties and physical dimensions and non-dimensional inputs and outputs, and to execute the entire program as a subroutine of a larger control program. In addition, minor changes were made so that the program compiles using the latest Fortran compiler. All of these changes were made to the program and the program was validated against existing test cases. Finally, the program was put under configuration control to document and control revision changes to all modules. These changes are documented in Section 3.3.

Additional work on the program, performed by Dr. Razi Nalim and members of the IUPUI wave rotor group over the past 14 years, have been incorporated into the actual functional portions of the code, in order to improve the accuracy of the program.

The current version of the program, with the changes mentioned, is being used by Indiana University-Purdue University at Indianapolis (IUPUI) for analysis and design efforts, and is referred to as the SCW1D program (Simulation of Combustion & Waves - 1D). Other works have been performed using derivatives of this program, including Elharis [19].

1.4 Experimental Test Description

The experimental test runs were carefully planned with precise timings for main air flow, nitrogen purge, ethylene fuel and propane torch igniter operation. Main air flow is a term used by the combustion laboratories to indicate the main working gas of the test article. Timings were chosen to allow stabilization of the main airflow, to ensure safe operation of the WRCVC, and to gather accurate test data for a short firing of the WRCVC. Main inlet airflow was controlled by a venturi as seen in Figure 1.3. Fuel and nitrogen purge flows were controlled by using pre-set pressures for the delivery systems. Each test was governed by a Test Operations Request (TOR) which detailed the rig configuration and the timings for the air, fuel, purge, and torch systems.

The specific test run evaluated by this thesis, characterized as Test O Run 5, was performed on Sept 30, 2009. The main airflow set point was achieved by upstream venturi pressures of approximately 160 psia, with airflow governed primarily by the upstream pressure and the calibrated venturi area. Testing protocol began with a spin-up of the rotor to a constant rotor speed which was held to virtually the same speed throughout the test. Stagnation pressures upstream of the venturi and at the fuel plane were recorded, as well as stagnation temperatures. After the rotor had achieved its set speed point, a sequence of mass flows were initiated at time set points as seen in the testing data. Table 1.3 shows the timing sequence of flows and igniter firings of Test O Run 5.

Use of a calibrated venturi for flow metering improves the certainty of the air flow measurement. After the initial couple of seconds, the venturi is choked, which makes the main air flow rate primarily proportional to the upstream pressure. Holding the pressure constant keeps the airflow constant until the tank temperature starts to drop, which is seen near the end of each test. This temperature drop is caused by the

Table 1.3 Test O run 5 timings.

Number/Type	Event	Time, sec	Value	Condition
1D	Main air isolation valve	-	HIGH	Cold
2D	Motor main switch control	1.0	HIGH	Cold
3A	Start spinning the motor	5.0	2100 rpm	Cold
4A	Start main air flow	80.0	175 psia	Cold
5D	Start N2 purge in main fuel	194.0	HIGH	Cold
6D	HF DAQ control	195.0	HIGH	Cold
7D	Burp torch fuel	197.0	HIGH	Cold
8D	Burp main fuel	197.0	HIGH	Cold
9D	Burp main fuel	198.5	LOW	Cold
10D	Burp torch fuel	202.0	LOW	Cold
11D	Torch air fire valve	203.0	HIGH	Torch On
12D	Torch spark	208.5	HIGH	Torch Lit
13D	Torch fuel fire valve	209.0	HIGH	Torch Lit
14D	Torch spark	212.5	LOW	Torch Lit
15D	Main fuel open	214.0	HIGH	Firing
16D	Gas sampling valve open	214.4	HIGH	Firing
17D	Main fuel close	215.0	LOW	Torch Lit
18D	Gas sampling valve close	215.2	LOW	Torch Lit
19D	Main air isolation valve	229.0	LOW	Cold
20A	Main air flow off	229.0	0 psia	Cold
21A	Stop spinning the motor	232.0	0 rpm	Cold
22D	HF DAQ control	233.0	LOW	Cold
23D	Motor main switch control	233.0	LOW	Cold

transient flow pulling flow work from the tank, in much the same way as a propane tank becomes cold when it is used.

Nitrogen purge flow is used to prevent residual presence of ethylene fuel in the fuel nozzles when the fuel supply is turned off. Because the nitrogen purge pressure is lower than the fuel pressure, when fuel flow is on, a check valve stops the nitrogen flow, and when the fuel flow is stopped, the nitrogen flow resumes, clearing the fuel nozzles of any residual fuel. During ethylene fuel operation, the check valve prevents ethylene gas from backflowing into the nitrogen purge system.

1.5 VOLDYN - WRCVC Rig Computer Model Description

The VOLDYN computer program, the main tool developed and used for this thesis, was developed to simulate the WRCVC rig inlet section volume dynamics, the pressure losses associated with fuel injection, fuel nozzle blockage, friction losses associated with the flow straightener walls and inlet guide vanes, and to simulate the time-dependent mass flow characteristic of the WRCVC, explained as changes in the WRCVC “pumping effect” in Matsutomi [4] page 8. The VOLDYN program uses a finite difference, modified Euler predictor-corrector method for time integration of the continuity and energy equations, including the time dependent injection of mass flows, to compute the lumped volume properties of a single volume. For this work this single volume is the rig inlet section, starting at the venturi and ending at the WRCVC rotor inlet, as seen in the simplified graphic in Figure 1.6. This method of time dependent flow analysis has been used by industry to predict the dynamic response of engine systems, including Drummond [20]. The author also has developed similar simulations, incorporating the momentum equation, for multiple volume simulation of the GE XF120 gas generator stall simulation program (unpublished). The VOLDYN program uses perfect gas relations to simulate pressure losses downstream of the flow treatment section. In order to properly simulate rig operation in real time, the rig model computes inlet air flow, nitrogen purge flow, and ethylene fuel flow rates based on measured stagnation pressure and stagnation temperature of each gas. Main air, nitrogen purge, and ethylene fuel flow values are computed using perfect gas relations, based on the time dependent measurements of upstream pressure. The rig exit airflow rate is computed from maps generated of the WRCVC operating at a single specified rotational speed and varying inlet pressure, yielding polynomial equations for non-dimensional airflow value as a function of inlet pressure.

The VOLDYN program computes working fluid conditions at specified points in the flow stream, using an industry standard technique of assigning “station” numbers to specific flow boundaries, and computing thermodynamic processes between these

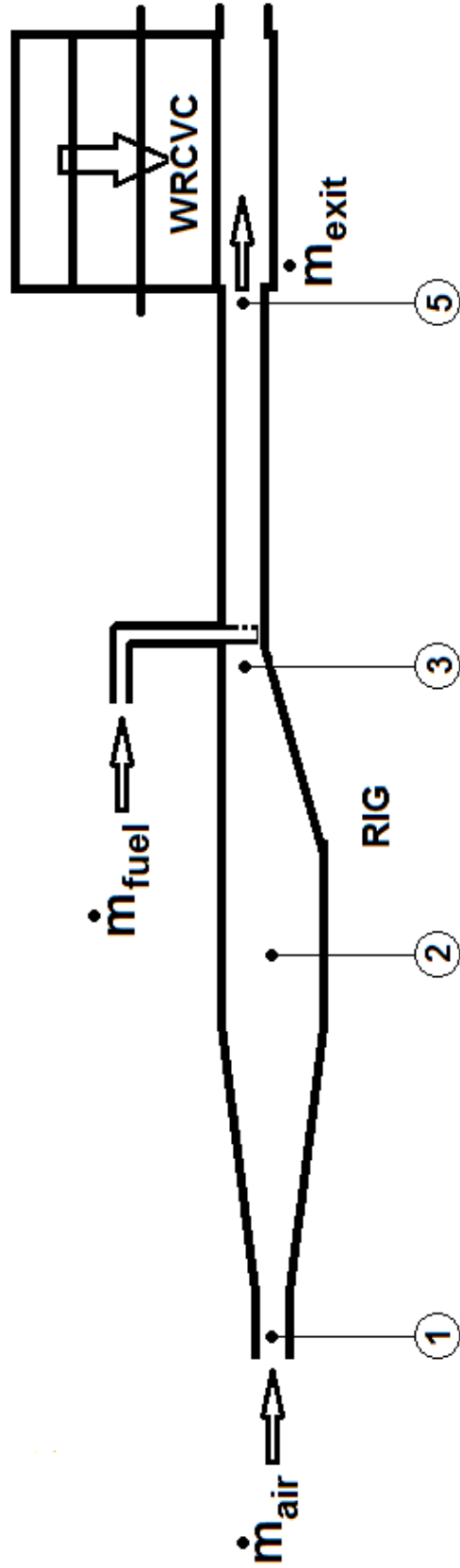


Figure 1.6. Simplified graphic of the VOLDYN control volume.

boundaries using perfect gas relations or real gas relations. The industry standard NPSS program uses this method for simple cycle modeling [21]. As described above, the inlet flows are computed using steady one-dimensional flow of perfect gas equations, which can be applied to dynamically changing flows even if the backpressure is changing rapidly, unless the flow unchokes.

Pressure loss computations are based on standard correlations of pressure drag based on correlations found in Hoerner [22] and Incropera [23]. Losses from introduction of fuel crosswise to the flow stream are based on ideal gas relations with computations found in Zucrow & Hoffman [24]. These pressure losses are detailed in Section 2.5.

2. DEVELOPMENT OF THE LUMPED VOLUME DYNAMIC MODEL

2.1 Finite Difference Equations

A general description of the lumped volume model is that it is a time-dependent solution of initial-value ordinary differential equations (ODEs), which Hoffman [25] describes as propagation problems. Hoffman's textbook describes many methods for solving propagation problems. Chapter 7 in this text describes a finite difference method, quoting, "transforming the calculus problem into an algebraic problem by

1. *Discretizing* the continuous physical domain
2. *Approximating* the exact derivatives in the ODE by algebraic finite difference approximations (FDAs)
3. *Substituting* the FDAs into the ODE to obtain an algebraic finite difference equation (FDE)"

Hoffman describes the numerical solution of initial value ODEs using the term "marching" methods. The calculus equations used in the development of the computer simulation in this thesis are the Navier-Stokes continuity and energy equations. The sections in this chapter describe the discretization of these two equations, the approximation used to create the FDAs, and the final FDEs used for the computer simulation. In addition, the problem domain for the WRCVC inlet section is one where the initial values are time dependent as well, making each time step require a re-evaluation of the inputs.

For all unsteady solutions of fluid dynamics problems, discretization must be performed in the temporal (time) and spacial (physical) dimensions. The temporal discretization of this problem is dependent on the time analysis of the inlet section as

seen in Sections 4.1 and 4.2. Because of nature of the problem to be solved, the size of the inlet section volume and its ability to accumulate mass and energy, the spacial discretization can be reduced to a single volume. Use of a single, fixed control volume reduces the spacial discretization in the equations to the overall volume measurement. Time discretization of unsteady solutions is generally a trade-off between the time difference required for stability (values too large will cause the computation to be unstable) and the time difference required for reasonable run times (values too small will cause the system to use excessive computer time).

The method employed for this thesis is the Modified Euler Predictor-Corrector Method, as described in Section 2.2. The error term for this method is of order

$$\epsilon \propto O(\Delta t^3) \quad (2.1)$$

For this thesis, this error term is minimized by setting the Δt value to 20 microseconds ($20\mu s$). The data acquisition system obtained data in 2 millisecond (ms) increments. Use of a 20 microsecond time step reduces the error over use of a 2 millisecond time step by 6 orders of magnitude. An error in the computation could also be caused by the spacial discretization and ignoring the pressure losses upstream of the flow treatment section. Further study could be accomplished by increasing the number of volumes, but this would require introduction of the momentum equation, adding an additional FDE and requiring different numerical methods. Section 4.2 describes the timing of the wave rotor cycle. The WRCVC rotor period of $28.6ms$ is approximately ten times the data measurement period and approximately 1000 times the VOLDYN computation period. For this reason the VOLDYN model assumes that the WRCVC conditions do not change during the Δt computation period.

2.2 Continuity Equation

The Continuity equation relates the increase of mass in a control volume based on the introduction of mass flows into the volume, balanced by mass flows exiting the volume. Over a specified increment of time, if the summed mass flows into the volume exceed the mass flows exiting, mass will accumulate in the volume. The integral equation for continuity is:

$$\int_{\mathcal{V}} \rho_t d\mathcal{V} + \int_A \rho \mathbf{V} \cdot d\mathbf{A} = 0 \quad (2.2)$$

Applying the integral form to a differential, one-dimensional control volume provides the differential form of the continuity equation:

$$\frac{\partial \rho}{\partial t} + \frac{\partial}{\partial x}(\rho \bar{u}) = 0 \quad (2.3)$$

Applying the integral form to the fixed rig volume \mathcal{V} gives the following finite difference approximation (FDA):

$$\frac{dm}{dt} = \sum \dot{m}_{in} - \sum \dot{m}_{out} \quad (2.4)$$

Accounting for the main air flow, fuel rail flow, exit flow, and making the assumption of no leakage flows leads to:

$$\mathcal{V} \frac{d\rho}{dt} = \dot{m}_{air} + \dot{m}_{fuel} - \dot{m}_{exit} \quad (2.5)$$

Which can be discretized as a time dependent relation of density over time:

$$(\rho \mathcal{V})_{t+\Delta t} = (\rho \mathcal{V})_t + (\dot{m}_{air} + \dot{m}_{fuel} - \dot{m}_{exit})\Delta t + (\text{higher order terms}) \quad (2.6)$$

Leading to the main iteration equation representing the change of density of the lumped volume for the next time step, a finite difference equation (FDE):

$$(\rho)_{t+\Delta t} = (\rho)_t + (\dot{m}_{air} + \dot{m}_{fuel} - \dot{m}_{exit}) \left(\frac{\Delta t}{\mathcal{V}} \right) \quad (2.7)$$

With units of:

$$\frac{lb_m}{ft^3} = \left(\frac{lb_m}{sec} \right) \cdot \frac{sec}{ft^3} \quad (2.8)$$

Since the main air pressure and fuel rail pressures were tabulated as a function of time, the inlet mass flows \dot{m}_{air} and \dot{m}_{fuel} could be evaluated at any value of time. The exit mass flow, as will be shown in Section 2.6, is a function of the volume density and pressure, shown as $f(\rho, p)$ and must be computed for time $t + \Delta t$. For this reason, evaluation of the FDE derivatives were evaluated using the mass flows at time step t and at time step $t + \Delta t$, and a Modified Euler Predictor-Corrector method was used to compute the value of $(\rho)_{t+\Delta t}$.

$$(g')_t = \frac{(\dot{m}_{air} + \dot{m}_{fuel} - \dot{m}_{exit})_t}{\mathcal{V}} \quad (2.9)$$

$$(\rho)_{t+\Delta t}^P = (\rho)_t + \Delta t \cdot (g')_t \quad (2.10)$$

$$(\dot{m}_{exit})_{t+\Delta t} = f((\rho)_{t+\Delta t}^P, (p)_{t+\Delta t}^P) \quad (2.11)$$

$$(g')_{t+\Delta t} = \frac{(\dot{m}_{air} + \dot{m}_{fuel} - \dot{m}_{exit})_{t+\Delta t}}{\mathcal{V}} \quad (2.12)$$

$$(\rho)_{t+\Delta t}^C = (\rho)_t + \frac{1}{2} \Delta t \left[(g')_t + (g')_{t+\Delta t} \right] \quad (2.13)$$

2.3 Energy Equation

The Energy equation relates the increase of the internal energy in a control volume based on the introduction of energy into the volume, balanced by energy exiting the volume. Over a specified increment of time, if the summed energy into the volume exceed the energy exiting, energy will accumulate in the volume. The integral equation for energy is:

$$\dot{W}_{shaft} + \dot{W}_{shear} - \dot{Q} + \int_{\mathcal{V}} \frac{\partial}{\partial t} \left[\rho \left(u + \frac{V^2}{2} + gz \right) \right] dV + \int_A \left(h + \frac{V^2}{2} + gz \right) (\rho \mathbf{V} \cdot d\mathbf{A}) = 0 \quad (2.14)$$

Applying the integral form to a differential, one-dimensional control volume, in the absence of heat transfer, work, and gravitational effects, provides the differential form of the energy equation:

$$\frac{\partial}{\partial t} \left(\rho e + \frac{\rho u^2}{2} \right) + \frac{\partial}{\partial x} \left(\rho e u + \frac{\rho u^2}{2} + up \right) = 0 \quad (2.15)$$

Applying the integral form to the fixed rig volume \mathcal{V} , in the absence of heat transfer, work, and gravitational effects, gives the following finite difference approximation (FDA):

$$\frac{d}{dt} (mu) = \sum \left[\dot{m} \left(h + \frac{V^2}{2} \right) \right]_{in} - \sum \left[\dot{m} \left(h + \frac{V^2}{2} \right) \right]_{out} \quad (2.16)$$

Summing the enthalpy and kinetic energy terms leads to:

$$\frac{d}{dt} (mu) = \sum (\dot{m}H)_{in} - \sum (\dot{m}H)_{out} \quad (2.17)$$

Applying the calorically perfect gas relation $H = c_p T_t$, applying the differential equation over a fixed time frame Δt , and accounting for the main inlet air flow, fuel rail flow, exit flow, and assuming no leakage, the equation can be written:

$$\frac{d(mu)}{dt} = (\dot{m}c_p T_t)_{air} + (\dot{m}c_p T_t)_{fuel} - (\dot{m}c_p T_t)_{exit} \quad (2.18)$$

The left hand relation can be reduced in the following fashion by the definition of mass $m = \rho \mathcal{V}$, applying the equation of state $p \mathcal{V} = \rho R T_s$, the definition of gas constant $R = c_p - c_v$ and of the specific heat ratio γ which is $\gamma = \frac{c_p}{c_v}$, leading to the relation between γ and the ratio $\frac{c_v}{R}$:

$$\gamma - 1 = \frac{c_p}{c_v} - \frac{c_v}{c_v} = \frac{R}{c_v} \quad (2.19)$$

and its reciprocal:

$$\frac{c_v}{R} = \frac{1}{\gamma - 1} \quad (2.20)$$

Substitution allows the value of (mu) to be related to temperature and pressure:

$$mu = mc_v T_s = \rho \mathcal{V} c_v T_s = \frac{p \mathcal{V} c_v}{R} = \frac{p \mathcal{V}}{(\gamma - 1)} \quad (2.21)$$

Leading to the following:

$$\frac{\mathcal{V}}{(\gamma - 1)} \frac{dp}{dt} = (\dot{m}c_p T_t)_{air} + (\dot{m}c_p T_t)_{fuel} - (\dot{m}c_p T_t)_{exit} \quad (2.22)$$

In this equation the value of pressure at a future time step Δt can be computed as a finite difference equation (FDE):

$$(p)_{t+\Delta t} = (p)_t + \left(\frac{(\gamma - 1)\Delta t}{g_t^2 \mathcal{V}} \right) \left[(\dot{m}c_p T_t)_{air} + (\dot{m}c_p T_t)_{fuel} - (\dot{m}c_p T_t)_{exit} \right] + (\text{higher order terms}) \quad (2.23)$$

With the length constant applied, the units are reconciled as follows:

$$\frac{lb_f}{in^2} = \frac{s}{\left(\frac{in^2}{ft^2} \cdot ft^3\right)} \cdot \left(\frac{lb_m}{sec} \cdot \frac{ft \cdot lb_f}{lb_m \cdot \circ R} \cdot \circ R\right) \quad (2.24)$$

Evaluation of the FDE derivatives were evaluated using the mass flows at time step t and at time step $t + \Delta t$, and a Modified Euler Predictor-Corrector method was used to compute the value of $(p)_{t+\Delta t}$.

$$(h')_t = \left(\frac{(\gamma - 1)}{g_l^2 \mathcal{V}}\right) \left[(\dot{m}c_p T_t)_{air} + (\dot{m}c_p T_t)_{fuel} - (\dot{m}c_p T_t)_{exit} \right]_t \quad (2.25)$$

$$(p)_{t+\Delta t}^P = (p)_t + \Delta t \cdot (h')_t \quad (2.26)$$

$$(\dot{m}_{exit})_{t+\Delta t} = f((\rho)_{t+\Delta t}^P, (p)_{t+\Delta t}^P) \quad (2.27)$$

$$(h')_{t+\Delta t} = \left(\frac{(\gamma - 1)}{g_l^2 \mathcal{V}}\right) \left[(\dot{m}c_p T_t)_{air} + (\dot{m}c_p T_t)_{fuel} - (\dot{m}c_p T_t)_{exit} \right]_{t+\Delta t} \quad (2.28)$$

$$(p)_{t+\Delta t}^C = (p)_t + \frac{1}{2} \Delta t \left[(h')_t + (h')_{t+\Delta t} \right] \quad (2.29)$$

2.4 Inlet Air, Nitrogen, and Fuel Flows

All inlet flows, either air, nitrogen (N_2) purge, or ethylene (C_2H_4) fuel, were computed using the same perfect gas relationship. The driving factors for the relation were the static to stagnation pressure ratio $\left(\frac{p}{P}\right)$, the gas specific heat and gas constant, and upstream stagnation temperature. The relation in the rig model was bounded on the low end where if the pressure ratio is ≥ 1 , the flow was set to zero, and if the pressure ratio was \leq critical, the Mach number was limited to 1.

From Zucrow and Hoffman [24], the equation for critical pressure ratio is:

$$\left(\frac{p}{P}\right)_{critical} = \left(\frac{2}{\gamma + 1}\right)^{\left(\frac{\gamma}{\gamma-1}\right)} \quad (2.30)$$

From this same reference, the mach number can be backed out of the pressure ratio:

$$M = \left(\left(\frac{2}{\gamma - 1} \right) \cdot \left(\left(\frac{p}{P} \right)^{\left(\frac{1-\gamma}{\gamma} \right)} - 1 \right) \right)^{\frac{1}{2}} \quad (2.31)$$

These relations lead to a direct computation of mass flow based on the pressure ratio:

$$\dot{m} = AMP \left(\frac{\gamma g_c}{RT_t} \right)^{\frac{1}{2}} \left(1 + \frac{\gamma - 1}{2} M^2 \right)^{\left(\frac{\gamma+1}{2(\gamma-1)} \right)} \quad (2.32)$$

With units:

$$in^2 \cdot 1 \cdot \frac{lb_f}{in^2} \cdot \left(\frac{ft \cdot lb_m}{lb_f \cdot s^2} \cdot \frac{lb_m \cdot {}^\circ R}{ft \cdot lb_f} \cdot \frac{1}{{}^\circ R} \right) = \frac{lb_m}{s} \quad (2.33)$$

The inlet mass flow relations apply to the inlet airflow, the nitrogen purge flow, and the ethylene fuel flow computations. The volume averaged static pressure and air tank pressures were used for the main airflow computation. The computed static pressure at the fuel nozzles and the purge/fuel tank pressures were used to compute the fuel nozzle flows. Supply pressures for all three flows were always high enough to choke the inputs, so the flows were very steady for the experimental runs.

2.5 Pressure Loss Computation

Evaluation of the pressure losses was an important part of the lumped volume model. A very detailed analysis of each portion of the inlet section could have been done in order to predict each component of pressure loss in the system, but the pressure losses upstream of the fuel delivery area do not affect the test operation.

This work focused on those pressure losses that impact the integrity of the test data and the prediction of the operation of the WRCVC.

Between the venturi and flow treatment section was a 90° elbow, which generated some turning losses and also generated disturbances in the flow due to the flow turning. Well behind that elbow was the flow treatment section which contained a pair of screens for flow smoothing. Although this apparatus introduced losses in that section, those losses were sufficiently upstream of station 2 to be ignored as being inconsequential to the model. If the losses from this section needed to be computed, a multiple volume computer model would have been required, and the momentum equation would have had to be incorporated into the computation scheme to be able to compute the pressure difference between the volumes.

The first significant pressure loss in the system was across the fuel nozzles. The pressure losses at the fuel delivery plane were caused by two factors. The first factor was the momentum loss caused by cross flow mass addition. The second factor was the pressure drag of the fuel nozzles themselves in cross flow. Downstream of the fuel nozzles, the flow straightener walls and the inlet guide vane pack generated some friction drag which was computed.

The VOLDYN model introduced external flows upstream of the combustor inlet including a nitrogen purge and an ethylene fuel flow. The introduction of this cross flow created two changes in the condition of the main airflow. The first was a momentum loss due to the acceleration of the injected flow at an angle to the main flow. The second was an effective reduction of the main flow area caused by the blockage of the injected flow. The VOLDYN model was designed to model both effects. Zucrow and Hoffman [24] provided the basic relations for perfect gas flow with mass addition in Chapter 9, Section 9-3(a), *Governing Equations for Flow with Simple Mass Addition*. Equation 9.22, repeated here, is:

$$\frac{ds}{c_p} = -\frac{\gamma - 1}{\gamma} \left(\frac{dP}{P} \right) = (\gamma - 1) M^2 (1 - y) \frac{d\dot{m}}{\dot{m}} \quad (2.34)$$

Where M is the local Mach number at the point where fuel is added. The Mach number was computed using the physical area minus the flow area blockage. The value of y is the cosine of the angle between the added mass flow and the main mass flow. For the WRCVC the angle between the fuel nozzle and airflow was 90, so the value of y always has a value of zero.

Rearranging this equation and substituting the actual station values results in the final equation:

$$\left(\frac{\Delta P}{P} \right)_{mass\ addition} = -\gamma (M_3)^2 \frac{\dot{m}_{fuel}}{\dot{m}_3} \quad (2.35)$$

Zucrow and Hoffman [24] also provide computational methods to determine the pressure loss caused by the reduction of momentum of the stream due to external forces. This was found in Chapter 9, Section 9-5(b), *Generalized Steady One-Dimensional Flow of a Perfect Gas*. The fuel nozzles experience a drag force caused by the flow of main air across them.

The incremental friction coefficient is $\frac{4f dx}{D_{hyd}}$ with pressure losses due to friction being:

$$\left(\frac{\Delta P}{P} \right)_{Fanno} = -\frac{\gamma M^2}{2} \left[\frac{4f dx}{D_{hyd}} \right] \quad (2.36)$$

In the referenced chapter, Table 9.6 showed the influence coefficients with the *Driving Potentials* and *Change in Flow Property* computations as a matrix. Removing the friction driving potential leaves the pressure loss due to external forces. The driving potential for external forces is $\frac{2}{\gamma M^2} \frac{\delta D}{pA}$ and the resulting pressure loss equation becomes:

$$\left(\frac{\Delta P}{P}\right)_{Drag} = -\frac{\gamma M^2}{2} \left[\frac{2}{\gamma M^2} \frac{\delta D}{pA} \right] \quad (2.37)$$

This equation reduces to an equation of:

$$\left(\frac{\Delta P}{P}\right)_{Drag} = - \left[\frac{\delta D}{p_3 A_3} \right] \quad (2.38)$$

Where the pressure loss is a function of the drag force, the pressure and area of the the affected section. In the VOLDYN model, the static pressure and area at the fuel nozzles were used in the denominator.

Determination of the drag force was done using standard drag force on a cylinder equations. Hoerner [22] in Section III - Pressure Drag, Figure 12, displayed the classic drag coefficient for a cylinder in cross flow versus Reynolds number, reproduced in Figure 2.1.

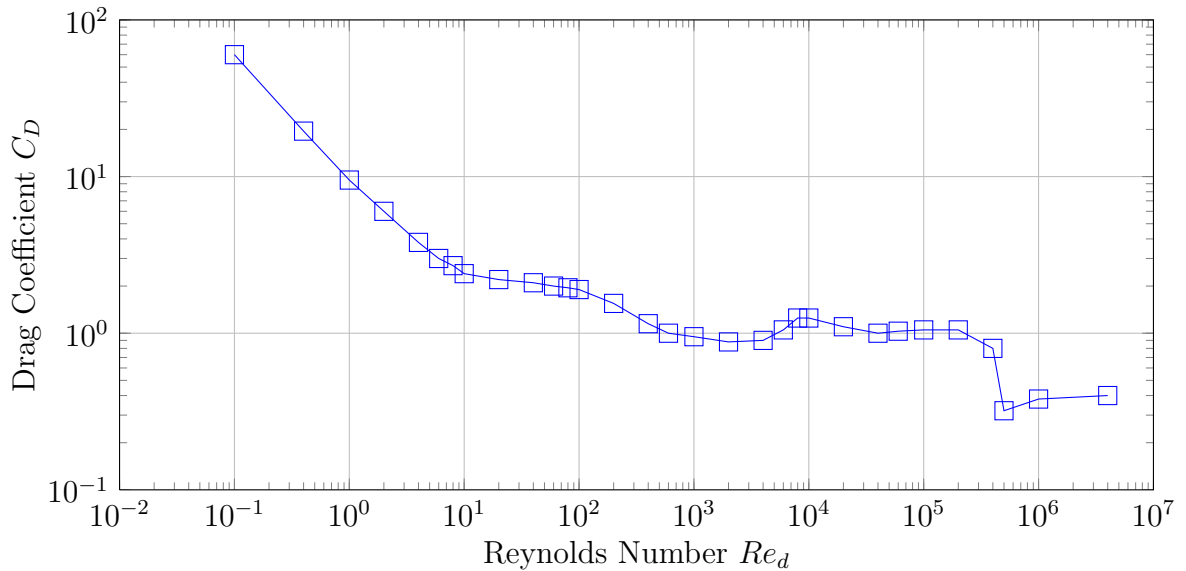


Figure 2.1. Drag coefficient - cylinder in crossflow.

The VOLDYN model computed the local Reynolds number, interpolated this to find the drag coefficient, computed the dynamic pressure, and using the summed frontal area of the fuel nozzles computed the drag force. From the drag force, the pressure loss was computed as follows:

$$C_D = f(Re_D) \quad (2.39)$$

$$F_{drag} = C_D (q * A_{frontal}) = C_D \left[\left(\frac{\rho \vec{V}_3^2}{2} \right) (N_{nozzles} * L_{exposed} * D_{nozzle}) \right] \quad (2.40)$$

Where $N_{nozzles}$ was a count of the number of fuel nozzles used, $L_{exposed}$ was the length of the fuel nozzles as seen by the flow (the height of the fuel nozzle delivery area channel), and D_{nozzle} was the diameter of the fuel nozzle. Together these multiplied into the frontal area of the fuel nozzles.

From the computation of the drag force, the pressure loss can be computed:

$$\left(\frac{\Delta P}{P} \right)_{Blockage} = - \frac{F_{drag}}{p_3 A_3} \quad (2.41)$$

The final pressure losses were computed from the friction drag of the flow straightener walls and inlet guide vanes. For these two loss mechanisms, flat plate drag theory was sufficient to provide an estimate of the friction force. The friction drag of a flat plate was computed using the Chapter 7 correlation found in Incropera [23]. This correlation is:

$$C_{f,x} = 0.0592 Re_x^{-1/5} \quad (2.42)$$

Substituting in the parameters from the rig:

$$F_{drag} = C_{f,l} (q * A_{surface}) = C_{f,l} \left[\left(\frac{\rho \vec{V}_4^2}{2} \right) (2 * N_{vanes} * L_{vane} * W_{vane}) \right] \quad (2.43)$$

Where N_{vanes} was the number of inlet guide vanes, L_{vane} was the height of each guide vane, W_{vane} was the width of the vane, and $C_{f,l}$ was the friction coefficient computed from Reynolds Number Re_L , the integration of Re_x over the width of the guide vane. In the same manner as the pressure drag force caused a pressure drop, the friction drag similarly caused a pressure drop:

$$\left(\frac{\Delta P}{P} \right)_{Friction} = - \frac{F_{friction}}{p_4 A_4} \quad (2.44)$$

Similar geometry data was used to compute the friction of the flow straightener walls and its contribution to the pressure losses between stations 4 and 5.

2.6 Exit Flow Characteristic

The exit flow characteristic of the inlet section is the inlet flow characteristic of the WRCVC, because the rig feeds the mixed air and fuel flow into the WRCVC. If the WRCVC were missing and the rig exhausted to atmosphere directly, the average pressure in the rig volume would naturally be very close to atmospheric. Conversely, if the WRCVC were to be replaced with a flat plate that blocks the flow, the rig pressure would rise to the value of the upstream tank pressure. If the WRCVC were replaced with a calibrated nozzle, the ability of that nozzle to pass flow would be its flow characteristic, governed by the pressure ratio between atmospheric pressure and the pressure at the exit of the rig, and that flow characteristic causes a backpressure in the rig. The flow characteristic of the WRCVC, similarly to a nozzle, is governed by equations and can be computed as a function of that same pressure ratio.

The flow characteristic is not governed only by the pressure ratio, because it is a mechanical device. Much like a jet engine compressor's flow characteristic changes as its rotational speed changes, the WRCVC flow characteristic changes as the rotor speed changes. Lightner [26] provided a set of curves for the flow characteristic of the WRCVC as a function of rotor speed and inlet pressure.

In order to generate the flow characteristic of the WRCVC, modifications were made to the SCW1D program described in Section 1.3 to allow running successive cases, raising and lowering the inlet stagnation pressure while holding the rotor speed constant and the inlet stagnation temperature constant. A more complete description of the modifications that were made to allow generation of the exit flow characteristic are found in Section 3.2.

2.7 Lumped Volume Dynamic Model Validation

One way to validate the lumped volume dynamic model is to compare the results in cold flow versus the rig test data. This is done in the results section of this thesis, but with pressure losses the comparison cannot be considered academic. A second validation of the dynamic model, without pressure losses, can be done by using the equations on a theoretical test case. In the Purdue ME500 Advanced Thermodynamics curriculum, such a test case can be found in the study of Transient Analysis as Example 5.1. The lumped volume model is applied to this test case for validation.

Given: Insulated air rigid tank with the following initial conditions:

$$\mathcal{V}_i = 0.15m^3$$

$$p_i = 2 \text{ bars}$$

$$T_i = 300K$$

Tank is charged from a large reservoir of air at 10 bars, to a final pressure $p_f = 4$ bars, and a final temperature $T_f = 360\text{K}$. What is the temperature of the reservoir?

Solution:

$$\frac{dm_{CV}}{dt} = \sum_{in} \dot{m}_{in} - \sum_{out} \dot{m}_{out}$$

$$dm_{CV} = \dot{m}_{in} dt = dm_{in}$$

Ignoring work and heat transfer,

$$\frac{dE_{CV}}{dt} = \sum_{in} \dot{m}_{in} \left(h + \frac{\vec{v}^2}{2} + gz \right)_{in} - \sum_{out} \dot{m}_{out} \left(h + \frac{\vec{v}^2}{2} + gz \right)_{out}$$

Since the tank is quiescent before and after the transfer, ignoring gravity effects, and knowing there is no outflow, this equation becomes:

$$\frac{dU_{CV}}{dt} = \dot{m}_{in} * h_{in}$$

$$dU_{CV} = h_{in} \dot{m}_{in} dt = h_{in} dm_{in} = h_{in} dm_{CV}$$

Knowing the beginning and end states, solve for h_{in} :

$$\int_i^f dU_{CV} = h_{in} \int_i^f dm_{CV}$$

$$\Delta U_{CV} = m_f u_f - m_i u_i = h_{in} (m_f - m_i)$$

Given the end states:

$$m_i = \frac{p_i \mathcal{V}_i}{RT_i}$$

$$R_{air} = 0.287 \frac{\text{kJ}}{\text{kg K}}$$

$$m_i = \frac{2 \cdot 10^5 \frac{\text{N}}{\text{m}^2} \cdot 0.15 \text{m}^3}{287 \frac{\text{J}}{\text{kg K}} \cdot 300 \text{K}} \cdot \frac{1 \text{J}}{1 \text{N} \cdot \text{m}} = 0.348 \text{ kg}$$

$$m_f = \frac{4 \cdot 10^5 \frac{N}{m^2} \cdot 0.15 m_3}{287 \frac{J}{kg \cdot K} \cdot 360 K} \cdot \frac{1 J}{1 N \cdot m} = 0.581 \text{ kg}$$

From air tables [27]: (values in curriculum are slightly different)

$$u_i = u_{air}(T_i = 300 K) = 214.32 \frac{kJ}{kg}$$

$$u_f = u_{air}(T_f = 360 K) = 257.48 \frac{kJ}{kg}$$

Recall:

$$m_f u_f - m_i u_i = h_{in} (m_f - m_i)$$

$$h_{in} = \frac{m_f u_f - m_i u_i}{m_f - m_i}$$

$$h_{in} = \frac{0.581 kg \cdot 257.48 \frac{kJ}{kg} - 0.348 kg \cdot 214.32 \frac{kJ}{kg}}{0.581 kg - 0.348 kg} = 321.94 \frac{kJ}{kg}$$

$$T_{in} = T_{air}(h_{in}) = 321.4 K$$

To validate this result, a computer program EXAM51 was written, in FORTRAN, using the continuity and energy equations as developed for the model. The EXAM51 program, of which a listing is given in Appendix A, starts with the same initial conditions as Example 5.1, a tank temperature of 321.4 K, and computes the time integrated tank density and pressure up to the final conditions. Total mass in the volume, and temperature in the volume are also computed. Since the mass flow in the example is constant, the Euler time integration method used could be called explicit or implicit.

Figure 2.2 shows the results of the model validation. The identical results between the two point computation and the time integrated computation validates the model's equations and also shows the stability of the Euler method.

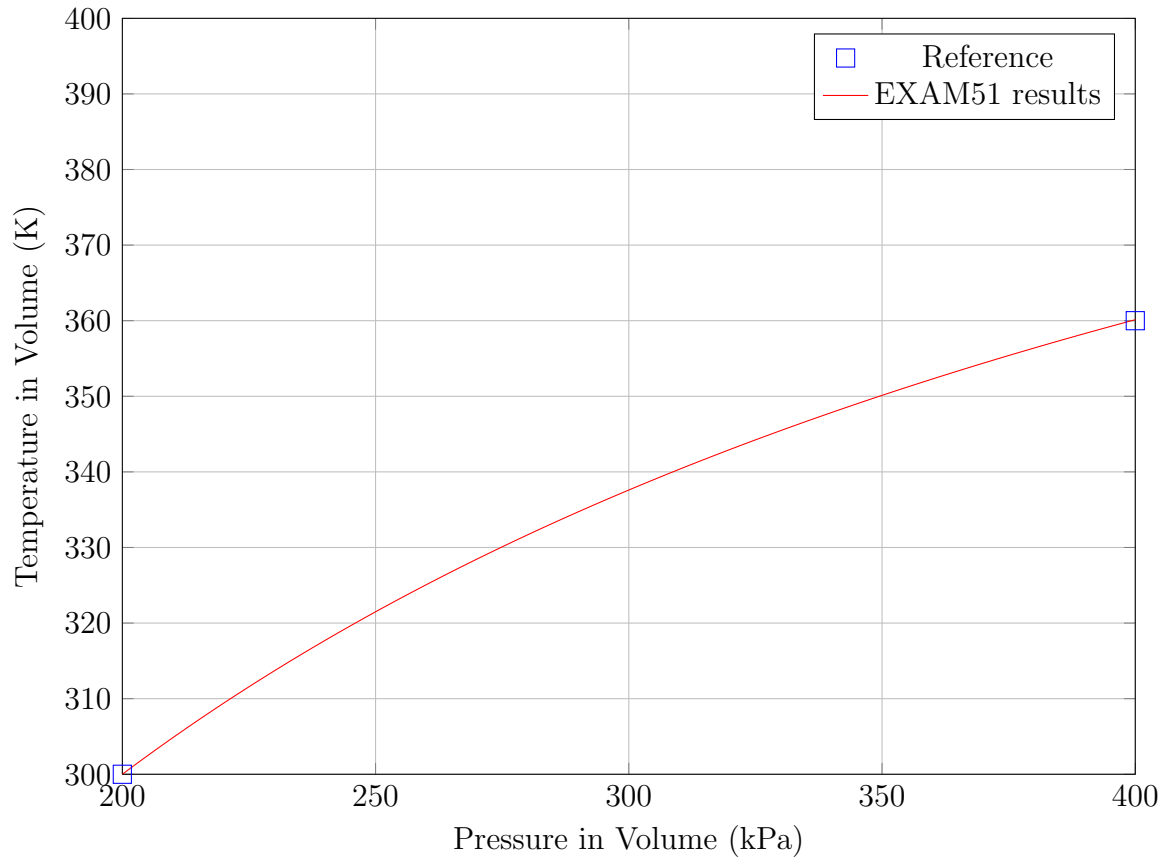


Figure 2.2. EXAM51 model validation results.

3. NON-DIMENSIONAL FLOW CHARACTERISTIC OF THE WRCVC

3.1 Software Modifications for Iteration

The SCW1D program is a computer program model that can be used to compute the performance of the WRCVC. It was originally written as a standalone Fortran program with an interactive iteration step capability, all from the console. The data input, results output, control and solution iteration code were originally contained in the main program, with just two other subprogram modules. This organization made the program difficult to manipulate for other uses, such as for iteration or using the program as a subroutine in another program. In order to perform a study of the flow characteristic of the rig, the program needed to be modified so that the inputs could be managed as a separate module from the iteration of the equations, to compute the conditions in the rotor and to compute the inlet and exit flow conditions.

Figure 3.1 shows the basic logic of the SCW1D program as delivered to the author for editing. The code portion that reads the initial conditions and input values was removed from the main program and placed into a module named RDINPT, and additional capability was added to allow Fortran NAMELIST input to the program. This module also has two parameter inputs, the first representing the program run mode ($0 = \textit{interactive}$, $1 = \textit{subroutine}$, or $2 = \textit{reinitialize}$) and the second representing the Fortran input file unit desired.

The iteration code was removed into a second module named FTPSIM, with one parameter input, representing the program run mode. This module contains the iteration code which solves the case and then prompts the user for interactive input, if running in interactive mode. In subroutine mode the interactive code is bypassed

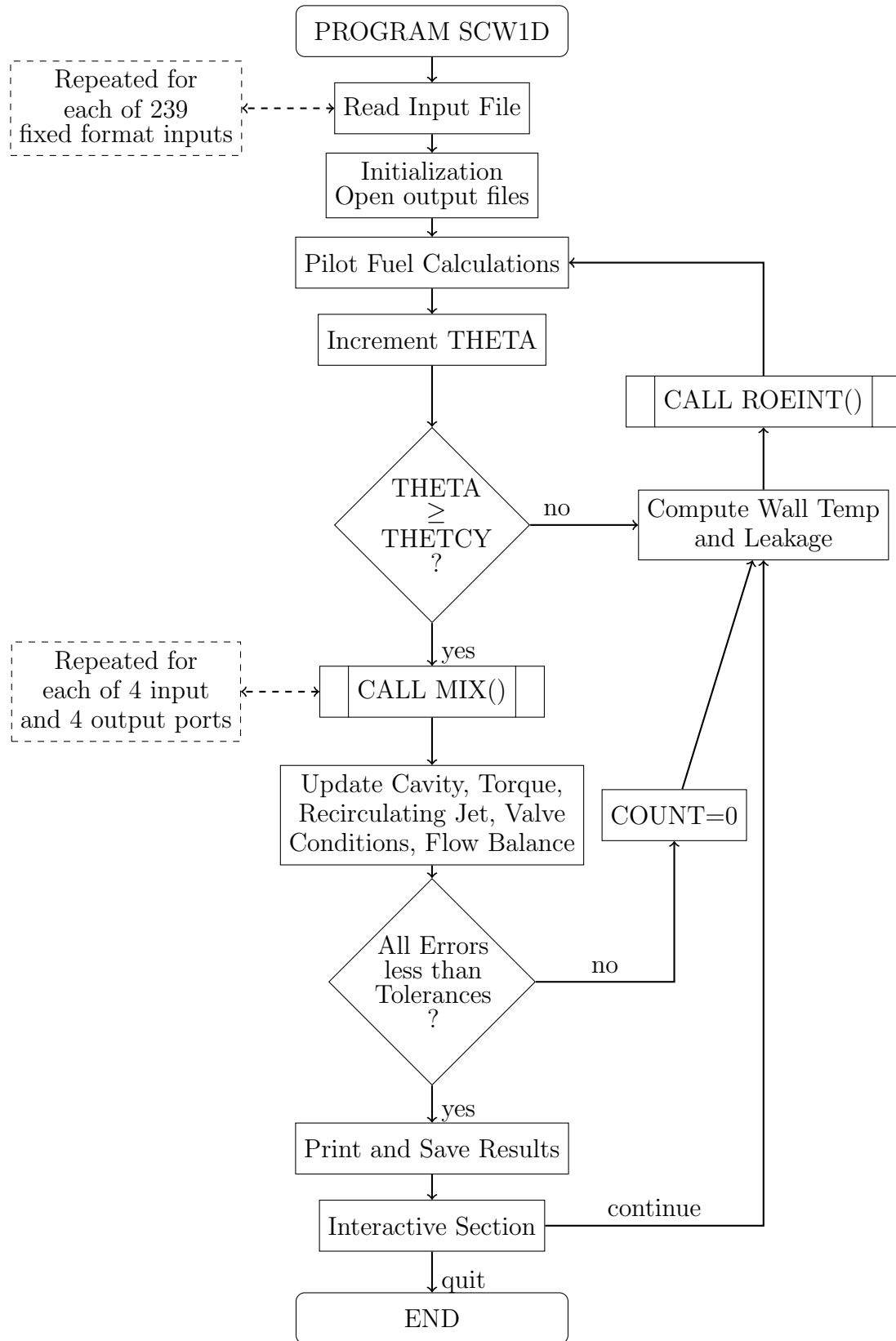


Figure 3.1. High level flowchart for WRCVC cycle computation.

and the module returns to the main program. The main program can then analyze the results and adjust the input conditions as needed.

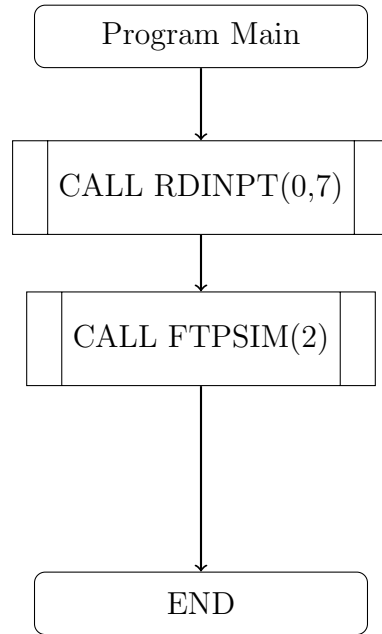


Figure 3.2. Modified flowchart for SCW1D main program.

If the iteration code module is run in reinitialize mode, the solution equations are reset for solving the conditions as if a new set of inputs were read, but no actual input data read operation is performed. The new SCW1D main program flowchart is seen in Figure 3.2. The RDINPT module flowchart is seen in Figure 3.3 and the FTPSIM flowchart is seen in Figure 3.4.

3.2 Software Modifications for Pressure Sweep

The VOLDYN dynamic rig computer program assumes a fixed design rotor speed, and with no heat addition assumes an essentially fixed inlet total temperature. A decision was made that generating a flow characteristic as a function of changing inlet total pressure would be computationally more efficient than attempting to integrate

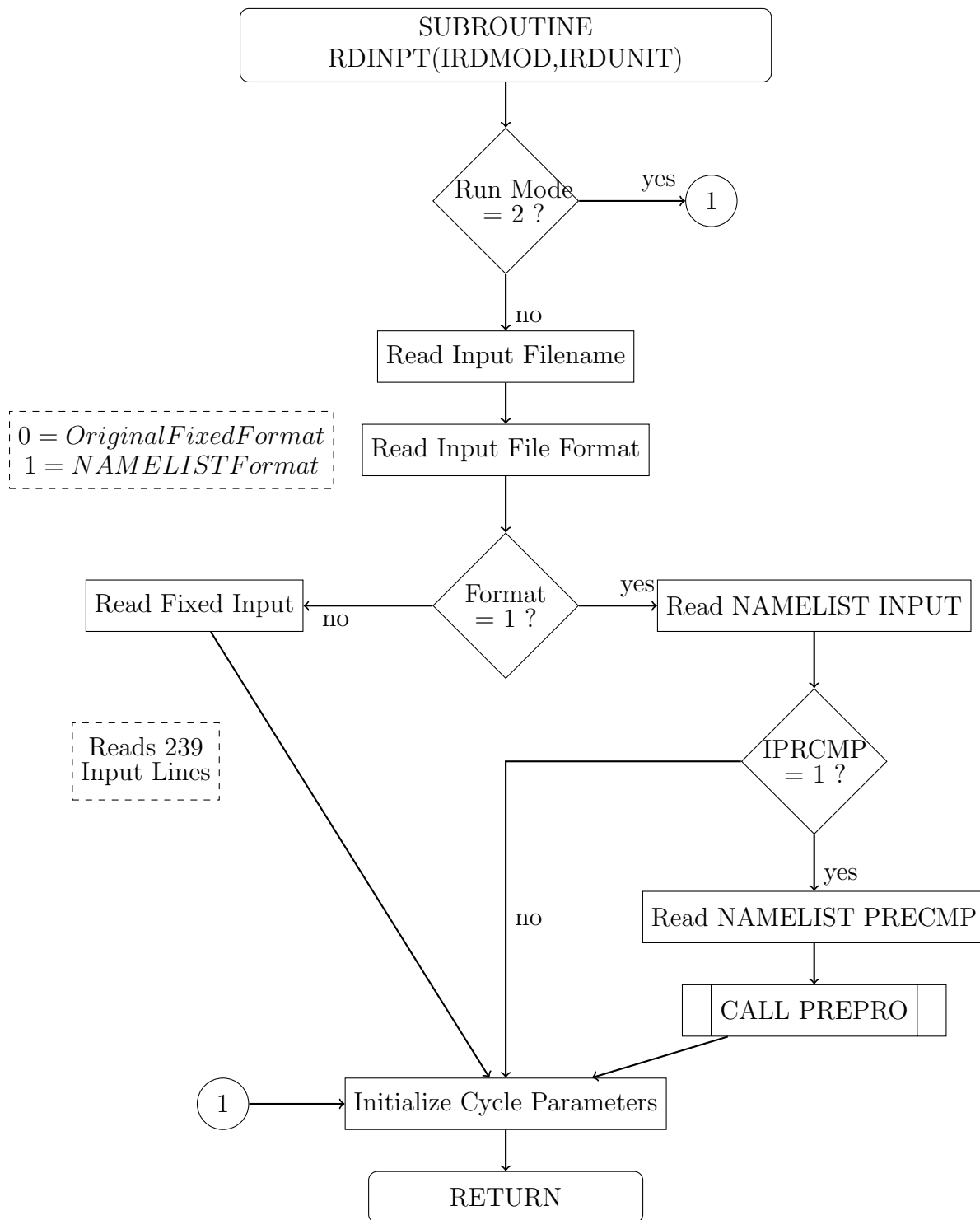


Figure 3.3. Flowchart for RDINPT input subroutine.

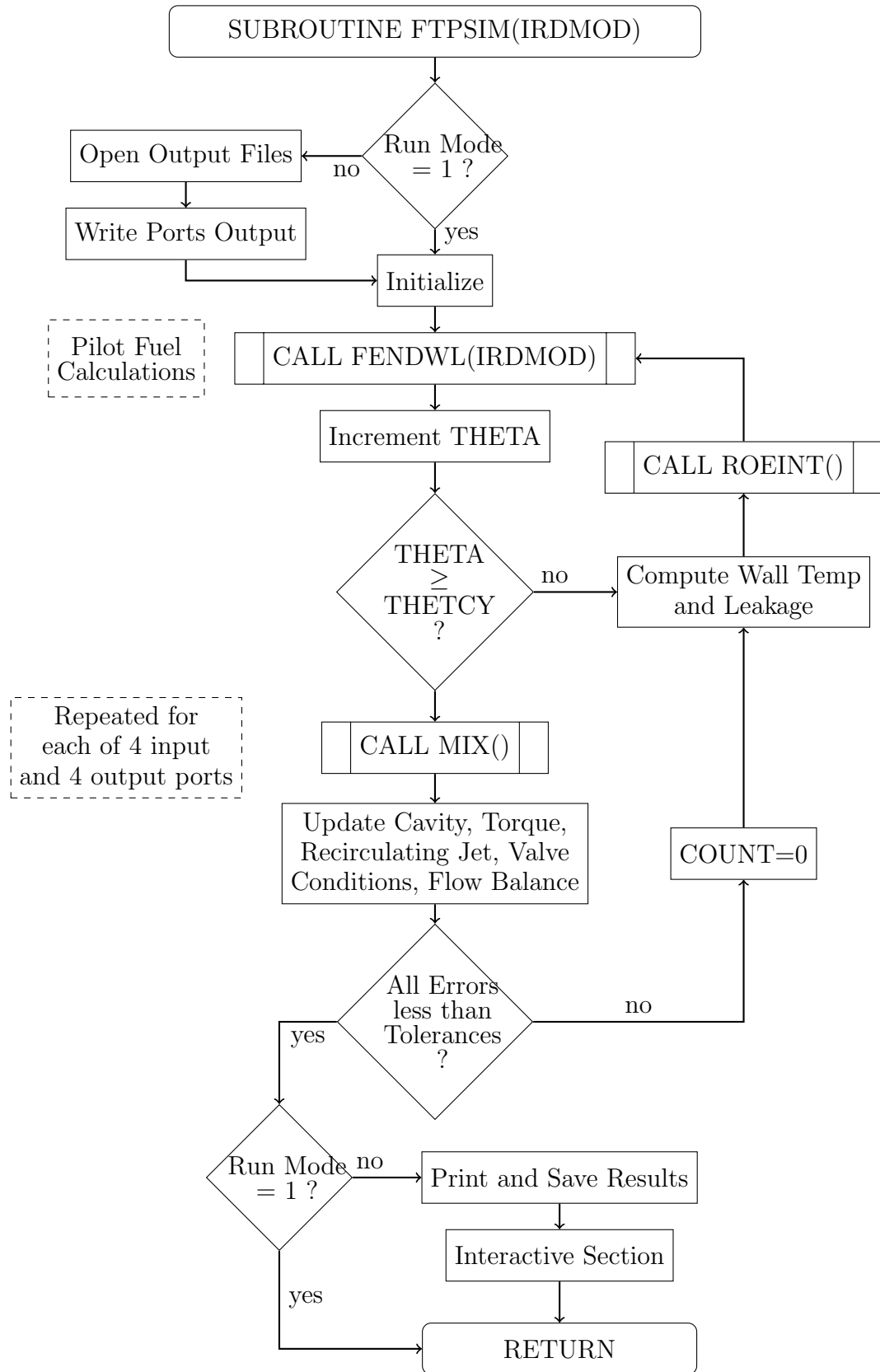


Figure 3.4. Flowchart for FTPSIM solution subroutine.

the SCW1D program into the VOLDYN rig program. Because of the changes made to allow iteration, the SCW1D main program was capable of being modified so that it can execute a series of similar cases at differing inlet pressures. In order to keep the program stable, the previous case was always used as the input to the next case, and the pressure change was kept small, only 0.05 percent per case, in order to allow the case to adjust to the new input condition without going unstable.

In the main program, the input modifications were assembled into a loop. The main program, showing the loop, is seen in Figure 3.5. Starting with the initial case, the base results are computed, and then the inlet pressure is systematically lowered or raised depending on the direction of the iteration, followed by another call to the iteration logic.

Each computation of the WRCVC cycle results in printed output containing the corrected flowrate, average inlet and exit conditions, and other cycle results, which are then able to be correlated into an equation for use in the VOLDYN program.

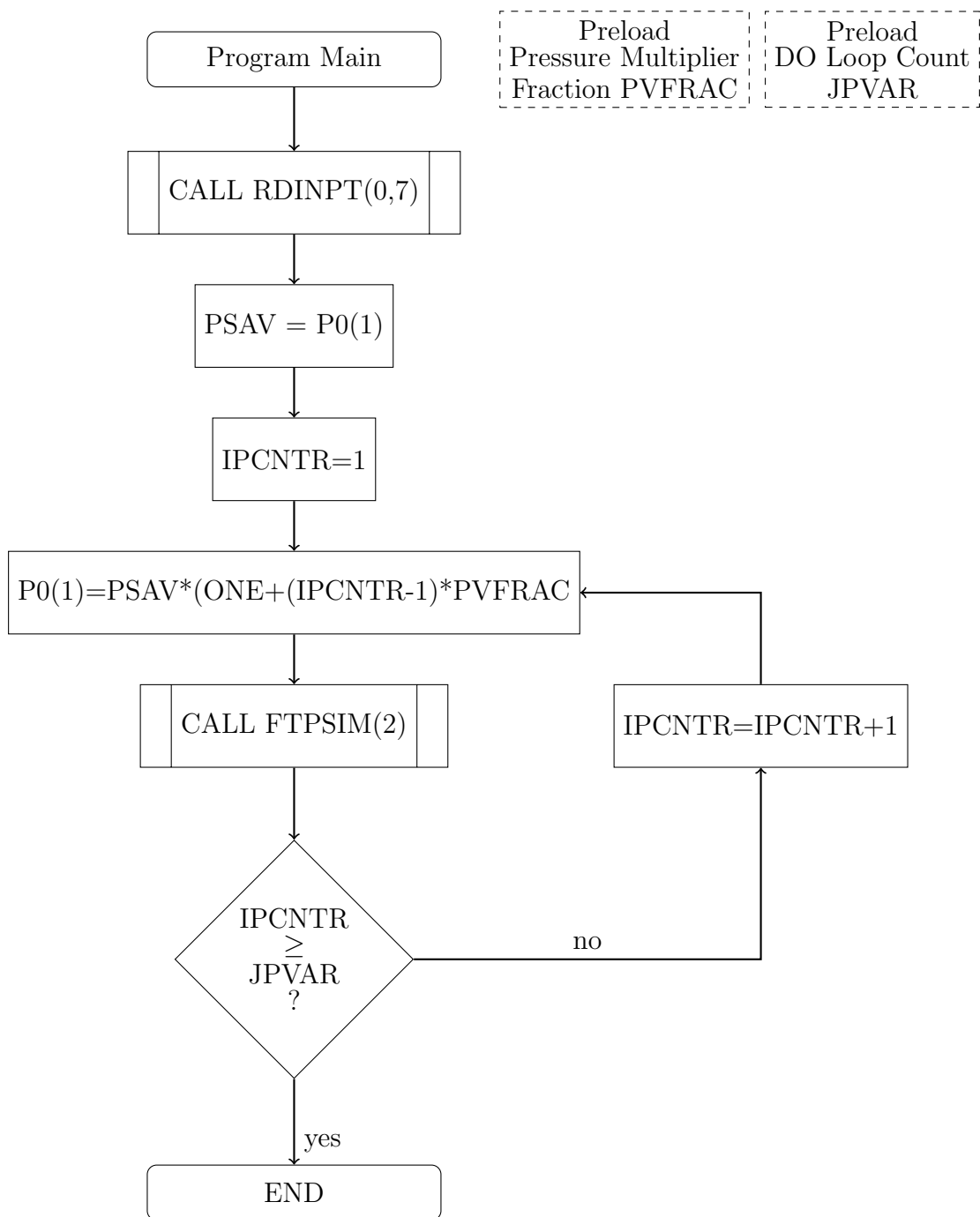


Figure 3.5. Flowchart for SCW1D main program, modified for pressure sweep.

3.3 Software Modifications for All other Purposes

In addition to changes needed so that the program can be used for iteration and also can be used as a subroutine, other changes were made to the code so that the program will be easier to maintain, executes faster, and so that the input preprocessing and output postprocessing can be merged into the program.

One source of slow execution of a typical scientific program is the constant creation and destruction of local, temporary variables. In a modern computer, when a program submodule is encountered in the code, a copy of that code is "loaded" and all local, temporary variables are created and initialized. When the program submodule completes, those local, temporary variables are released back to memory. This process is also performed on each line of the program that uses program elements called "literals". A literal is a programming element that "literally" means what it is, such as in the equation $y = 5 * x + 3$, the 5 and the 3 are considered literals. Using a literal in a line of code causes creation and initialization of the local, temporary variable, typically each time that line of code is executed, even for optimized code. Conversion of literals to global constant variables eliminates the creation, initialization and destruction processes, replacing the literal with a global address reference.

The ROEINT and BC modules are the main sections of the program that are executed repeatedly, often thousands of times per program run. A study of the entire SCW1D program yielded 154 lines of code using at least one literal double precision 0.0, with 42 lines in the ROEINT and BC modules. It yielded 192 lines of code using at least one literal double precision 1.0, with 136 lines in the ROEINT and BC modules. And it yielded 121 lines of code using at least one literal double precision 2.0, with 60 lines in the ROEINT and BC modules. These literals were replaced with global constants, causing a significant reduction in execution time for the program.

A second area of interest centered around the portability of the program and the need to bring the program into a modern execution environment. The original program was written primarily for Fortran 77, using constructs that were non-portable to other environments. The original Fortran compiler needed for the program was the g77 program, the original GNU project Fortran 77 compiler [28]. While the g77 program is a classic and well supported program, it does not allow Fortran-90 constructs such as include files and has limited platform compatibility.

The preferred compilation platform today is the gcc4 platform [29], which combines the latest GNU C compiler with front ends for C, C++, Objective-C, Fortran, Java, Ada, and Go. This compiler series is globally accepted and actively maintained. The Fortran module is Fortran-90 compliant and is available on all Linux variants, including the RedHat Linux used on IUPUI lab equipment. It also is available on cygwin, which is a licensed version of Linux that runs natively on a Windows machine without use of a virtual machine. It is available on Mac OS/X platforms as well, so it is available for the most popular platforms used by the students and faculty at IUPUI.

Once the program was upgraded to the gcc4 version of Fortran, named gfortran, extensive modifications were made to the COMMON block areas and DIMENSION areas. All DIMENSION statements that are used in COMMON blocks were placed into include files, and all COMMON block definitions were put into include files. The DIMENSION and COMMON statements in the program modules were then replaced with include statements, and all array sizes were specified using Fortran-90 PARAMETER statements. The effect of this change is significant, placing the definition of all global variables into separate files, so that a change to that file is reflected in all of the program modules instantly. For this to take effect, the program was also given a valid Makefile which resolves all dependencies during the build process. In addition, all files associated with the program, including source files, include files,

and the Makefile, were placed into an RCS software repository for revision tracking and documentation.

As described in the RDINPT flowchart seen in Figure 3.3, the 293 separate lines of fixed format input have been supplemented by the addition of Fortran NAMELIST inputs. The main namelist is called INPUT, and an additional namelist PRECMP is available for control of the preprocessor.

The preprocessor takes the physical inputs that describe the WRCVC and generate the non-dimensional inputs required by the SCW1D program. In preprocess mode, the specific parameters generated by the preprocessor replace those read in by the Namelist inputs. Preprocess mode is not available with non-namelist inputs.

The postprocessor takes the non-dimensional outputs and generates the dimensioned physical outputs required for some studies. Neither the preprocessor nor the postprocessor were needed for this thesis. These modules were created by the author for use in a study to design a WRCVC for a 16 inch diameter, Mach 2.0 ramjet missile.

3.4 SCW1D Sweep Results

The WRCVC combustor geometry is shown in table 3.1. Initial conditions for these four conditions are seen in table 3.2. The nominal inlet total pressure $P_0(1)$ is the starting point for the sweep calculations, while the minimum and maximum values are the limits to the pressure variation produced by the computer program loop. There were four distinct rig operating conditions. The first was the cold flow condition (cold) where the torch was off. This condition included operation where the nitrogen purge or the ethylene fuel flow was on. It also included a short period where the torch fuel was on without the torch air. The flow characteristic of the WRCVC based on pressure should not be affected by the addition of fuel or purge

flows, assuming negligible change to the specific heat ratio of the flow. The first condition was seen during the time that the main air was brought up to the set point, the time that the nitrogen purge flow was on, the time that the torch fuel was burped (momentarily on with the torch air off and the spark off) and the time that the main fuel flow was burped. The second condition (torch on) was where the torch air is on, but the torch fuel and the spark were both off. The third condition (torch lit) was where the torch air and fuel were on and the torch was lit. This condition was seen immediately after the torch spark and fuel were turned on, and remained on until the main fuel was added near the end of the testing, because the torch was needed to cause ignition of the main fuel flow. The fourth and final (firing, aka hot) condition was where the torch was lit and the main fuel was on, creating a properly positioned combustion profile in the combustor. This condition lasted one second during the referenced test sequence. The torch remained on until it was manually turned off, so after combustion, the torch lit condition was maintained.

Table 3.1 WRCVC rig geometry parameters.

Parameter	Value	Units
Rotor speed	2100	rpm
Number of cycles per revolution	1	
Rotor angular velocity ω	219.9	rad/sec
Number of passages	20	
Passage length, L	30.95	in
Passage height, h	2.614	in
Outer passage width	2.757	in
Inner passage width	1.936	in
Mean passage width, b	2.381	in
Outer radius	9.094	in
Inner radius	6.48	in
Mean radius	7.896	in
Wall thickness, k	0.1	in
Inlet port opening angle	62.0	deg
Inlet port closing angle	166.0	deg
Exhaust port opening angle	18.0	deg
Exhaust port closing angle	137.0	deg
Torch center angle	242.14	deg

Table 3.2 WRCVC non-dimensional input parameters.

Condition	Cold Flow	Torch On	Torch Lit	Firing
Parameter	-	-	-	-
Rotor Speed	2100	2100	2100	2100
Nominal inlet total pressure P0(1)	1.313	1.308	1.308	1.242
Sweep minimum P0(1)	1.006	1.006	1.007	1.233
Sweep maximum P0(1)	1.379	1.373	1.373	1.304
Inlet total temperature	.99043	.99043	.99043	.9980
Exit static pressure	1.007	1.007	1.007	1.007
Exit static temperature	1.123	1.131	1.131	3.95
Torch total pressure	No port	8.80	8.80	8.80
Torch total temperature	No port	1.0	6.01	6.01
Reference pressure	14.696	psia		
Reference temperature	520	R		

The nominal characteristics of the WRCVC at these four conditions are shown in standard plots of the unrolled wave rotor temperature, log pressure, and fuel fraction values, presented as color contour plots. These plots will be called x-t plots. The four conditions are plotted in Figures 3.6, 3.7, 3.8, and 3.9. In the cold flow plot, the inlet and exhaust port start and end are shown. In all of the plots these ports are represented by a white line. In the torch lit plot, the torch igniter location is shown. A small slice of increased temperature is shown past the igniter in this plot. The influence of the torch air on pressure is seen in the pressure plot on this and the torch on (but not lit) plot. In the Firing plot, the combustion zone is shown as a large increase in temperature.

The flow characteristics were generated for the cold flow, torch on, torch lit, and firing cases. The cold and both torch cases were capable of being iterated all the way to ambient pressure ($P0(1) \approx 1.0$) The firing case could not be iterated as far down but exhibited a reasonable plot outside its normal operating point. The four correlated flow characteristics are shown in Figure 3.10 (cold), Figure 3.11 (torch on), Figure 3.12 (torch lit), and Figure 3.13 (firing).

In Figure 3.14 the four characteristics can be compared. In the comparison it is seen that a dramatic increase in flow occurs when the WRCVC was lit, due to the high pressure in each channel generating a large expansion wave as it passes the exhaust port. Since the intention of the rig operation was to hold the flow as near as constant as possible, the characteristic instead shifted to a lower pressure during the combustion (firing) portion of the rig operation.

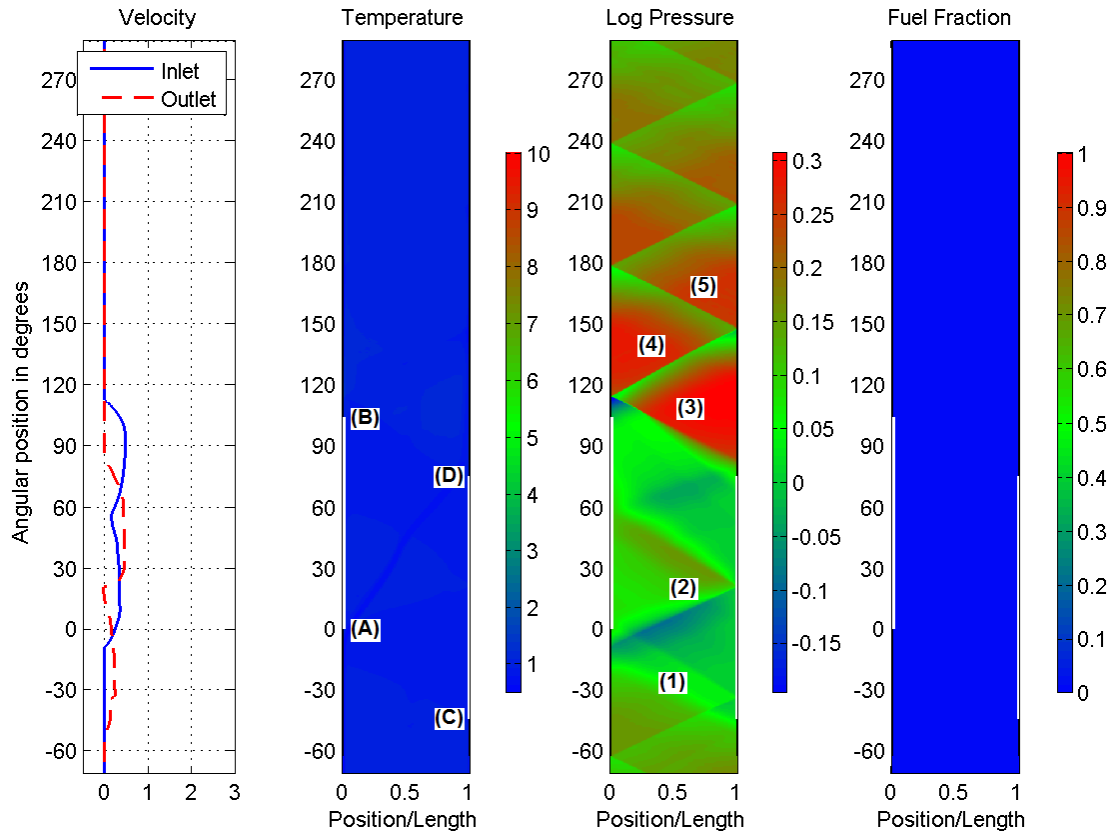


Figure 3.6. WRCVC Cold flow condition temperature, density, fuel fraction for the nominal inlet pressure. (A) Inlet opening, normalized to zero angle. (B) Inlet closing. (C) Exhaust opening. (D) Exhaust closing. (1) Expansion fan caused by exhaust opening. (2) Compression wave caused by inlet opening. (3) Hammer shock from exhaust closing. (4) Reflected hammer shock from left end wall. (5) Reflected hammer shock from right end wall.

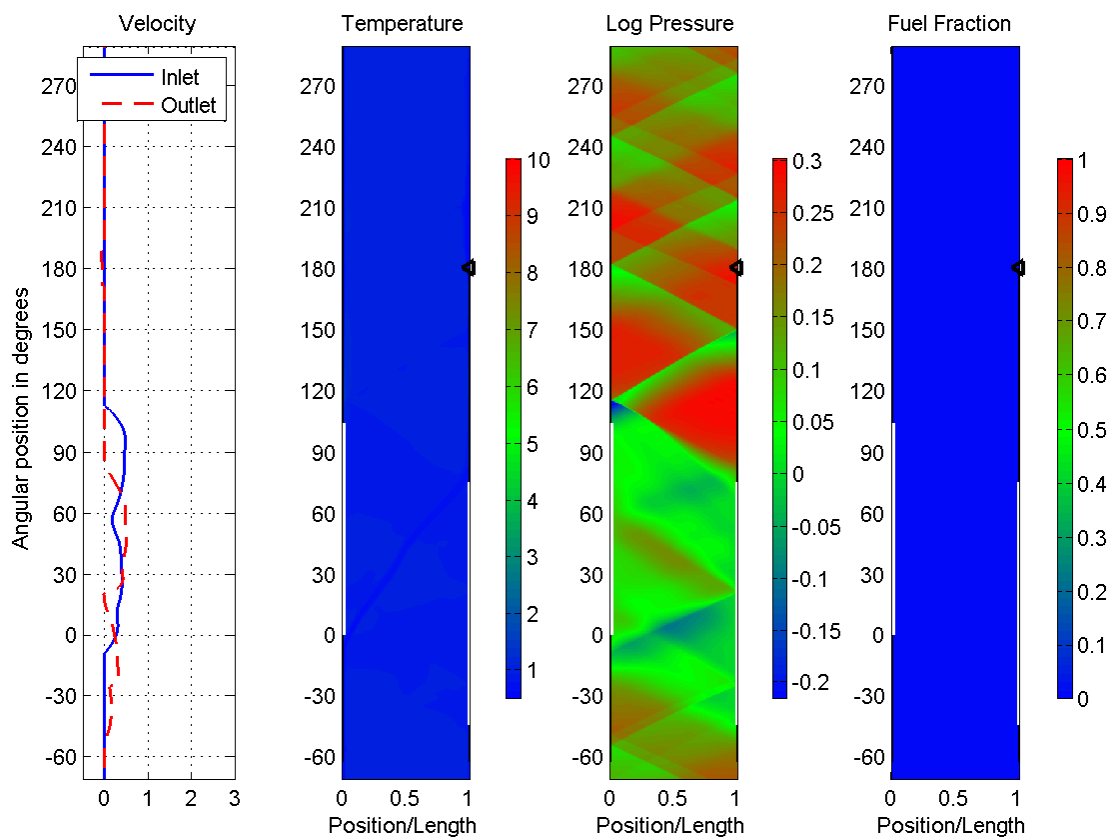


Figure 3.7. WRCVC Torch On condition temperature, density, fuel fraction for the nominal inlet pressure.

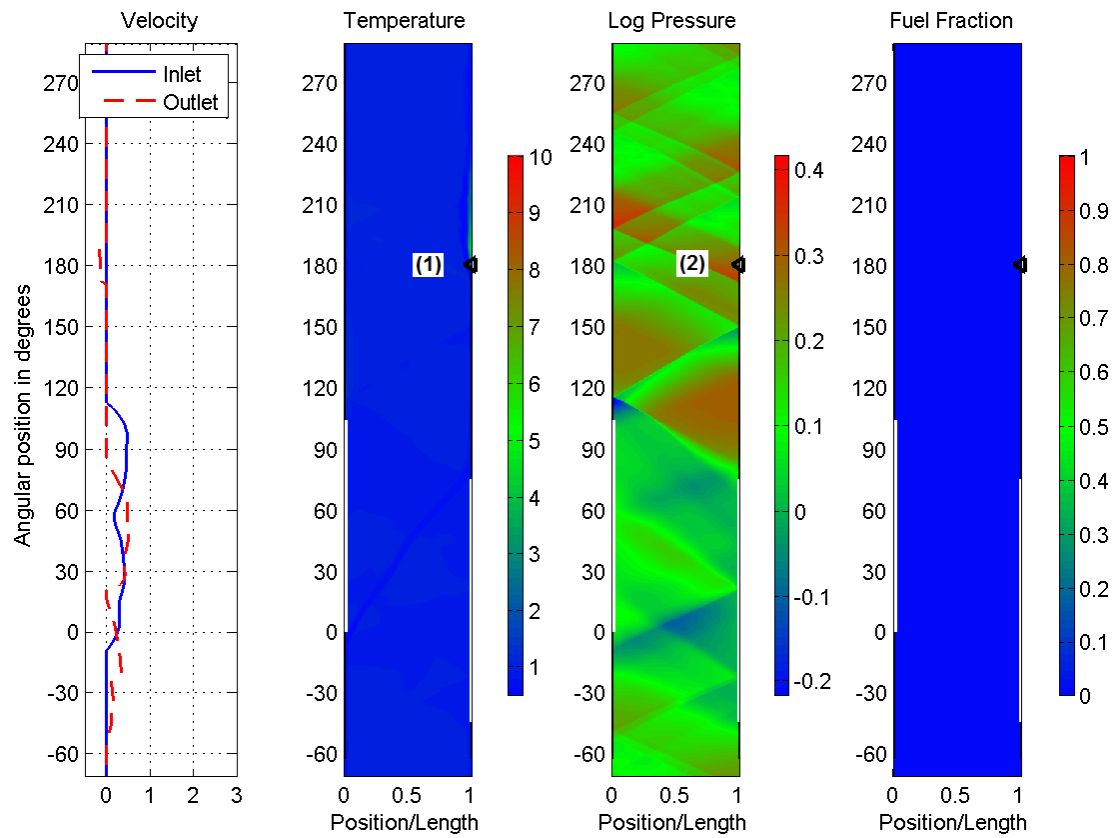


Figure 3.8. WRCVC Torch Lit condition temperature, density, fuel fraction for the nominal inlet pressure. (1),(2) Torch location.

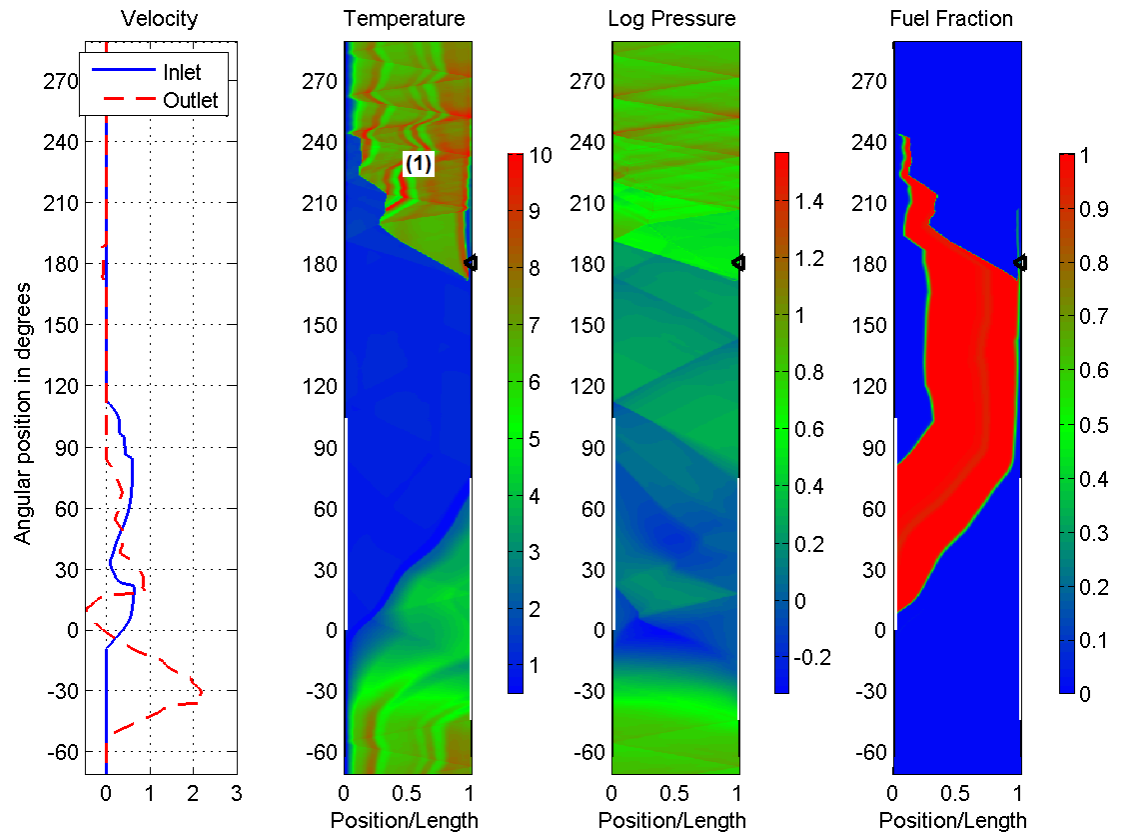


Figure 3.9. WRCVC Firing condition temperature, density, fuel fraction for the nominal inlet pressure. (1) Combustion zone.

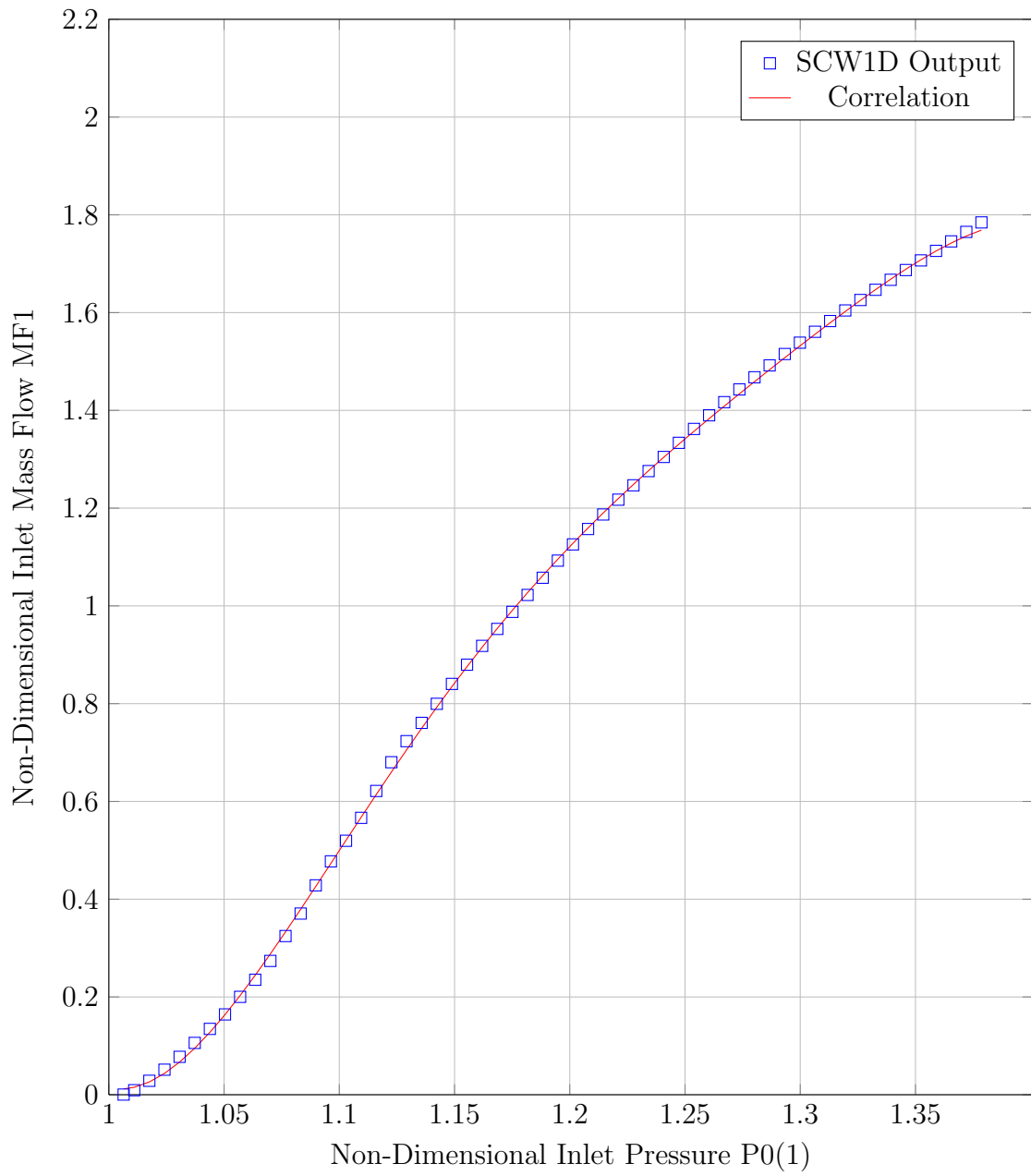


Figure 3.10. Cold flow sweep results - SCW1D output vs 5th order polyfit.

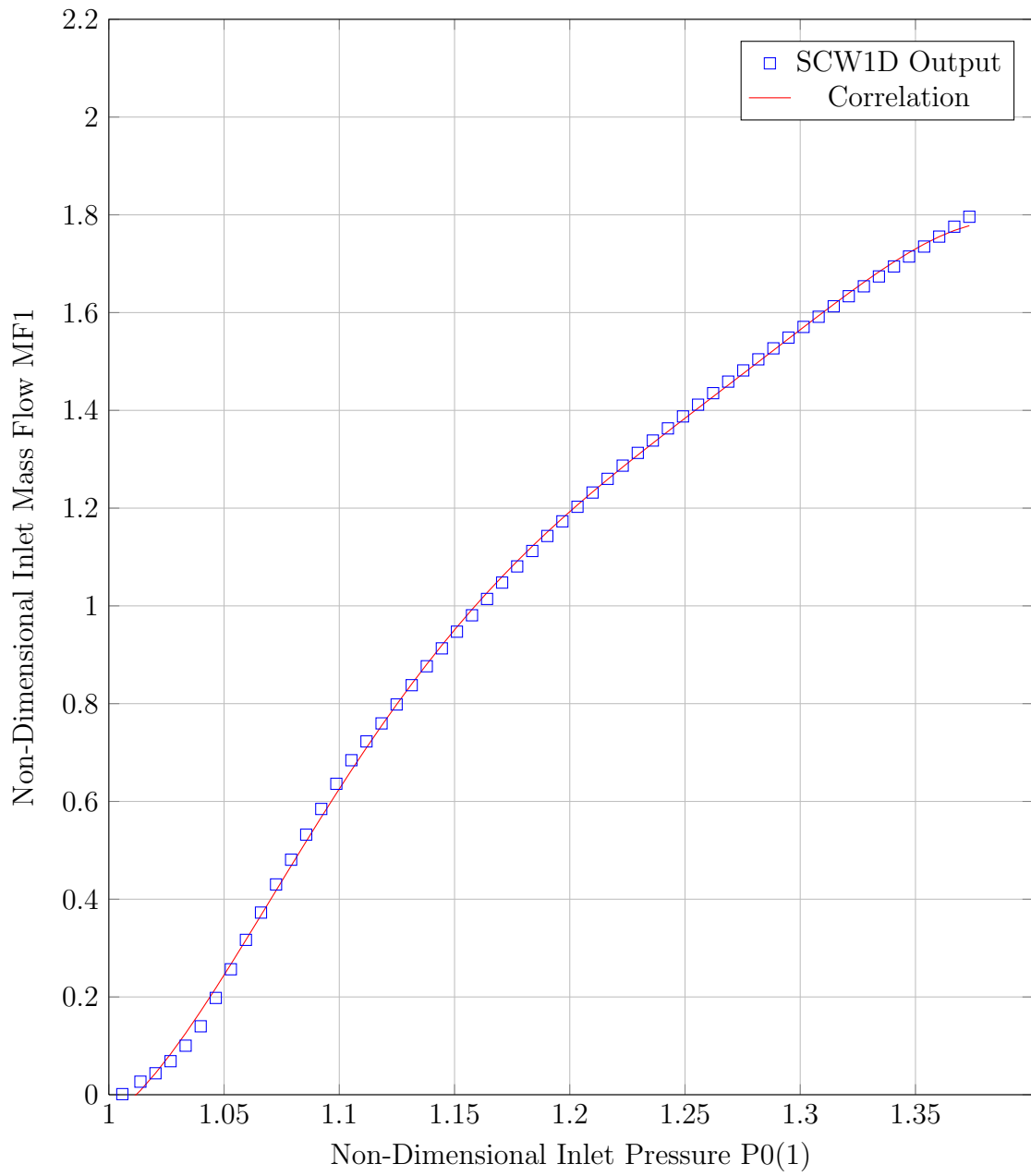


Figure 3.11. Torch on sweep results - SCW1D output vs 5th order polyfit.

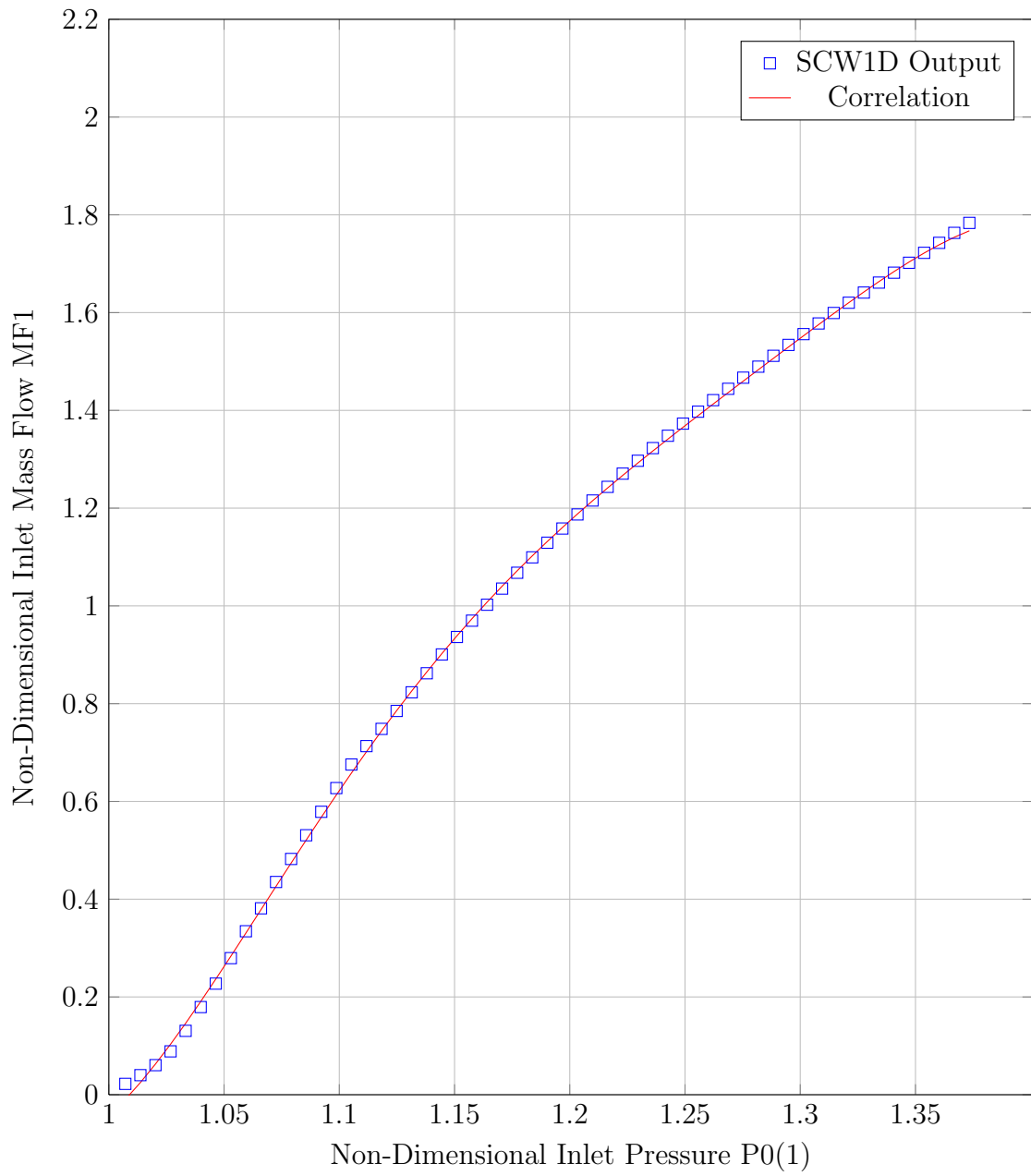


Figure 3.12. Torch lit sweep results - SCW1D output vs 5th order polyfit.

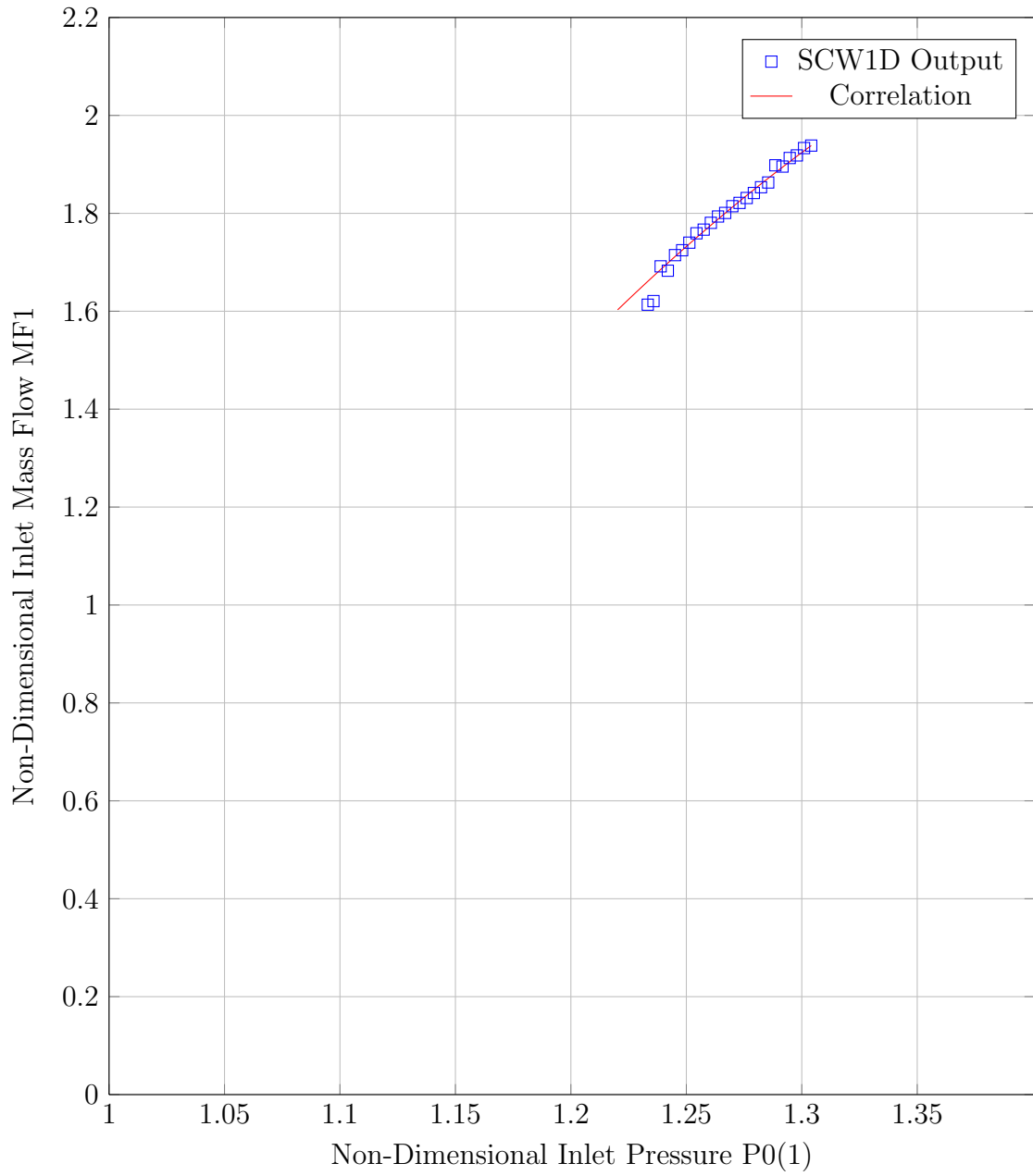


Figure 3.13. Firing condition sweep results - SCW1D output vs 2nd order polyfit.

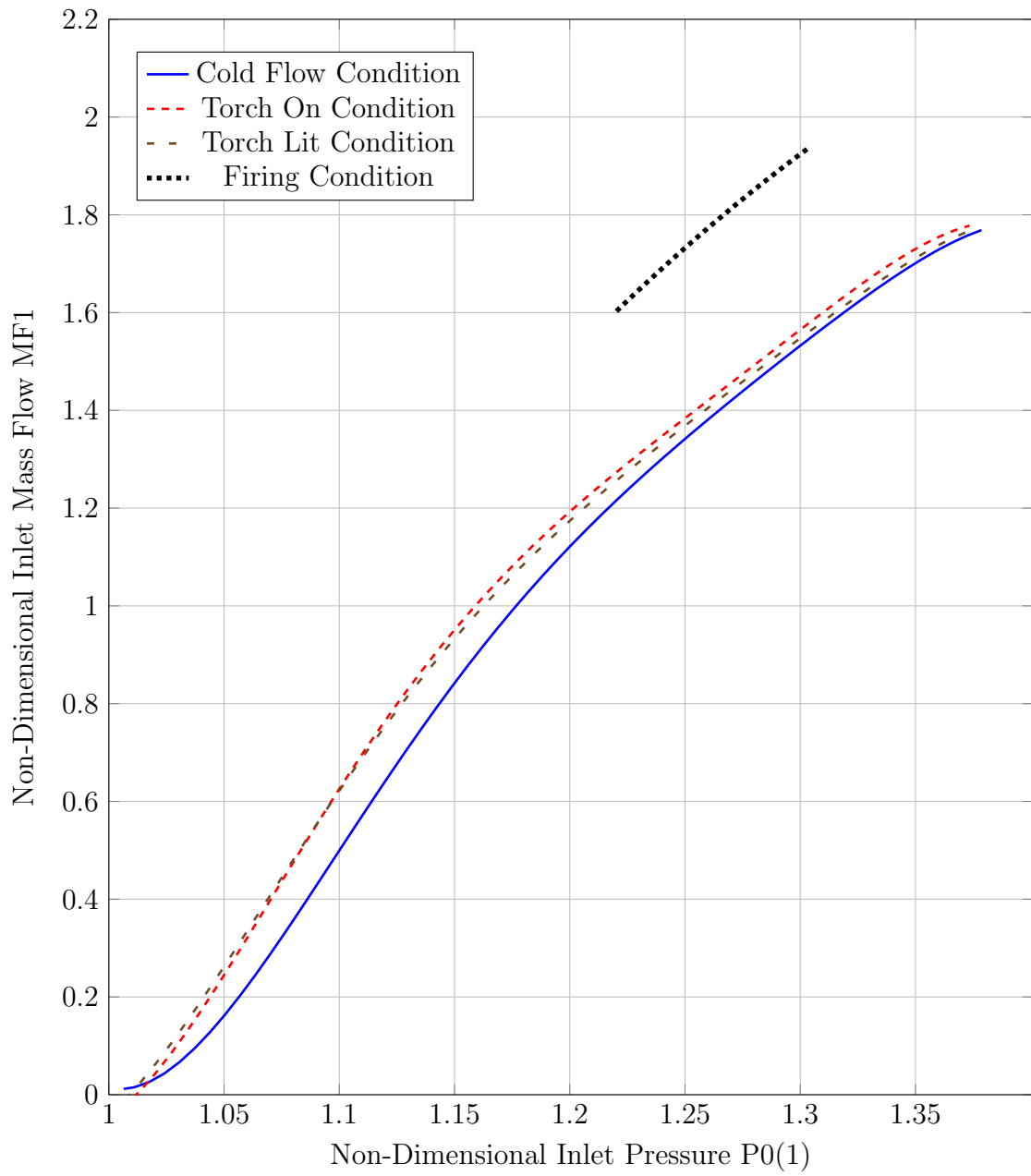


Figure 3.14. Sweep comparison - polyfit results at conditions.

4. TIMING ANALYSIS OF THE INLET SECTION AND WRCVC ROTOR

4.1 Inlet Section Volume Timing Analysis

A time analysis of the inlet section at the design airflow was needed to determine if changes in the WRCVCs operating characteristic were too fast to be reflected by the dynamic equations used by the VOLDYN program. At a constant inlet temperature, changes to the inlet pressure resulted in a change to the corrected airflow. This change to the airflow propagated an expansion wave forward into the inlet section, causing the average pressure to adjust, and the cycle continued.

The WRCVC is a mechanical device, presenting the rotating channels to the inlet and exit ports at a frequency directly related to the rotational speed. Airflow will adjust only as fast as these channels present to the inlet port. In this way, the WRCVC behaved similarly to other mechanical devices, such as internal combustion engines, which use a system of valves and pistons to direct airflow through its combustion process. The internal combustion engine exhibits similar airflow versus pressure characteristics at a constant speed.

The time scale for the inlet section was the time computed as if a single particle were to pass through the entire volume, computed as follows:

$$\tau_{inletsection} = \frac{\rho \mathcal{V}}{\dot{m} g_l^3} \quad (4.1)$$

With units:

$$sec = \frac{lb_m}{ft^3} \cdot \frac{in^3}{in^3} \cdot \frac{sec}{lb_m} \cdot \frac{ft^3}{in^3} \quad (4.2)$$

For the design point the inlet section time constant evaluated to be:

$$\tau_{inletsection} = \frac{(0.109933)(6724.18)}{(9.5025)(1728)} = 45ms \quad (4.3)$$

4.2 WRCVC Rotor Timing Analysis

The WRCVC rotor presents a full set of channels to the inlet at a period of $\frac{60}{N}$ where N is the rotor speed in RPM. For a rotor speed of 2100 RPM, the rotor period is $28.6ms$. Based on this time scale and the rig time scale, it can be determined that the WRCVC takes almost two revolutions to clear the inlet section volume. This time scale shows that the choice to use a flow characteristic for the WRCVC was reasonable, because the WRCVC reacts slowly to pressure disturbances.

The integration of the WRCVC performance as a set of correlation curves was done in lieu of a full SCW1D integration into the VOLDYN program. The assumption, identical to the assumption made in Paxson's transient startup performance paper [30], is that the flow quantities, and hence the entire WRCVC balanced cycle solution, at any instant in time, is essentially a steady state solution. Hence the entire dynamic solution, as seen from the perspective of the WRCVC, is a series of steady state solutions, whose inputs are the input total pressure $P0(1)$ and the operating condition.

If the rig volume were smaller, this assumption might not be valid. If the the WRCVC could clear the rig in less than one revolution, then a different analysis technique might be required, possibly including modeling each channel in parallel, with the set of twenty parallel channels being integrated into the VOLDYN model. This condition could also be seen at slow rotor speeds, where flow changes would only be propagated to a subset of channels.

5. DYNAMIC MODEL CONSTRUCTION AND EXECUTION

5.1 Dynamic Model Construction

The dynamic model was implemented as a FORTRAN program constructed to compute the mass flow rates and intrinsic flow conditions of the working fluid at the working stations. The working stations are seen in Table 5.1 with their positions on the rig shown in Figure 5.1 and Figure 5.2. The earlier simplified graphic of the control volume found in Figure 1.6 shows the station layout in relation to the inlets and outlets.

Table 5.1 Lumped volume dynamic model working stations.

Station	Description
0	Upstream main air tank
1	Venturi throat
2	Flow treatment section (largest cross section area)
3	Inlet to the fuel delivery region
4	Flow straightener region before inlet guide vanes
5	Rig exit and WRCVC rotor inlet

5.2 Dynamic Model Initialization

The initialization of the dynamic model is the quiescent condition, with all of the pressures and temperatures set to the reference condition. Since the rig actually starts in this condition, using this condition for initialization allows a time comparison of the rig model versus the test data for conditions all the way from zero flow to the design test points. In addition to the pressure and temperature being set to the reference conditions, all of the mass flow rates are initially set to zero.

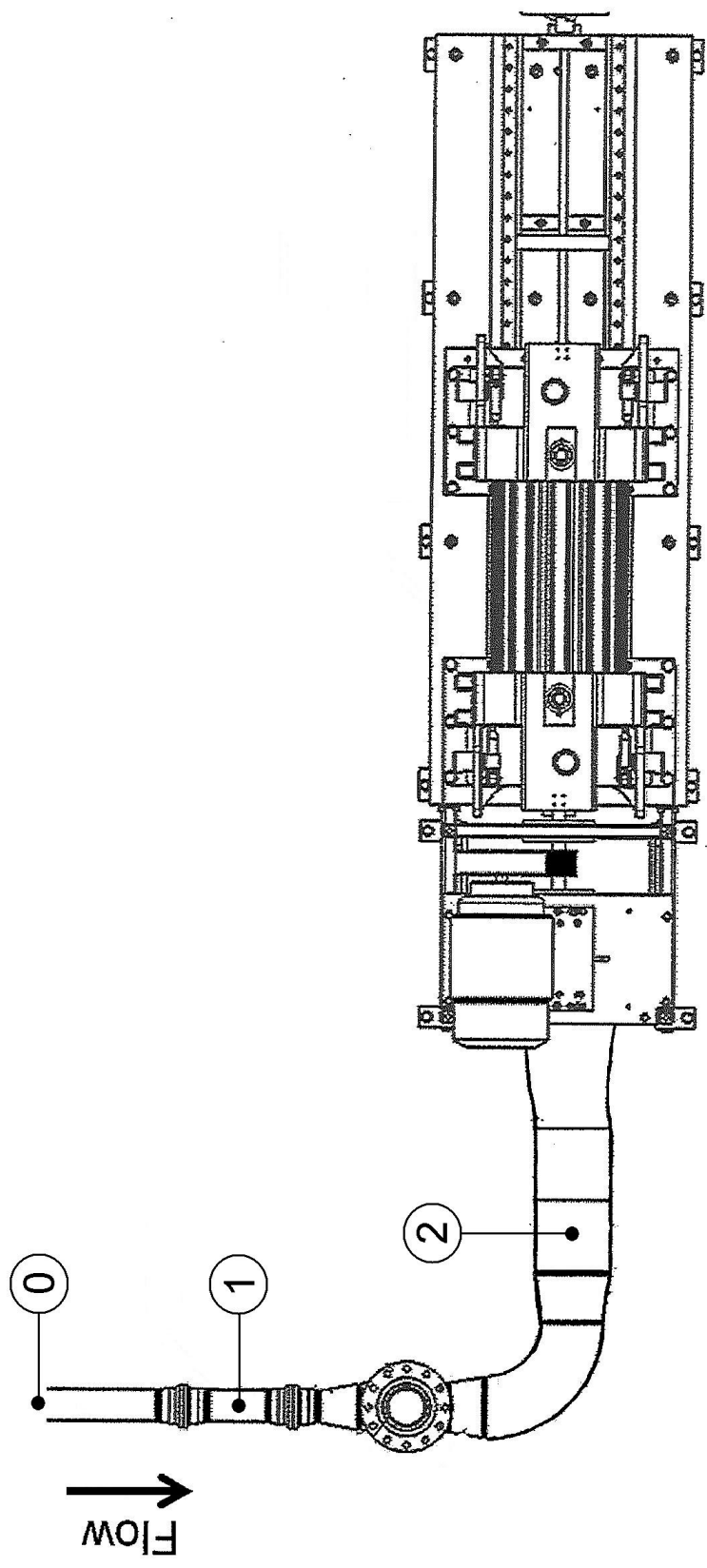


Figure 5.1. Lumped volume dynamic model stations 0, 1, and 2.

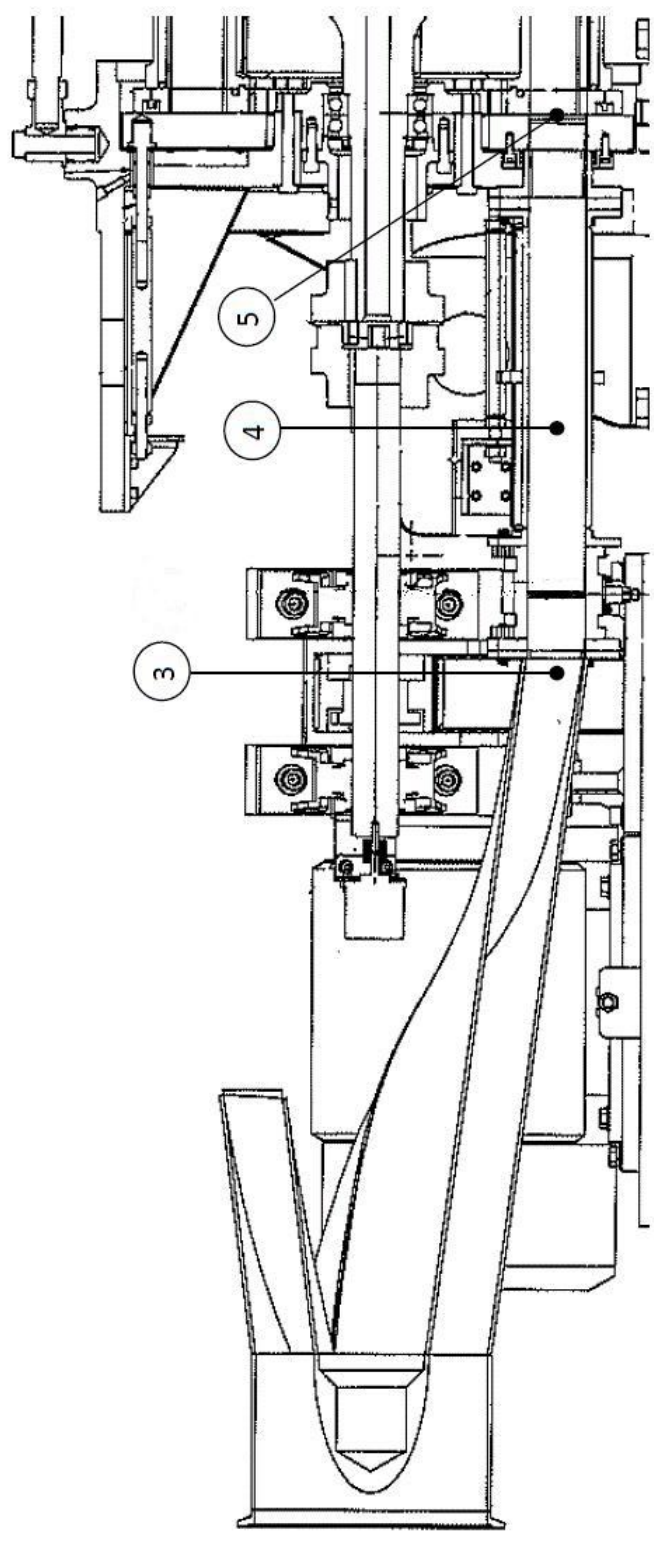


Figure 5.2. Lumped volume dynamic model stations 3, 4, and 5.

5.3 Dynamic Model Volume Computation

The inlet section volumes were computed by a geometric analysis of the hardware, from the venturi to the rotor plane, using the best available drawings. For each part, the upstream and downstream cross sectional areas were computed, and a trapezoidal volume computation was computed using those areas and the measured length. For the more complex hardware, the same technique was used, but longer lengths of ducting were divided into smaller sections for better accuracy. There is a transition duct which goes from a solid pipe geometry, transitions to an annular geometry, then transitions from there to an annular section varying from 360° to the design angular section. Table 5.2 shows the computation of the volume. Summation of the volumes shows that a third of the volume is before the 10 inch diameter by 22 inch long Flow Treatment section, a third is the Flow Treatment section and annular portion of the inlet, and the remaining third is from the annular part of the inlet duct back to the WRCVC rotor.

Table 5.2 Volume computations for WRCVC rig.

-	-	Section	Angle	Section	Area	-
Section	Description	Inlet	Exit	Inlet	Exit	Volume
1	Venturi	360	360	2.545	12.566	30.22
2	Adapter	360	360	12.566	12.566	87.96
3	6x4 Reducer	360	360	12.566	28.274	107.21
4	Burst Disk	360	360	28.274	28.274	395.84
5	6x8 Reducer	360	360	28.274	50.265	206.17
6	8 inch Elbox	360	360	50.265	50.265	972.64
7	8x10 Reducer	360	360	50.265	78.540	450.82
8	Flow Treatment	360	360	78.540	78.540	1727.88
9	Inlet - Straight	360	360	78.540	78.540	116.24
10	Inlet - Nose	360	360	60.265	45.499	317.29
11	Inlet A-C	360	321.71	59.295	61.041	259.33
12	Inlet C-D	321.71	277.47	61.041	62.331	370.73
13	Inlet D-E	277.47	198.63	62.331	51.541	341.62
14	Inlet E-F	198.63	134.80	51.541	39.667	273.17
15	Inlet F-G	134.80	112.30	39.667	36.940	228.67
16	Inlet G-B	112.30	103.42	36.940	35.265	74.91
17	Fuel Inlet Adapter	103.95	103.95	35.446	35.446	140.90
18	Flow Straightener	103.95	103.95	35.500	35.500	514.75
19	Guide Vane Pack	107.0	107.0	36.425	36.425	56.46
20	Seal Plate - Inlet	100.625	100.625	34.255	34.255	51.38
-	Total Volume	in^3	-	-	-	6724.18

5.4 Dynamic Model Execution

The VOLDYN model execution was conducted in the sequence shown in Table 5.3. For each time step, the execution sequence was conducted, and the time was incremented by the chosen time increment. The time increment was kept small enough to allow the volume dynamic model to run in a stable manner, but large enough to prevent any kind of underrun processing due to changes in the values being too small to sum. In most of the execution runs, the time step was 20 microseconds, and data was output in 0.005 to 0.1 second intervals for graphing and study, with closer spaced output for fast changing time periods.

Table 5.3 Lumped volume dynamic model execution steps.

Step	Process
1	Compute main air tank pressure and temperature, nitrogen or fuel tank pressure and temperature based on time curves digitized from the recorded test data.
2	Compute respective flow rates from the static and tank pressures, temperatures, and constituent properties (air, nitrogen, or ethylene).
3	Update the volume averaged density and pressure using the dynamic relations for the next time step.
4	Compute the volume averaged temperature from the density and pressure, using the equation of state.
5	Estimate that the volume averaged properties exist at station 2 as the density, static pressure and static temperature.
6	Use perfect gas relations to compute pressure losses downstream of this station, to compute the stagnation pressure and temperature at the rotor plane.
7	Use the observed operating condition (cold flow, torch on, firing) to determine the flow characteristic of the rotor.
8	Use the stagnation pressure at station 5 and flow characteristic to compute the corrected mass flow of the rotor.
9	Compute the actual mass flow of the rotor based on the corrected value and conditions.

Execution of the model required time dependent inputs. The time dependent inputs include the air pressure and temperature measured upstream of the venturi,

the fuel delivery line pressure and the gas supplied. Figure 5.3 shows the venturi pressure versus time, Figure 5.4 shows the venturi temperature versus time. Because the actual measured values had significant noise, the markers on these plots represent an estimation of the value, input to the program as an interpolated curve as a function of time. Using an interpolated value ensured the stability of the program as well.

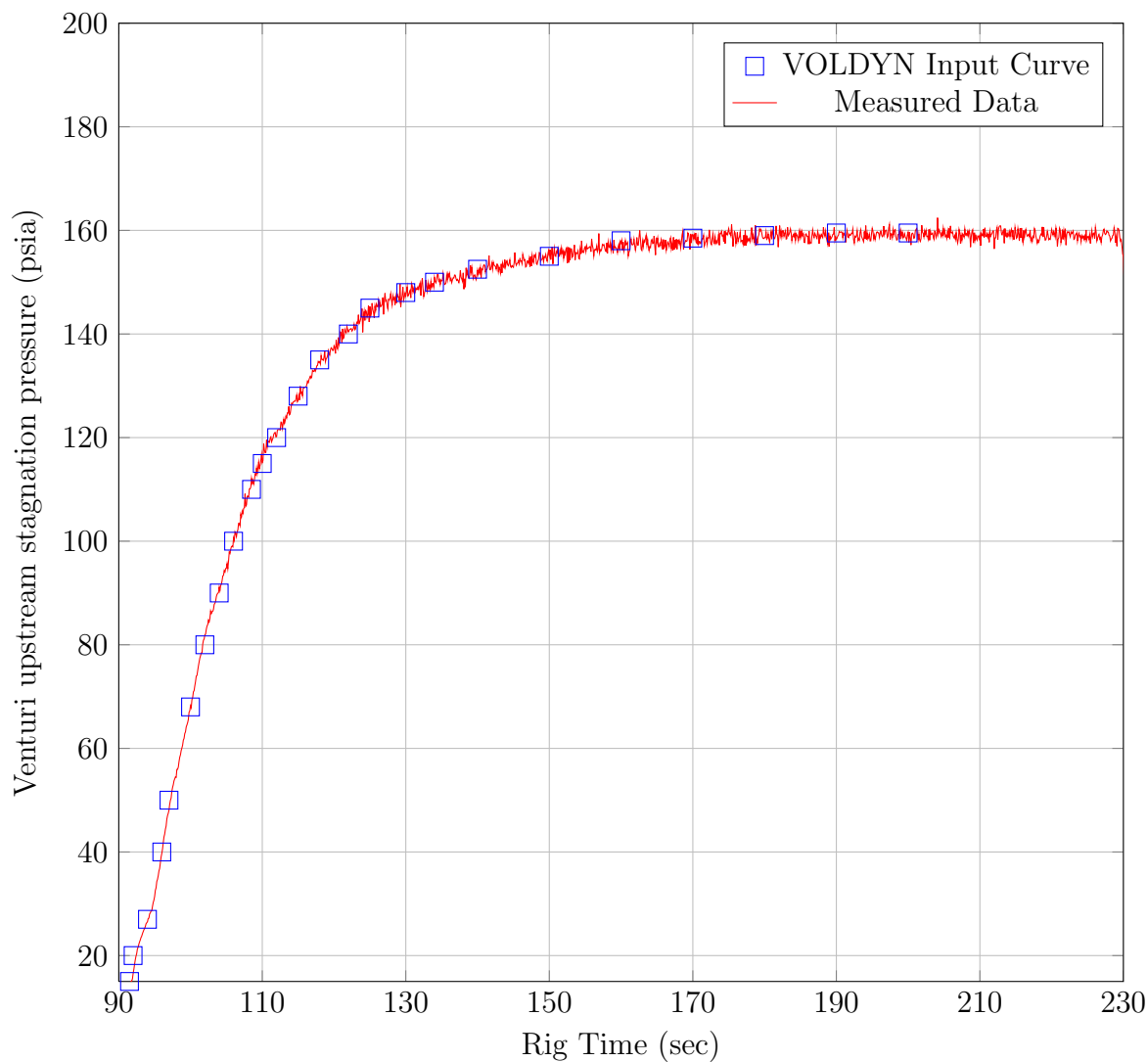


Figure 5.3. WRCVC rig venturi upstream stagnation pressure.

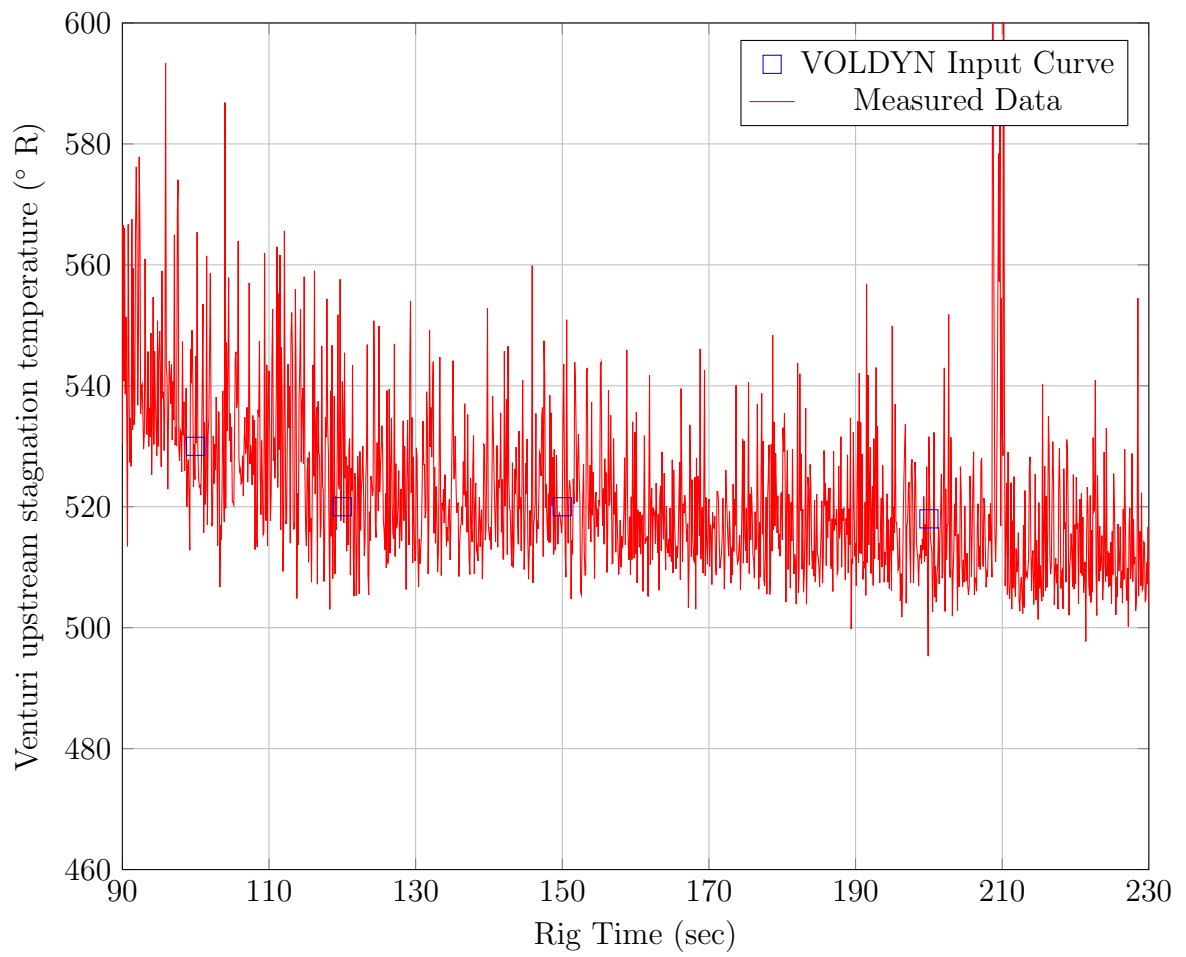


Figure 5.4. WRCVC rig venturi upstream stagnation temperature.

Figure 5.5 shows the input pressure at the fuel nozzles versus time. Again the measured values contain variation, so the input to the VOLDYN program required interpolated values for data. The interpolated values contain hard corner points to signify the rapid change in the pressures. The pressure of approximately 60 psi represents the time that the nitrogen purge is on. The pressure of approximately 180 psi represents the time that the ethylene fuel is on. These 3 inputs are essentially the only primary inputs to the VOLDYN program. Minor inputs include the specific heat values of the nitrogen purge and ethylene fuel. The propane torch operation is not accounted for in the VOLDYN model because it is downstream of station 5, except that the torch operation causes a small shift in the exit flow characteristic of the WRCVC.

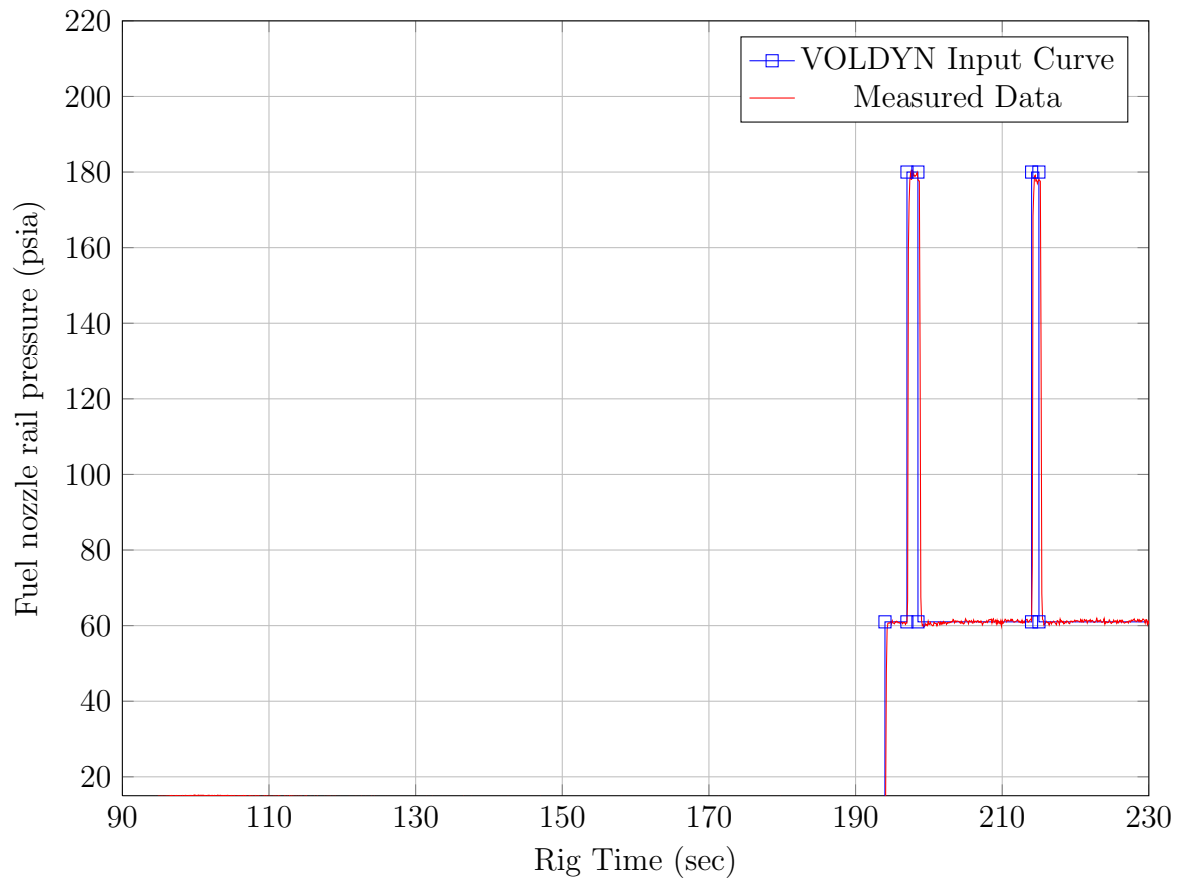


Figure 5.5. WRCVC rig fuel rail pressure.

5.5 Dynamic Model Results

During VOLDYN execution, data was output at 0.1 second intervals, except during the test transition times, where the output interval was reduced to 0.005 seconds. This allowed the program to output the rapidly moving pressures and the WRCVC mass flow rate. The charts shown in this section are time plots of the data generated by the VOLDYN program, and where data was gathered for the running rig, the reduced test data is also plotted. While the rig test data was gathered in 0.002 second increments, the LaTeX software cannot handle the length of that dataset, so the data in the plots is limited to 0.1 second increments.

5.5.1 Airflow Comparison Results

The main air (venturi) mass flow computation correlated exactly with the measured values, as seen in Figure 5.6. This graph shows the VOLDYN computed versus measured values from the start of the main air at 90 seconds, to the end of the computation at 230 seconds. The correlation in large part was due to the simplicity of the equations for computing the venturi air flow, which are the air flow calculations shown in Section 2.4. Both the data reduction system used for the rig testing and the VOLDYN model used these same equations, which are primarily driven by the upstream pressure. One small difference should be noted in the plot at the very start; the data reduction system appears to not account for the Mach number in the unchoked region, and computes a higher mass flow at the initial values of pressure. In Figure 5.7, the VOLDYN computed and rig test reduced values are seen in the 190 to 220 second region. In all of the graphs, the reduced data was subject to the effects of noise in the measurements in the 208.5 to 212.5 second region, which is when the torch's spark igniter was switched on. The effect of noise can explain the reduced rig air flow measurement in this time frame.

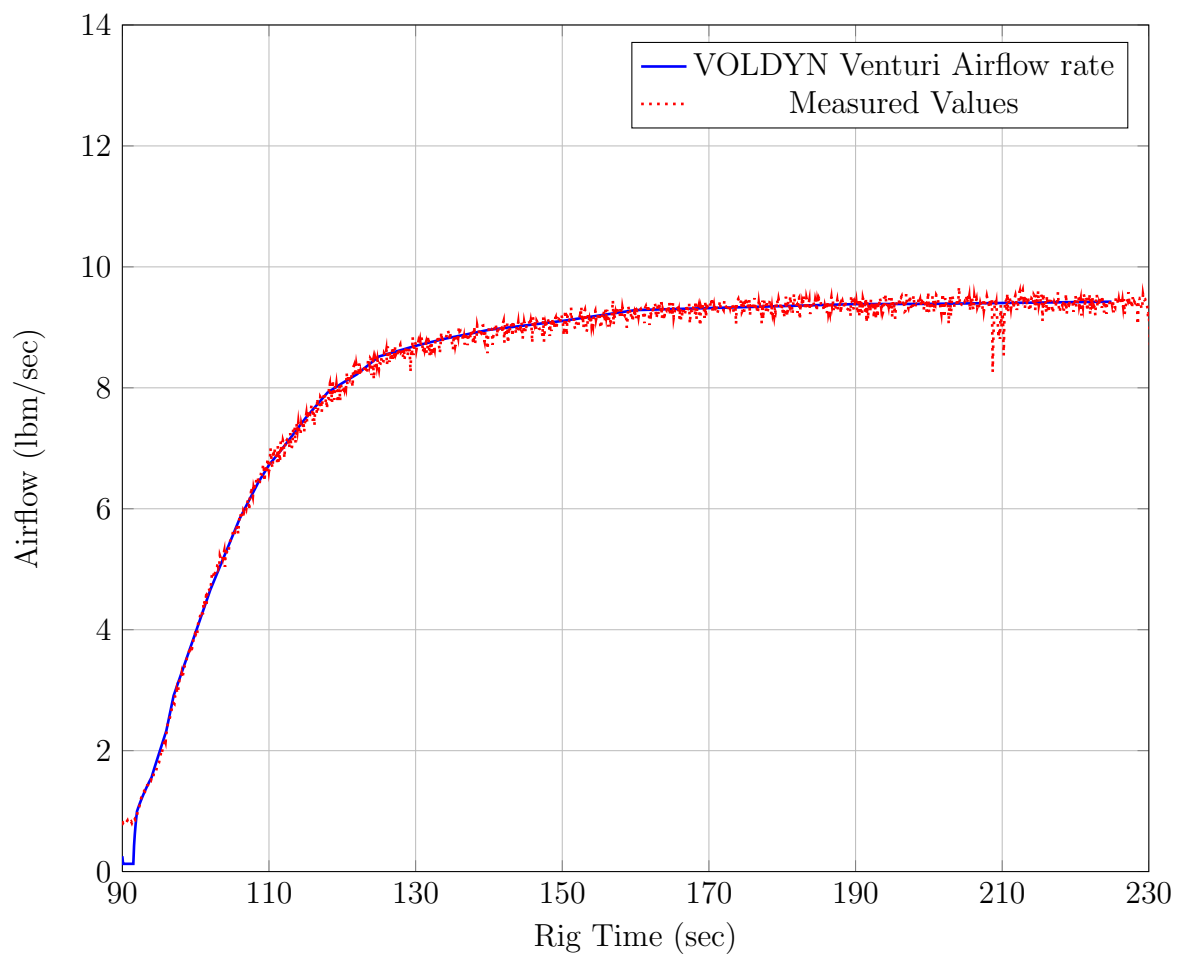


Figure 5.6. WRCVC rig venturi flow rates.

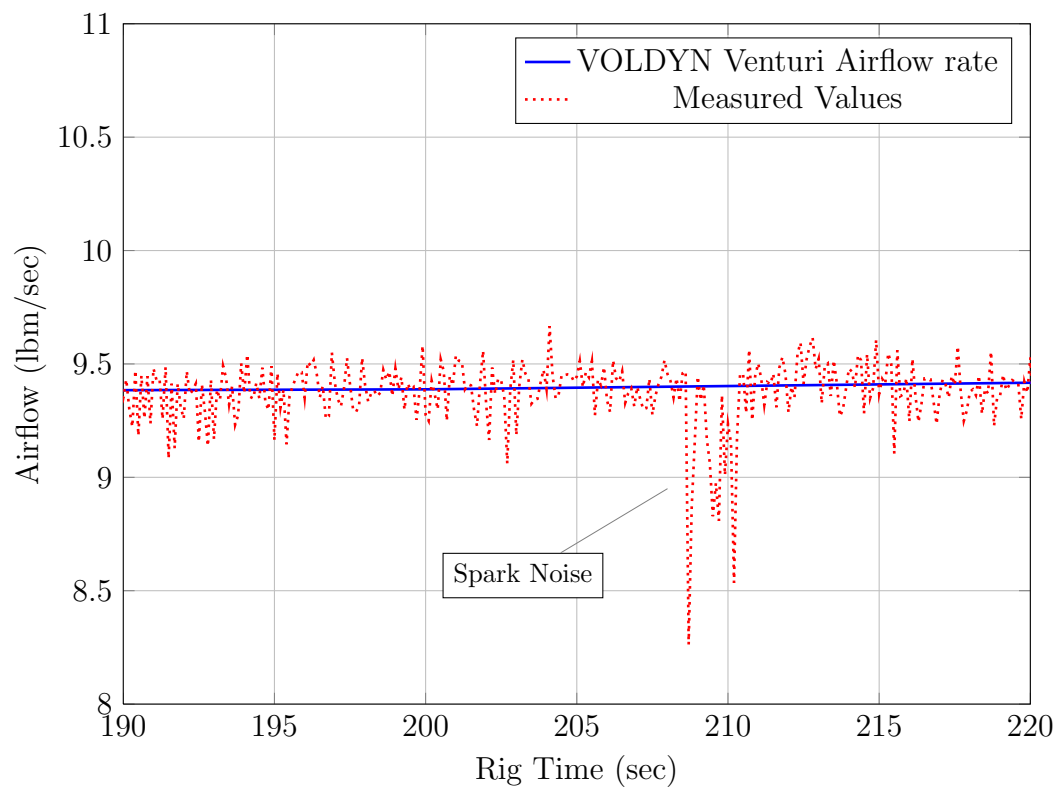


Figure 5.7. WRCVC rig venturi flow rates - detailed.

One other important value to observe is the accumulation rate of mass in the control volume. A positive value indicates a compression of the mass and a negative value indicates an expansion of the mass. Figure 5.8 shows the computed mass imbalance for the test run. A detailed view from 190 to 220 seconds is shown in Figure 5.9, and a micro plot from 214.8 to 215.2 seconds is seen in Figure 5.10.

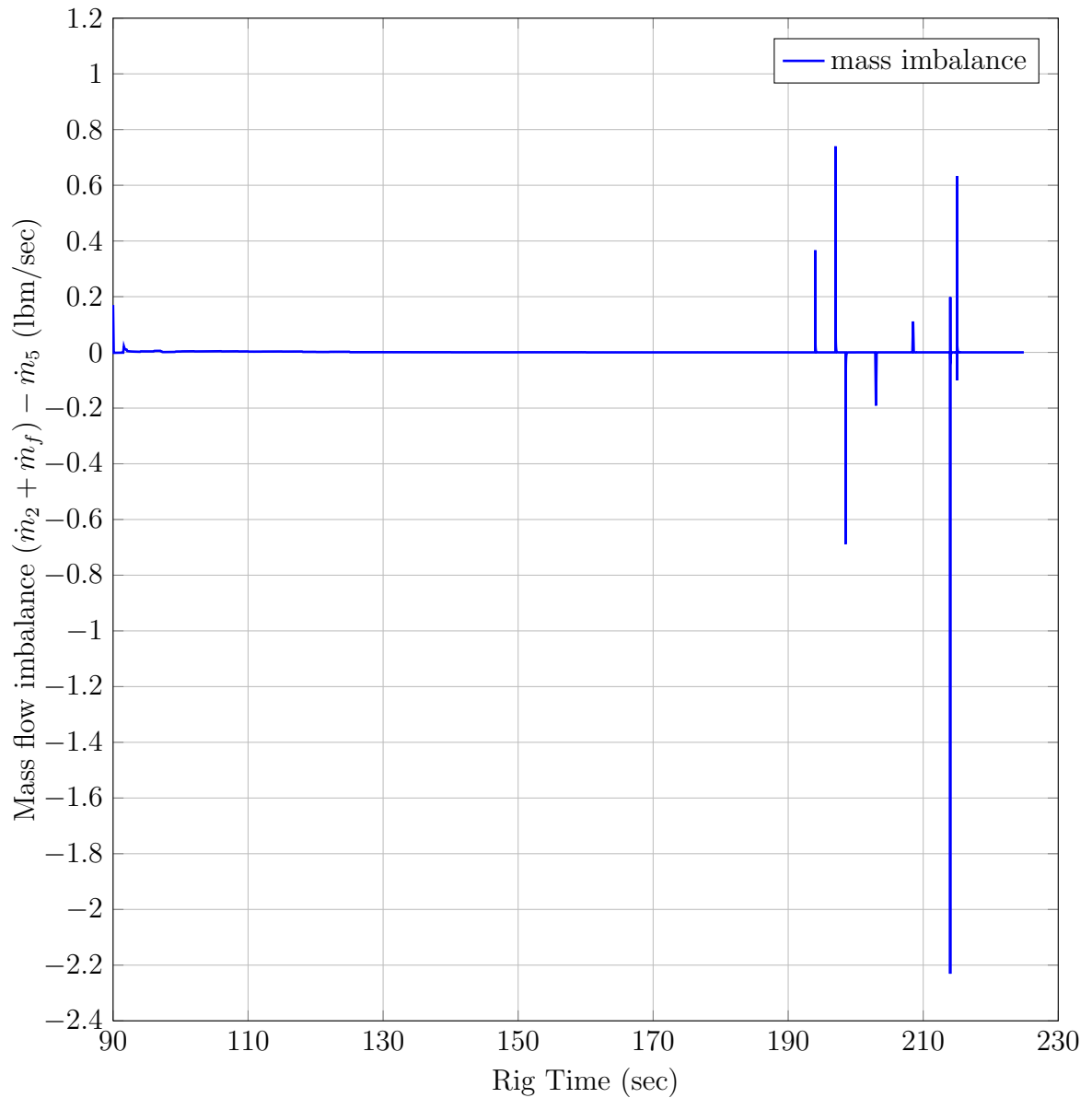


Figure 5.8. VOLDYN Computed mass flow imbalance.

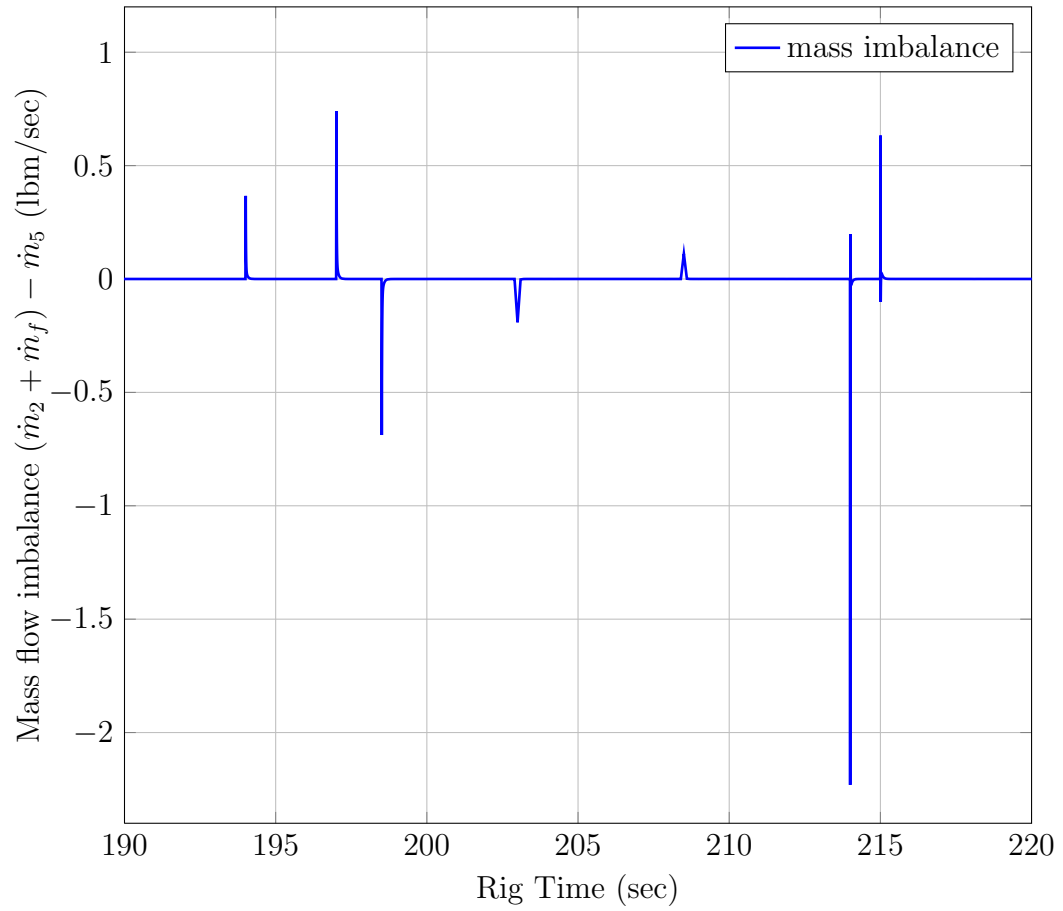


Figure 5.9. VOLDYN Computed mass flow imbalance - detailed view.

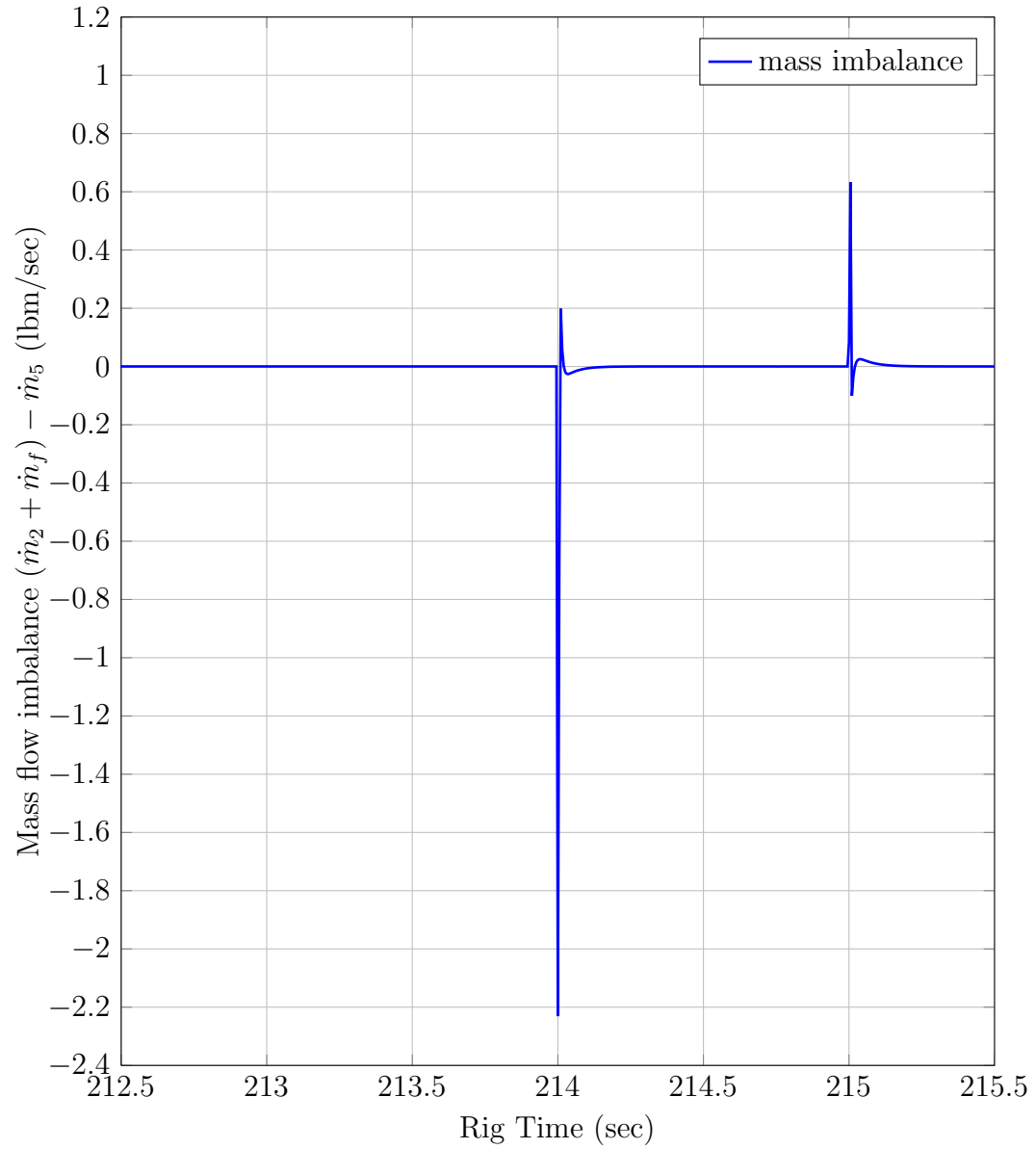


Figure 5.10. VOLDYN Computed mass flow imbalance - micro view.

5.5.2 Pressure Comparison Results

The main purpose of the VOLDYN program was to predict the pressures in the inlet section, to understand the pressure losses caused by the fuel delivery system and by the cross flow injection. Prediction of the pressure losses caused by the flow straightener walls and inlet guide vanes was a secondary purpose. Another secondary purpose was to study and predict the pressure variation at the WRCVC inlet, as well as the WRCVC airflow variation, during the condition transition times. The VOLDYN program was executed with the rig test sequence as specified in the previous section, computing all three pressure loss components. It will be shown in this section that the results were very close to those measured by the instrumentation.

The overall computation solution pressures can be seen in Figure 5.11. This plot shows the volume average pressure PS2 as well as the stagnation pressures at Stations 3, 4, and 5. This plot dramatically shows the amount of pressure loss across the fuel nozzles, and shows the additional loss during fuel and purge flow addition. This plot starts at the 90 second main air on time, and continues to just before the 230 second test end. Figure 5.12 shows the drag forces on the fuel nozzles, the inlet guide vanes, and the flow straightener walls. Figure 5.13 shows the individual $\Delta P/P$ values for all four loss mechanisms. A table of the computed values for four steady-state points is also seen in Table 5.4. In this table, the reynolds numbers, friction and drag coefficients, $\Delta P/P$ values can be seen.

The most important comparison to make is between the computed values at the fuel nozzle measurement station (3) and the test data gathered during the test. This comparison is influenced by the pressure losses and by the dynamics of the air system. Figure 5.14 shows the direct comparison between the computed values of PT3 and the measured rig values. In this plot, starting again at the 90 second main air on time, and ending just before the 230 second test end, the computed value is seen to track fairly closely with the measured values. During the startup transient, the

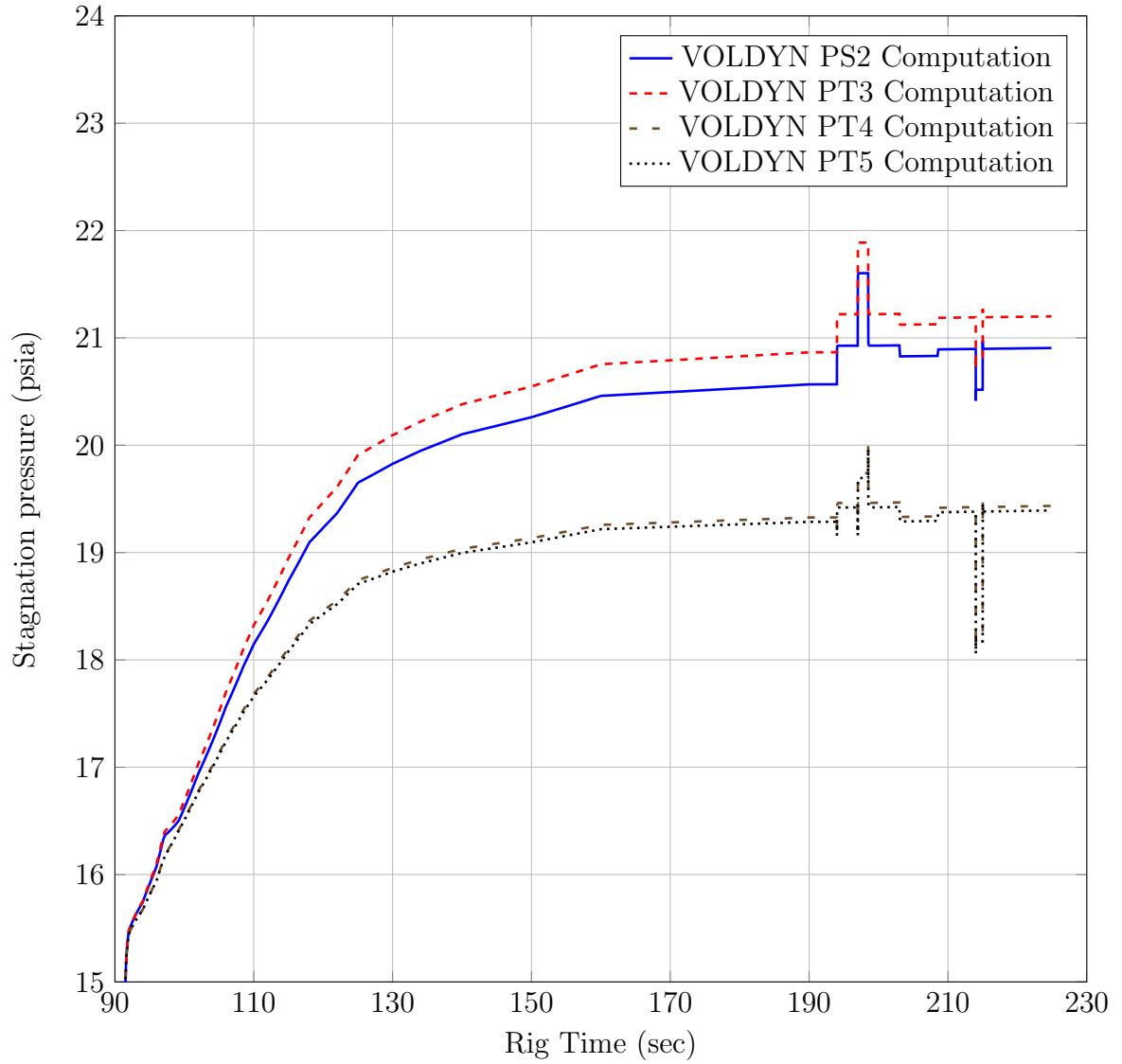


Figure 5.11. VOLDYN computed volume average pressure PS2, and stations 3, 4, and 5 stagnation pressures.

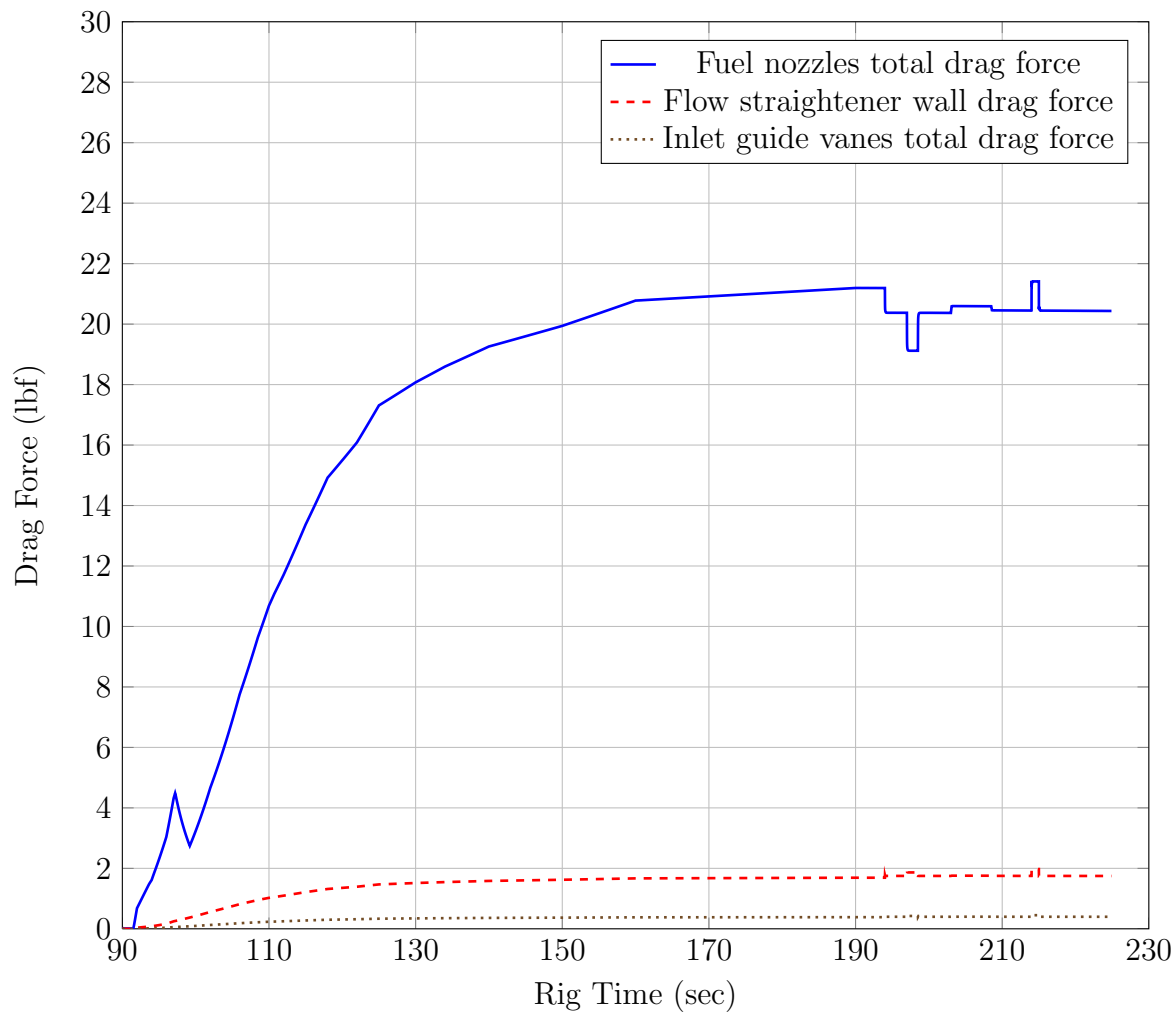


Figure 5.12. VOLDYN Computed drag forces.

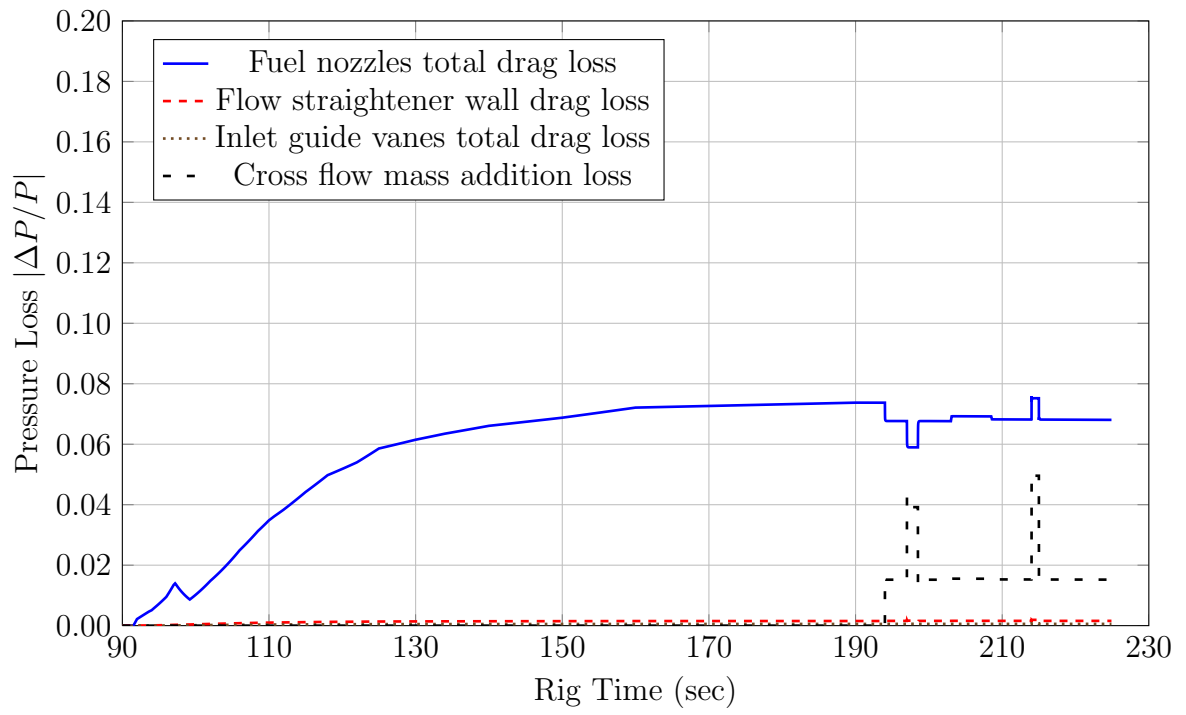


Figure 5.13. VOLDYN Computed drag losses.

Table 5.4 VOLDYN computed pressure loss values.

Parameter	Value	Value	Value	Value
Time	190.0	194.5	198.0	214.5
Mass imbalance	9.88E-05	3.98E-05	4.01E-05	1.46E-04
PT3	20.865	21.221	21.888	20.817
\dot{m}_f/\dot{m}_{air}	0.00	0.0202	0.0594	0.593
$(\Delta P/P)_{massaddition}$	0.00	0.0152	0.0392	0.0496
Re_D	1.547E+08	1.466E+08	1.346E+08	1.573E+08
C_D	0.386	0.385	0.384	0.386
$F_{pressuredrag}$	21.19	20.37	19.12	21.41
$(\Delta P/P)_{pressuredrag}$	0.0737	0.0677	0.0590	0.0752
PT4	19.327	19.462	19.739	18.219
$Re_{L,flowstr}$	2.590E+09	2.584E+09	2.587E+09	2.956E+09
$C_{friction}$	0.00389	0.00390	0.00390	0.00380
$F_{frictiondrag,flowstr}$	1.69	1.75	1.86	1.97
$(\Delta P/P)_{flowstr}$	0.0015	0.0016	0.0017	0.0019
$Re_{L,igv}$	2.769E+08	2.762E+08	2.765E+08	3.160E+08
$C_{friction}$	0.00609	0.00610	0.00610	0.00594
$F_{frictiondrag,igv}$	0.39	0.40	0.43	0.45
$(\Delta P/P)_{igv}$	0.0006	0.0006	0.0006	0.0007
PT5	19.286	19.420	19.694	18.171

measured pressures were initially computed slightly higher than the measured values, with the error reversing direction in the intermediate region, and becoming nearly zero when the air flow stabilizes. This pressure error is most likely caused by the use of the single volume spacial discretization, which ignores the pressure losses in the flow treatment section and the elbow.

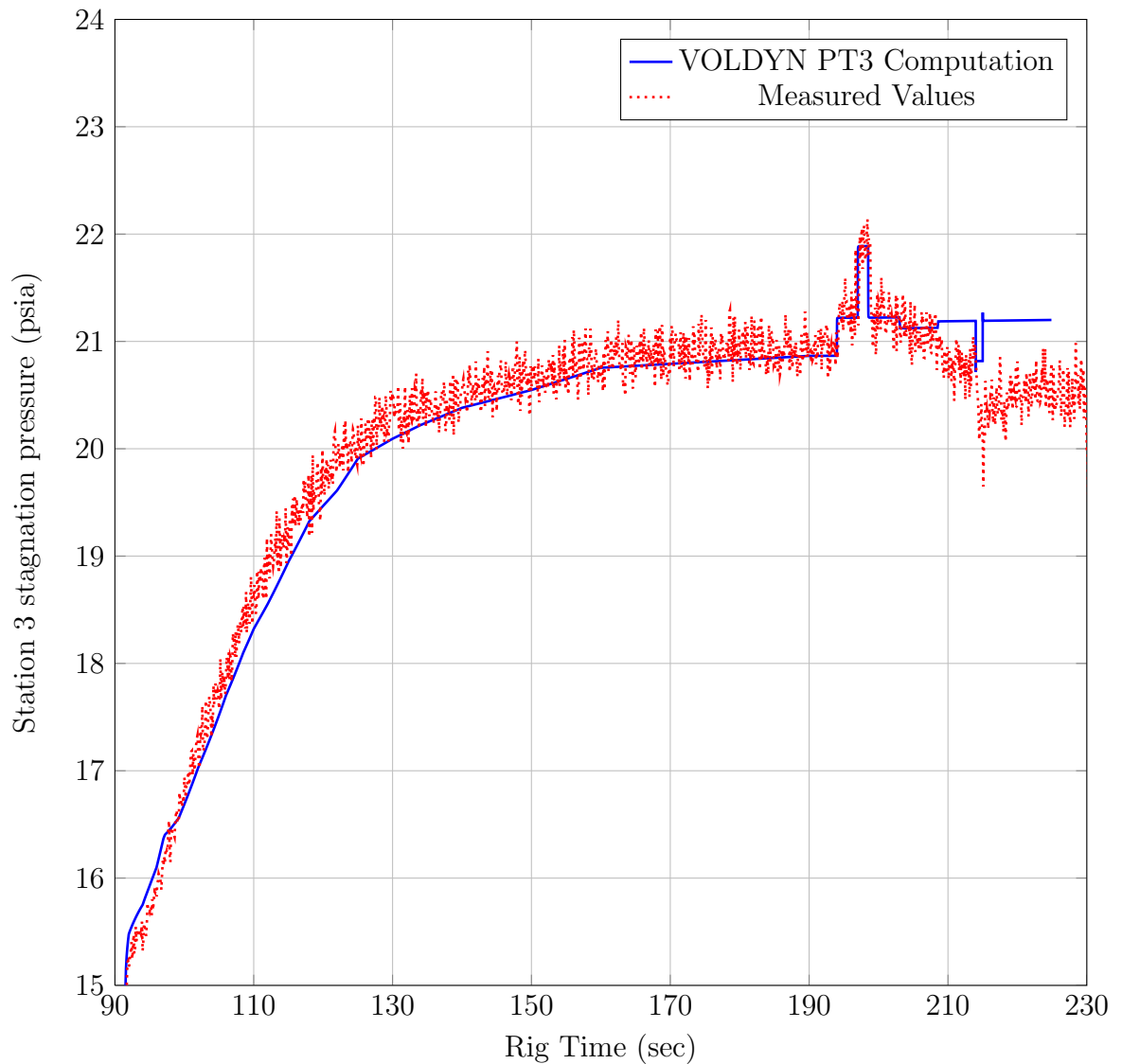


Figure 5.14. WRCVC rig station 3 stagnation pressure.

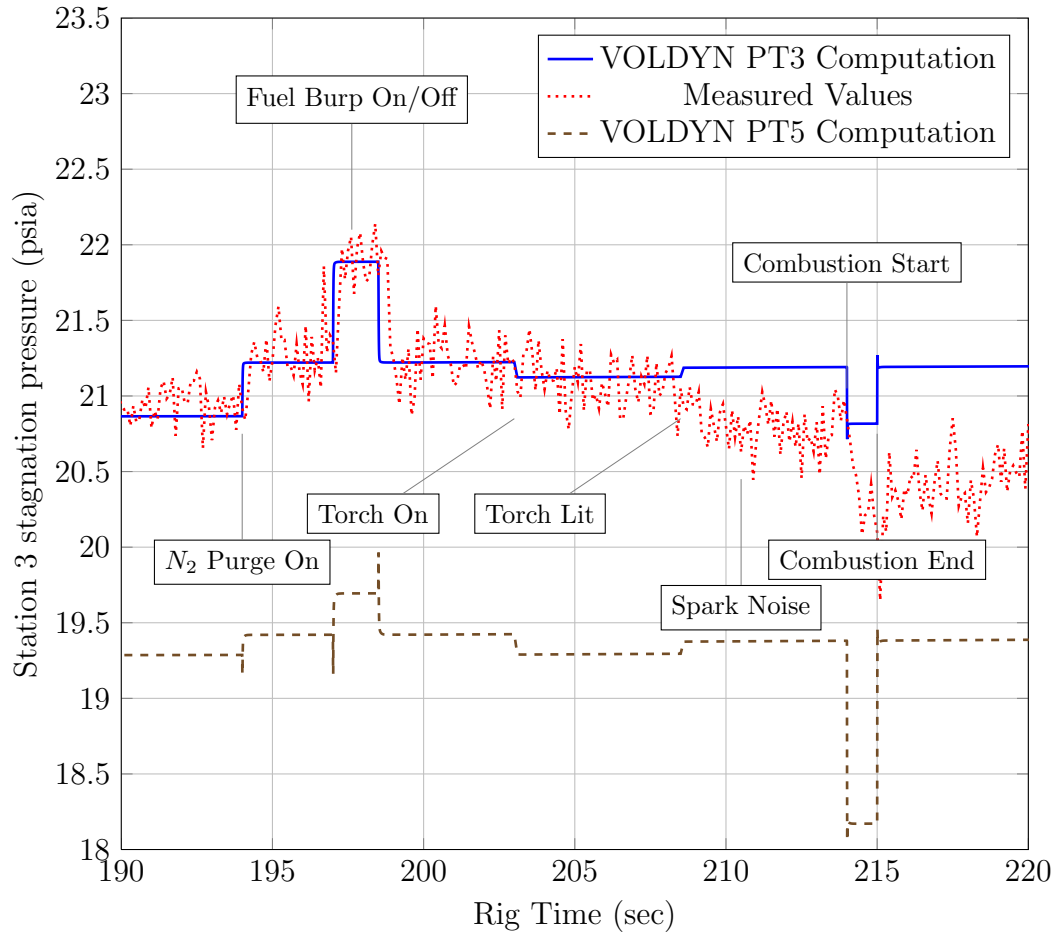


Figure 5.15. WRCVC rig station 3 stagnation pressure - detailed.

Figure 5.15 shows a close up comparison of the VOLDYN computed PT3 values against the measured test data in the range of 190 seconds to 220 seconds, where most of the test events occurred. The events causing the largest changes in this pressure were at the 194 second and 197 second marks. The 194 second mark is the start of the nitrogen purge, and the 197 second mark is the start of the fuel burp segment. These two events increased the total mass flow entering the WRCVC, with the volume average pressure increasing to accommodate the additional mass flow. The change in pressure shifted the operation of the WRCVC to a new point on its operating characteristic, with the accompanying higher flowrate matching the total

flowrate when finally stabilized. At this stabilized condition, the non-dimensional inlet pressure $P0(1) = 1.3401$. Figure 5.16 shows a theoretical fuel distribution at the nominal inlet pressure, while Figure 5.17 shows the shift in the fuel distribution at the actual operating pressure at the 198 second mark.

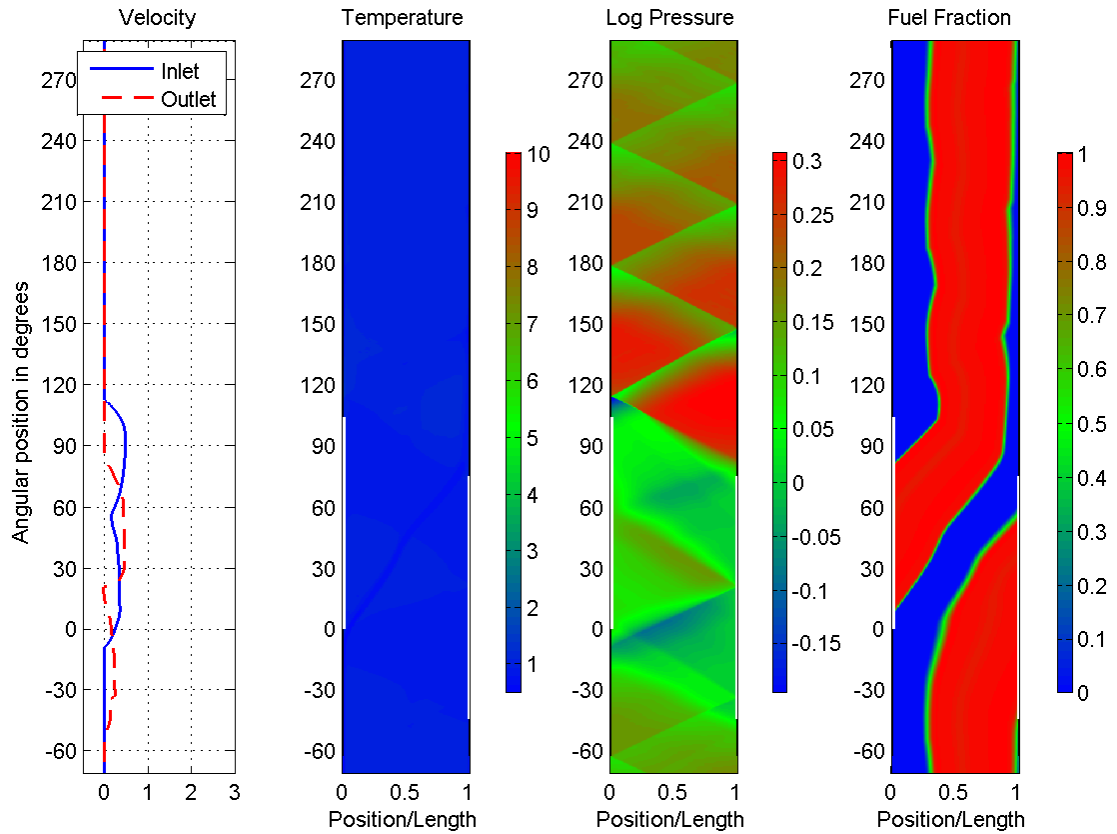


Figure 5.16. WRCVC Cold Flow condition temperature, density, fuel fraction for the nominal inlet pressure, with fuel delivery on.

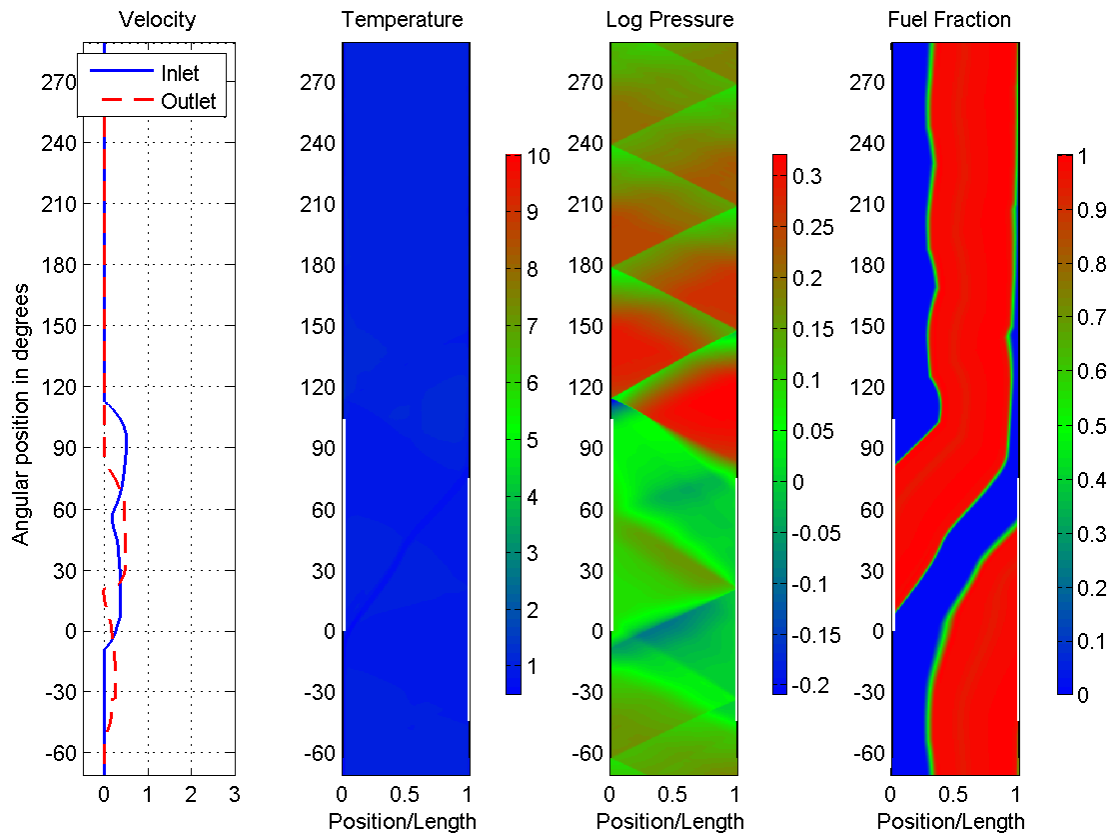


Figure 5.17. WRCVC Cold Flow condition temperature, density, fuel fraction for the actual inlet pressure during fuel burp segment.

The computation of stagnation pressure at station 3 is very close to the measured data in the cold flow region. This cold flow tracking of pressures during the rapid addition of nitrogen purge and ethylene fuel indicates that the VOLDYN model is predicting the upstream volume conditions accurately. But during and after the torch lighting segment, the correlation diverges. At $t = 208.5$ seconds, the torch spark was started, and in an earlier Figure (5.7) a dip in the measured pressure appears to be caused by noise in the data system, so the dip in the fuel nozzle pressure in this same region, up until $t = 212.5$ seconds, could be attributed to the spark noise. Another explanation might be related to the effect of the torch on the WRCVC operation. The actual shift in the operating line of the WRCVC could be more than predicted. The pressure variation between computed and measured values appears to lessen just before combustion starts, indicating the variation may most likely be due to spark noise.

At $t = 214.0$ seconds, the introduction of fuel to the system causes the operating condition to move to the firing condition. The difference between the conditions at $t = 198.0$ seconds and $t = 214.0$ seconds is the presence of combustion, and the change in pressure is significant. In the fuel burp segment, the pressure is a full 1 psi higher than at the nominal segment (before the nitrogen purge), but during the firing segment, the pressure drops. This is also seen in Matsutomi's paper [4], where a graphic shows the pressure dropping 0.5 psi for a different test run. The operating point for the firing condition, at the very start of the firing sequence, is seen in Figure 5.18.

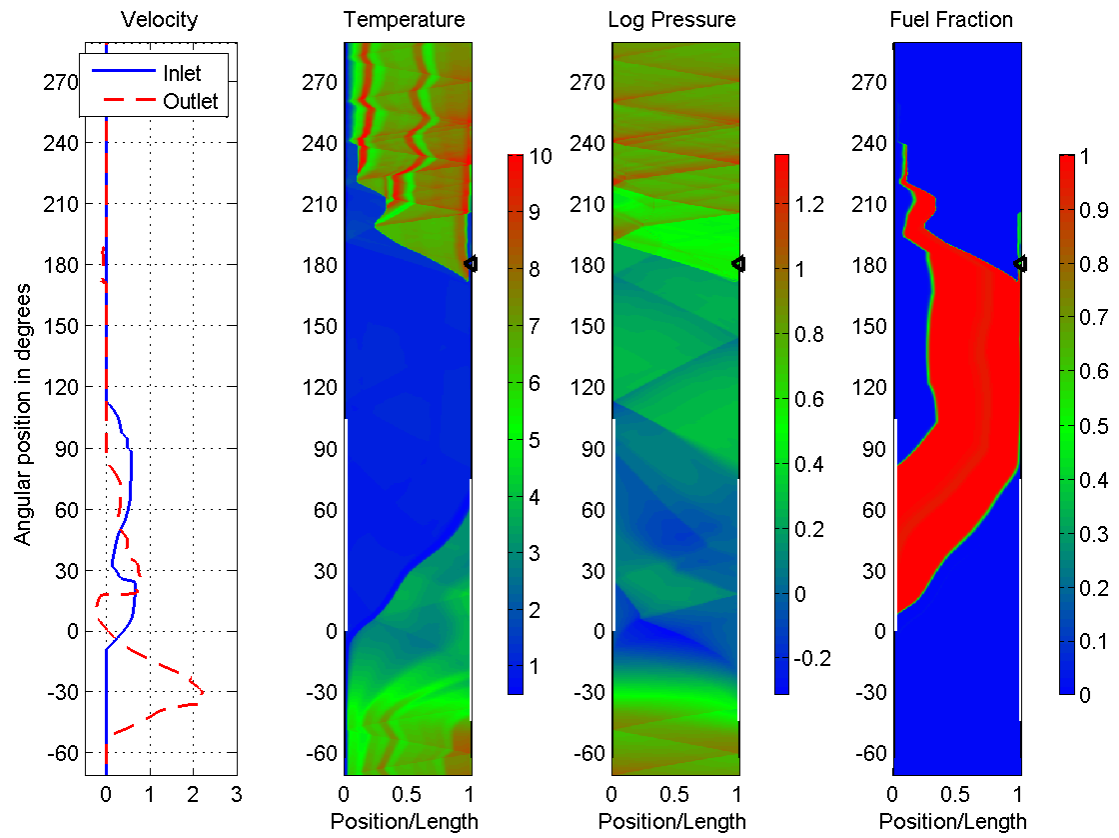


Figure 5.18. WRCVC Firing condition temperature, density, fuel fraction for the actual operating inlet pressure.

After combustion starts, the computed pressure and the measured pressure diverge significantly. This is seen in the graph starting at $t = 214.0$ seconds. The most likely explanation of this divergence is the drop in WRCVC rotor speed. A plot of rotor RPM, seen in Figure 5.19, show a 40 RPM droop in speed, during the firing portion of operation. This speed droop, which is not accounted for in the current version of the VOLDYN program, will change the flow characteristic of the WRCVC, and is the most likely cause of the pressure difference between computed and measured. The effort to add a speed dependent component to this analysis is significant. If attempted, a tradeoff study should be undertaken, between developing a correlation method for multiple speeds and pressures, and actually integrating the SCW1D program into the VOLDYN program. A comparison of the pressure-flow characteristic shift between the 2100 RPM start point and a theoretical 2058 RPM end point is shown in Figure 5.20. This assumes the fuel nozzle placement and flow have not changed. The characteristic shift does not explain the change in pressure during the combustion process and resulting change in rotor RPM.

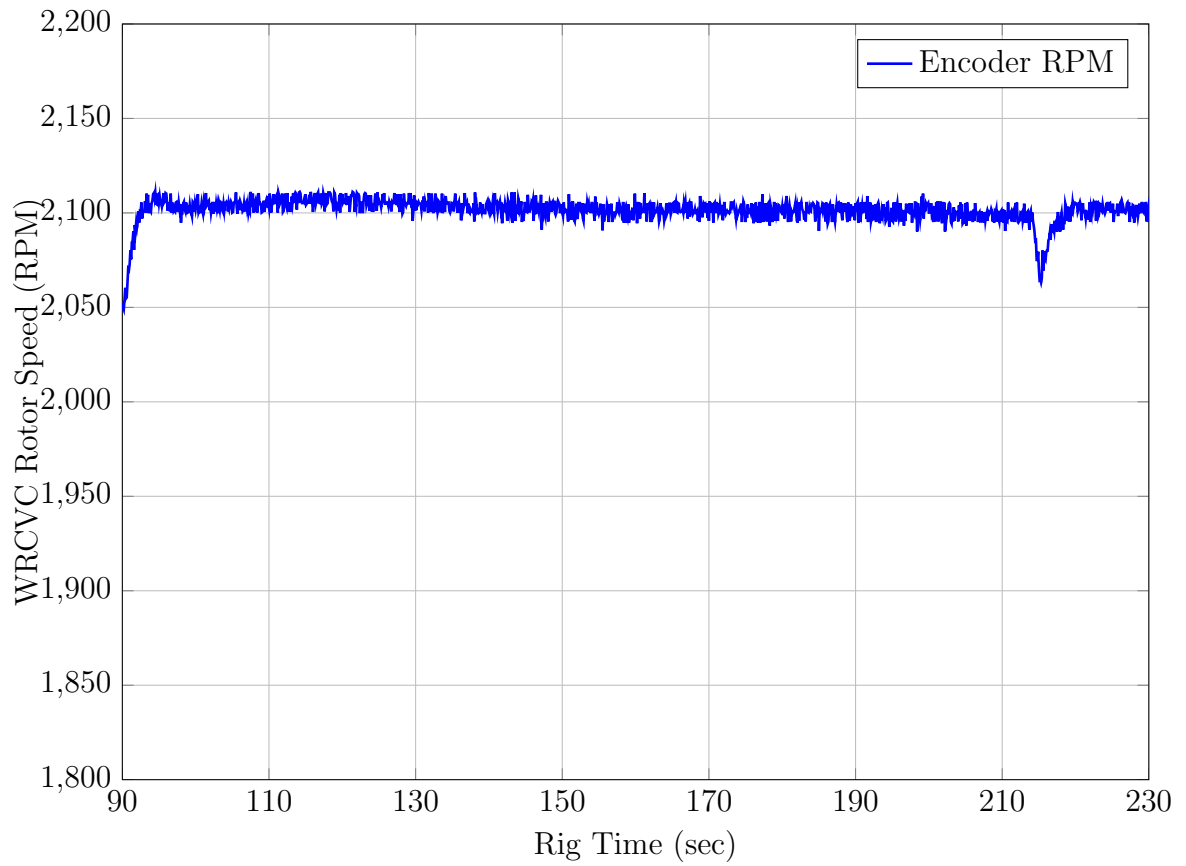


Figure 5.19. WRCVC rotor speed vs rig time.

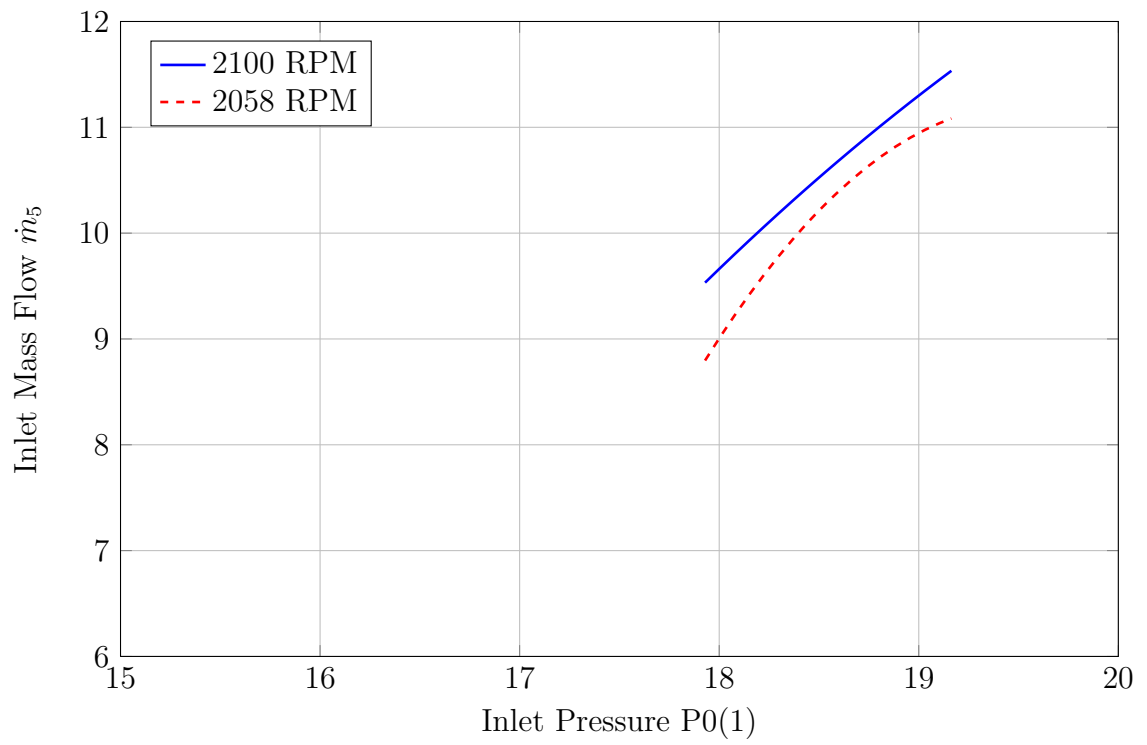


Figure 5.20. RPM dependent pressure-flow characteristics.

5.5.3 WRCVC Operation Results

The final purpose of this thesis is to show, in detail, the estimation of the transient operation of the WRCVC. Refer to Section 4.2 for the explanation of the WRCVC integration into the VOLDYN program.

The results of the analysis are presented here with limited interpretation. In Figure 5.21 the computed WRCVC inlet airflow, which is the computed exit airflow of the inlet section, is plotted against time for the 90 to 230 second total test time frame. A second figure is provided, from 190 seconds to 220 seconds, showing the detail in that time frame, as described previously. This is Figure 5.22, and shows the rapid change in flowrate during the one second combustion process. The features to note in this plot are twofold.

The first feature is that during the torch transients, the flow increases slightly and then returns to its previous value. This is due to the fact that the torch does not change the upstream mass flow, but rather shifts the WRCVC's operating line due to it being at a different condition (torch on, torch lit). Each time the torch changes its state, at the previous value of inlet pressure, the WRCVC briefly changes its flow due to the shifted characteristic. In response to the flow change, a weak expansion or compression wave is propagated into the inlet section, whose reaction is seen as a change in the upstream volume averaged pressure. This change in pressure shifts the operating line on the WRCVC's pressure flow characteristic until its mass flow matches the upstream mass flow. The entire process is finite in time, spanning a $200ms$ timespan.

The second feature on the plot is the equivalent increase in mass flow during the firing segment (214-215 seconds) and during the fuel burp segment (197-198.5 seconds). This is another indication that the VOLDYN program is working properly. Since the WRCVC mass flow is only determined by the upstream pressure and the operating

condition (assuming constant upstream total temperature), the equivalent increase in mass flow matching the fuel burp value shows that the VOLDYN computations are correct.

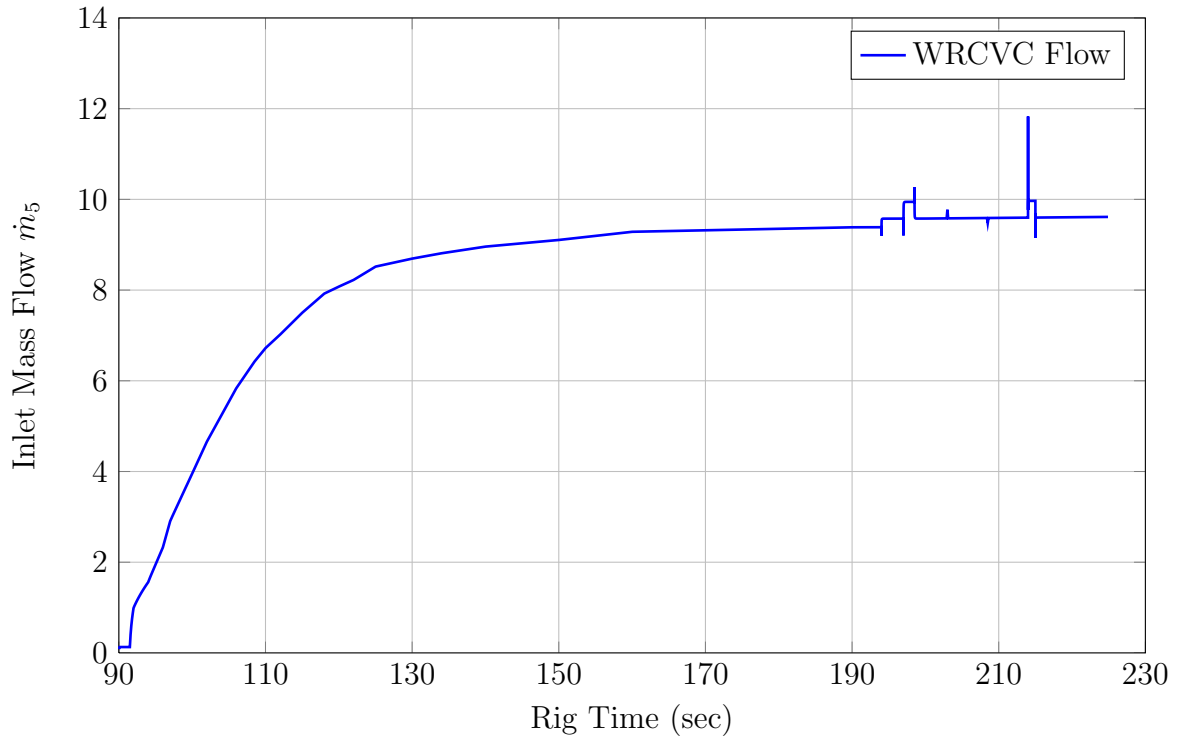


Figure 5.21. VOLDYN computation of WRCVC flow vs time.

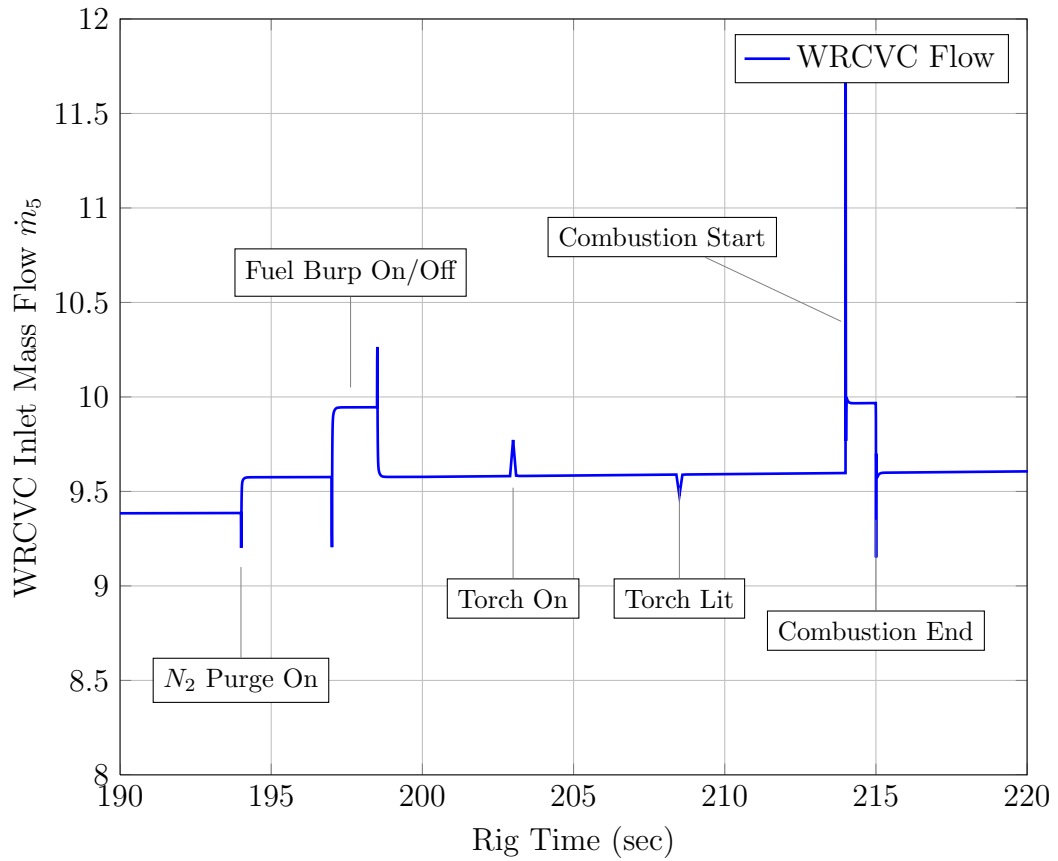


Figure 5.22. VOLDYN computation of WRCVC flow vs time - detailed.

In the previous Figure 5.11 the PT5 pressures are seen. This data is repeated in non-dimensional form in Figure 5.23, for the 90 to 230 second test period. Additional detail is shown in Figure 5.24 for the 190 to 220 second detail period. In these plots the pressure variations seen by the WRCVC are seen to be large enough to cause the brief swing in the mass flows. One matter to study is if the pressure and flow changes are significant enough to cause the WRCVC experience a “blowout” event or to cause unburned fuel to be fed into the exhaust. An x-t plot of the Firing condition at the maximum pressure achieved by the rig is seen in Figure 5.25. In this plot the fuel is too close to the exhaust closing location, which could result in fuel spillage out of the exhaust port, due to the finite width of each channel. To prevent fuel spillage, the fuel should not approach the right end wall until one channel width past the end of the exhaust closing angle.

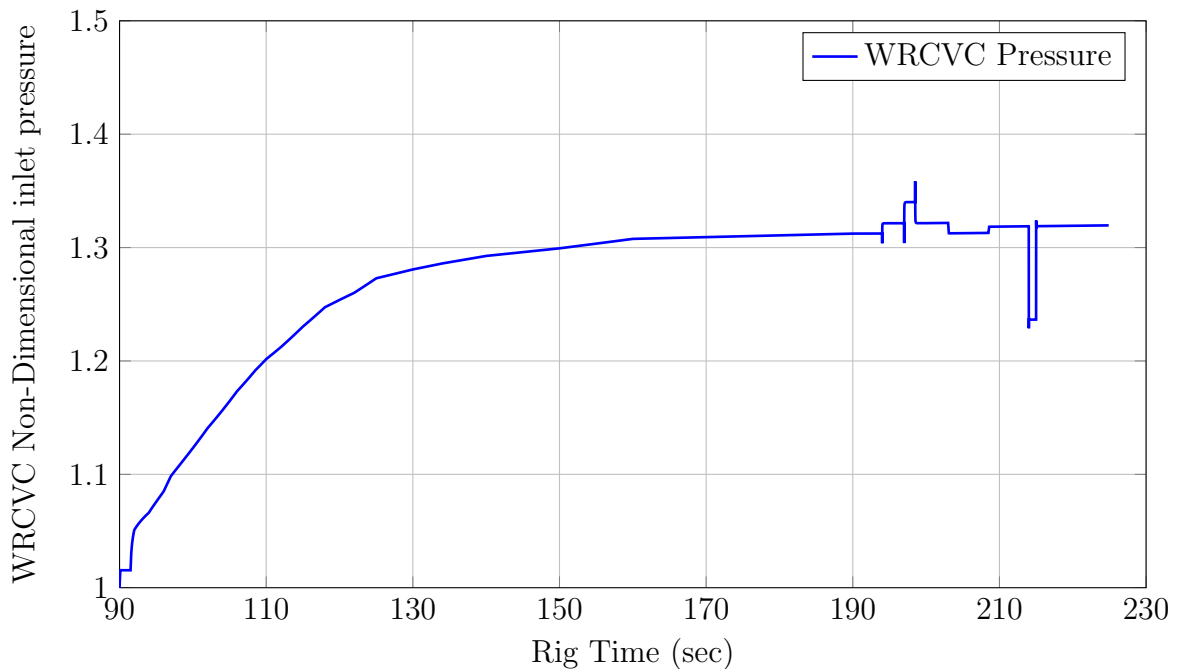


Figure 5.23. VOLDYN computed non-dimensional WRCVC inlet pressure vs time.

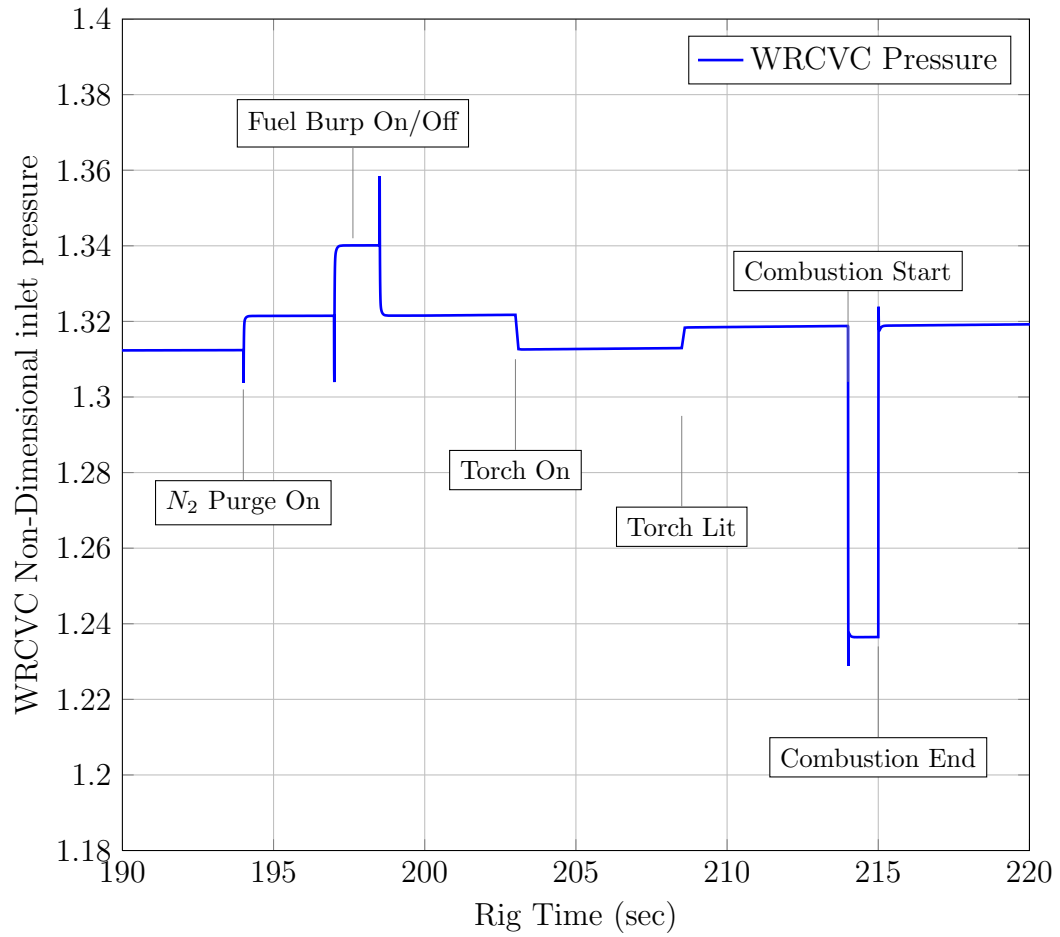


Figure 5.24. VOLDYN computed non-dimensional WRCVC inlet pressure vs time - detailed.

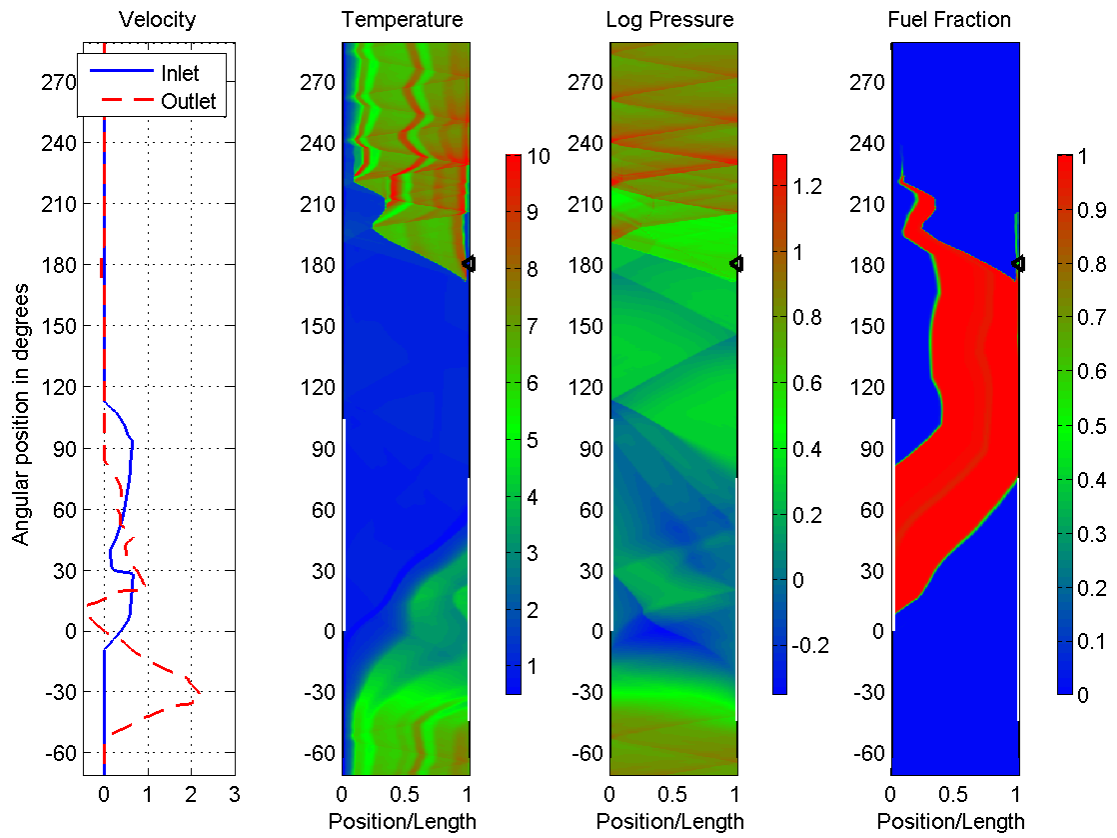


Figure 5.25. WRCVC Firing condition temperature, density, fuel fraction for the actual operating inlet pressure.

In the final Figure 5.26, the airflow is plotted versus the pressure, in the same fashion as in Figure 3.14, and the tracking of the flow along each characteristic can be clearly seen. The two plots can be overlaid to illustrate the shifting of the flow characteristic of the WRCVC for the entire 90-230 second test period.

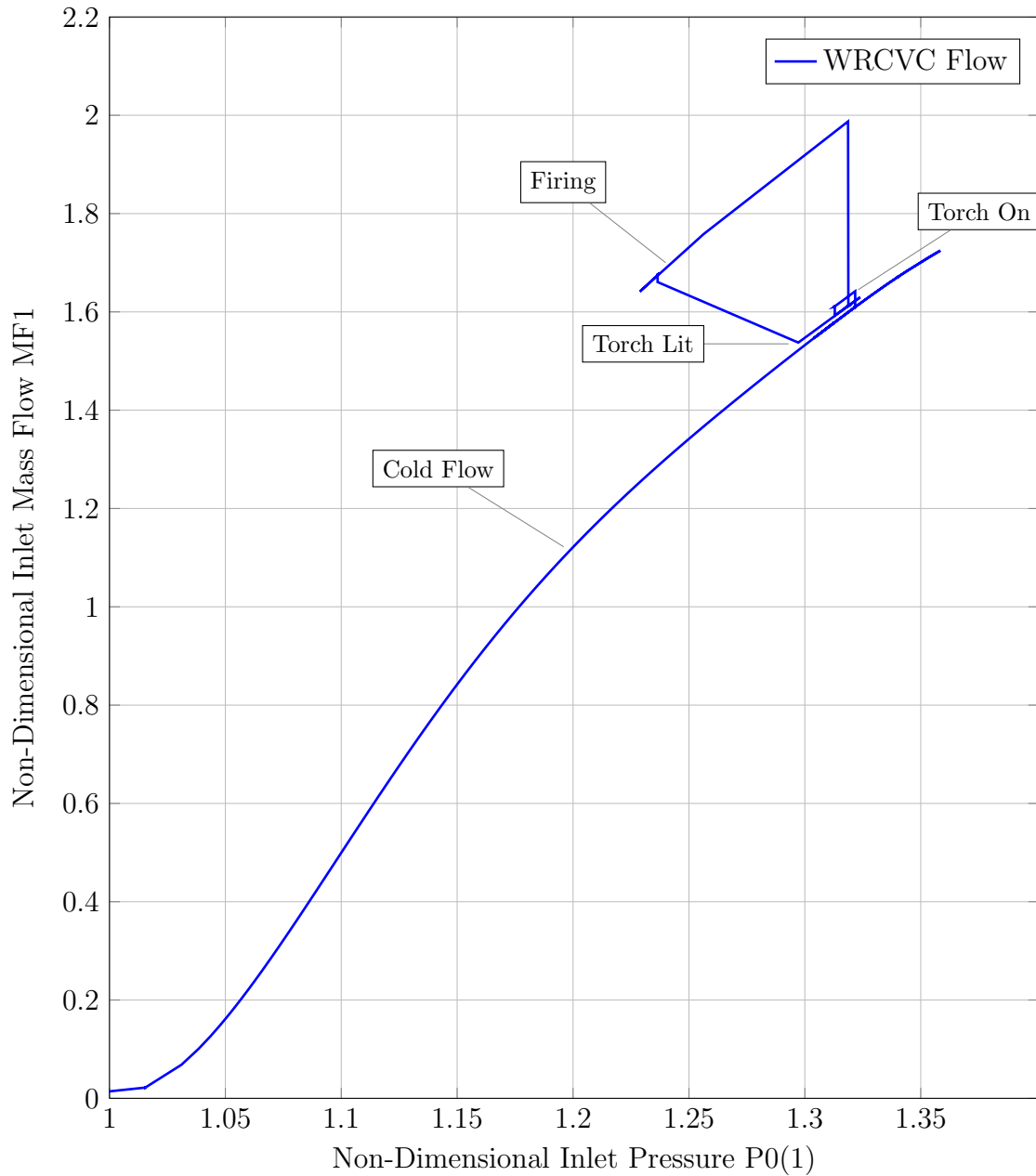


Figure 5.26. VOLDYN computation of flow vs inlet pressure.

6. CONCLUSIONS

The overall purpose of this thesis was to present a time-dependent lumped volume computer simulation of the WRCVC rig, in an attempt to explain the pressure loss mechanisms seen in the inlet section, and to show the dynamic pressure variation caused by shifting of the WRCVC pressure-flow characteristic during the combustion sequence.

The SCW1D computer program is a computer model used for computation of wave rotor cycles, and has been used to compute the base operating points for the WRCVC. As part of this thesis, the program was modified to allow a sweep of the inlet pressures, from low to high values, as needed by the user. The capability to vary inlet pressure without stopping the program made it possible to rapidly generate pressure versus flow characteristics for each of the WRCVC's four main operating conditions. In addition the SCW1D program was modified to be capable of insertion into a driver program as a subroutine for more detailed studies.

The VOLDYN computer program is an original work of this thesis. It was developed in Fortran 90 using a lumped single volume representation of the WRCVC rig's upstream inlet section, modeling the main air system, the fuel delivery system, and coupling the pressure versus flow characteristics generated by the SCW1D program. The VOLDYN program very closely simulated both the pressure loss mechanisms in the inlet section and accurately simulated the dynamic response of that hardware to mass addition and changes in the WRCVC operating condition.

The VOLDYN computed pressure losses across the fuel nozzles are significant, and consist mostly of the pressure drag caused by the nozzles themselves blocking the flow. An additional loss during fuel delivery was computed, caused by cross flow mass addition. A small pressure loss was also computed based on friction drag of the inlet guide vanes and the flow straightener walls. These losses bring the WRCVC rotor inlet pressure down to the flow characteristic intersection at the set mass flow rate. Comparisons were made between the computed flow and pressure values and the measurements from the rig's data reduction system. For the cold flow segment of the test sequence, the differences between computed and measured values were very small, indicating the VOLDYN computer model was accurately predicting the pressure losses in the inlet section. These differences were higher during and after the torch lighting sequence and during the firing sequence. For the spark lighting sequence, all of the pressure measurements were seen to decrease, and so the data in this time period were assumed to be inaccurate due to this electrical noise. For the firing (combustion) sequence, the WRCVC rotor speed decreased approximately 2 percent. The related shift in the WRCVC pressure-flow characteristic was not sufficient to explain the decrease in measured pressure at the fuel delivery station.

The combination of the VOLDYN program and the SCW1D program can be a valuable tool for studying the WRCVC rig and for future planning of WRCVC testing for IUPUI, the Purdue Zucrow Laboratories and Rolls Royce LibertyWorks. Since the pressure losses across the fuel system are significant for this hardware, it will be important to estimate those pressure losses in order to accurately determine the expected operating condition of the WRCVC during testing. Accurate prediction of the WRCVC performance will facilitate determination of fuel nozzle placement and fuel fraction needed for future test cases.

One recommendation is to modify the VOLDYN program to fully integrate the SCW1D program into it, so that a full dynamic simulation can be run. This will be important for any future dynamic testing, for control system studies, and for startup transient planning. Documentation and training for use of the program will also help transfer this technology to future IUPUI graduate students and Rolls Royce LibertyWorks engineers.

LIST OF REFERENCES

LIST OF REFERENCES

- [1] B. Alparslan, M.R. Nalim, and P.H. Snyder, "Wave Rotor Combustor Test Rig Preliminary Design", in *Proceedings of IMECE2004 - 2004 ASME International Mechanical Engineering Congress and Exposition*, pp. 177-185, Anaheim, California, November 13-19, 2004.
- [2] Y. Matsutomi, C. Hein, C. Lian, S. Meyer, C. Merkle, and S. Heister, "Facility Development for Testing of Wave Rotor Combustion Rig", AISS-2007-5052, *43rd AIAA/ASME/SAE/ASEE Joint Propulsion Conference and Exhibit*, Cincinnati, Ohio, July 8-11, 2007.
- [3] T.M. Elharis, S.D. Wijeyakulasuriya, and M.R. Nalim, "Wave Rotor Combustor Aerothermodynamic Design and Model Validation based on Initial Testing", *46th AIAA/ASME/SAE/ASEE Joint Propulsion Conference and Exhibit*, Nashville, Tennessee, July 25-28, 2010.
- [4] Y. Matsutomi, S.E. Meyer, S. Wijeyakulasuriya, I. Zuhair, M.R. Nalim, M. Shimo, M. Kowalkowski, and P.H. Snyder, "Experimental Investigation on the Wave Rotor Constant Volume Combustor", *46th AIAA/ASME/SAE/ASEE Joint Propulsion Conference and Exhibit*, Nashville, Tennessee, July 25-28, 2010.
- [5] T.M. Elharis, S.D. Wijeyakulasuriya, M.R. Nalim, and Y. Matsutomi, "Analysis of Deflagrative Combustion in a Wave-Rotor Constant-Volume Combustor", *49th AIAA Aerospace Sciences Meeting including the New Horizons Forum and Aerospace Exposition*, AIAA-2011-583, Orlando, Florida, January 4-7, 2011.
- [6] National Museum of the Air Force. Available from <http://www.nationalmuseum.af.mil/shared/media/photodb/photos/070105-F-1234S-003.jpg>. Last accessed November 2011.
- [7] C.C. Graves, "Effect of Oxygen concentration of the inlet Oxygen-Nitrogen mixture on the combustion efficiency of a single J33 turbojet combustor". NACA RM E52F13, 1952: Lewis Flight Propulsion Laboratory, Cleveland, Ohio, August, 1952.
- [8] National Museum of the Air Force. Available from <http://www.nationalmuseum.af.mil/shared/media/photodb/photos/060829-F-1234S-023.jpg>. Last accessed November 2011.
- [9] E.V. Zettle, C.T. Norgren, and H. Mack, "Combustion performance of two experimental turbojet annular combustors at conditions simulating high-altitude supersonic flight", NACA RM E54A15, 1954: Lewis Flight Propulsion Laboratory, Cleveland, Ohio, March, 1954.

- [10] H. Li, P. Akbari, and M.R. Nalim *Air-Standard Aerothermodynamic Analysis of Gas Turbine Engines With Wave Rotor Combustion*. Journal of Engineering for Gas Turbines and Power, Volume 131, Issue 5, 054506, September 2009.
- [11] M.R. Nalim, "Thermodynamic Limits of Work and Pressure Gain in Combustion and Evaporation Processes", *Journal of Propulsion and Power*, Vol. 18, No. 6, November-December 2002, pp 1176-1182.
- [12] P. Akbari, M.R. Nalim, and N. Mueller, "A Review of Wave Rotor Technology and its Applications", *Journal of Engineering for Gas Turbines and Power*, October 2006, Vol 128, pp 717-735.
- [13] D. E. Paxson, "A General Numerical Model for Wave Rotor Analysis", NASA Technical Memorandum 105740, Lewis Research Center, Cleveland, Ohio, July 1992.
- [14] D.E. Paxson and J. Wilson, "An Improved Numerical Model for Wave Rotor Design and Analysis", in *31st Aerospace Sciences Meeting and Exhibit*, Reno, Nevada, January 11-14, 1993.
- [15] D.E. Paxson, "A Numerical Model for Dynamic Wave Rotor Analysis", in *31st AIAA/ASME/SAE/ASEE Joint Propulsion Conference and Exhibit*, San Diego, California, July 10-12, 1995.
- [16] D.E. Paxson, "Comparison Between Numerically Modeled and Experimentally Measured Wave-Rotor Loss Mechanisms", *Journal of Propulsion and Power*, Vol 11., No. 5, September-October 1995, pp 908-914.
- [17] D. E. Paxson, "Numerical Simulation of Dynamic Wave Rotor Performance", *Journal of Propulsion and Power*, Vol 12., No. 5, September-October 1996, pp 949-957.
- [18] M.R. Nalim and D.E. Paxson, "A Numerical Investigation of Premixed Combustion in Wave Rotors", in *41st Gas Turbine and Aeroengine Congress and Exhibition*, June 10-13, 1996, Birmingham, United Kingdom.
- [19] T. Elharis, *A Multi-Step Reaction Model for Stratified-Charge Combustion in Wave Rotors* Master's Thesis, School of Mechanical Engineering, Purdue University, May 2011.
- [20] C.K. Drummond and P.J. Ouzts, "Real-Time Simulation of an F110/STOVL Turbofan Engine", NASA TM-102409, Lewis Research Center, Cleveland, Ohio, 1989 prepared for the Central/Northeastern ADIUS Conference, Cleveland, Ohio, October 16-17, 1989.
- [21] S. M. Jones, "An Introduction to Thermodynamic Performance Analysis of Aircraft Gas Turbine Engine Cycles Using the Numerical Propulsion System Simulation Code", NASA TM 2007-214690, Glenn Research Center, Cleveland, Ohio, March 2007.
- [22] S. F. Hoerner, *Fluid-Dynamic Drag. Practical Information on Aerodynamic Drag and Hydrodynamic Resistance*. 2nd ed., Published by the Author. Brick Town, New Jersey, 1965.

- [23] F.P. Incropera, D.P. DeWitt, T.L. Bergman, and A.S. Lavine, *Fundamentals of Heat and Mass Transfer*. 6th ed., John Wiley & Sons, Hoboken, New Jersey, 2007.
- [24] M. J. Zucrow, and J. D. Hoffman, *Gas Dynamics, vol 1* John Wiley & Sons, Hoboken, New Jersey, 1976.
- [25] J. D. Hoffman, *Numerical Methods for Engineers and Scientists* McGraw Hill, 1992.
- [26] Z. Lightner, Wave Rotor Review and Cold Flow Analysis ME491 Review Paper, Nov 2007. (Summarized in Appendix B)
- [27] J.H. Keenan, J. Chao, and J. Kaye, *Gas Tables, International Edition*. Second Edition (SI Units), Krieger Publishing Company, Malabar, Florida, 1992.
- [28] GNU Fortran 77 (g77) Legacy Site <http://www.kilmnj.com/g77>. Last accessed November 2011.
- [29] GCC, the GNU Compiler Collection <http://gcc.gnu.org/>. Last accessed November 2011.
- [30] D. E. Paxson, "A Numerical Investigation of the Startup Transient in a Wave Rotor Performance", *ASME Journal of Engineering for Gas Turbines and Power*, Vol. 119, No. 3, 1997, pp. 676-682.

APPENDICES

A. EXAM51 COMPUTER PROGRAM LISTING

```

PROGRAM EXAM51
IMPLICIT DOUBLE PRECISION (A-H,O-Z)
IMPLICIT INTEGER (I-K,M-N)
IMPLICIT LOGICAL (L)
DATA ZERO,ONE/0.0D0,1.0D0/
C
C   Example 5.1 from ME500 curriculum
C
VOL=0.15
P1=2.0 * 100000.0
WRITE(6,*) 'P1_=_',P1
PFINAL = 4.0 * 100000.0
TT1=300.0
WRITE(6,*) 'TT1_=_',TT1
CV1=AIRCV(TT1)
CP1=AIRCP(TT1)
GAM1=CP1/CV1
U1=TT1*CV1
R=287.0
TTANK=321.4
CPTANK=AIRCP(TTANK)
HTANK=TTANK*CPTANK
AM1=(P1*VOL)/(R*TT1)
WRITE(6,*) 'AM1_=_',AM1
C
C   Arbitrarily choose a mass flow
C   Choosing 0.01 kg/sec so that it should
C   take approx 23.3 seconds to fill the tank
C
AMDOT1=0.01
C
C   Start the iteration
C
TIME=0.0
DT=0.0001
TT1=300.0
CV1=AIRCV(TT1)

```

```

CP1=AIRCP(TT1)
HT1=TT1*CP1
AM2=AM1
U2=U1
P2=P1
RHO2=AM2/VOL
GAM2=GAM1
AMDOTF=0.0
CPF=CP1
TTF=TT1
AMDOT5=0.0
CP5=CP1
TT5=TT1
NITER=0
DO WHILE(P2 .LT. PFINAL)

```

```

C
C
C
C
C
C
C

```

Equations used **in** the volume dynamic model

```

drho=(mdot1+mdotf-mdot5)*(dt/volume)
rho2p1=rho2+drho

```

```

DRHO=(AMDOT1+AMDOTF-AMDOT5)*(DT/VOL)
RHO2=RHO2+DRHO
AM2=RHO2*VOL

```

```

C   WRITE(6,*) 'DRHO=',DRHO
C   WRITE(6,*) 'RHO2=',RHO2
C   WRITE(6,*) 'AM2=',AM2
C   GO TO 10

```

```

C
C
C
C
C
C
C

```

Equations used **in** the volume dynamic model

```

dp=((gam-one)/volume)*(mdot1*cp1*tt0+
1 mdotf*cpf*ttfuel-mdot5*cp2*tt5)*dt/(g1*g1)

```

```

ps2p1=ps2+dp

```

```

DP=((GAM2-ONE)/VOL)*(AMDOT1*(CPTANK*1000.0)*TTANK+
1 AMDOTF*(CPF*1000.0)*TTF-AMDOT5*(CP5*1000.0)*TT5)*DT
P2=P2+DP

```

```

C   AM1=(P1*VOL)/(R*T1)
C   T2=(P2*VOL)/(R*AM2)
C   CP2=AIRCP(T2)
C   CV2=AIRCV(T2)

```

```
GAM2=CP2/CV2
TIME=TIME+DT
NITER=NITER+1
IF (MOD(NITER,1000).EQ.1) THEN
  WRITE(6,100) TIME, AM2, RHO2, (P2*0.001), T2
100  FORMAT(F14.3, F14.6, F14.6, F14.4, F14.3)
  END IF
END DO
WRITE(6,100) TIME, AM2, RHO2, (P2*0.001), T2
10 STOP
END
FUNCTION AIRCP(T)
AIRCP=((5.6294298E-08*T) - 2.3548591E-05)*T + 1.0034327
RETURN
END
FUNCTION AIRCV(T)
AIRCV=((5.6013567E-08*T) - 2.3270886E-05)*T + 7.1634137E-01
RETURN
END
```

B. SUMMARY OF Z. LIGHTNER REFERENCE PAPER

The following is a summary of an unpublished paper by Zach Lightner, part of an ME491 Project, titled “Wave Rotor Review and Cold Flow Analysis”.

ABSTRACT

Conventional turbomachinery utilizing steady flow and constant pressure combustion has dominated the propulsion and power generation industries. However, limitations of materials to withstand higher temperatures have dramatically reduced recent improvements to this technology. Alternative technologies are currently being researched by major aerospace firms, including non-steady flow devices. It has been known since the early 19th century that unsteady flow devices are inherently more efficient thermodynamically than steady flow devices. With the major advancements in CFD over the last two decades, unsteady flow can now be predicted and analyzed, providing a real, viable option for future power generation. Examples of non-steady flow devices are shock tubes, pulse detonation engines (PDE), and wave rotors.

EXPERIMENTAL RESULTS AND DISCUSSION

The non-dimensional inlet mass flows evaluated at each rotational speed and pressure ratio by the Q1D code are shown in Table 7. Using the methods described above, the values were converted into actual mass flow rates in lbm/sec., as shown in Table 8. A plot of the preceding table is shown in Figure 12.

Table B.1 Table 7: Non-dimensional mass flow rates.

	Inlet	Pressure	(psia)					
RPM	24.5	22.6	21.0	19.6	18.4	17.3	16.3	15.5
2000	1.741	1.669	1.585	1.489	1.373	1.219	0.952	0.521
2500	1.362	1.303	1.228	1.138	1.037	0.911	0.757	0.525
3000	1.064	1.030	0.983	0.912	0.824	0.718	0.589	0.445
3500	0.822	0.781	0.728	0.669	0.601	0.500	0.365	0.216
4000	0.724	0.703	0.678	0.643	0.591	0.520	0.425	0.284
4500	0.518	0.474	0.425	0.374	0.317	0.254	0.198	0.145

Table B.2 Table 8: Actual mass flow rates in lbm/sec.

	Inlet	Pressure	(psia)					
RPM	24.5	22.6	21.0	19.6	18.4	17.3	16.3	15.5
2000	16.3106	14.4333	12.7278	11.1598	9.6473	8.0614	5.9459	3.0827
2500	15.9499	14.0852	12.3263	10.6614	9.1080	7.5307	5.9100	3.8830
3000	14.9522	13.3610	11.8405	10.2529	8.6846	7.1223	5.5181	3.9496
3500	13.4767	11.8195	10.2305	8.7746	7.3900	5.7865	3.9894	2.2366
4000	13.5657	12.1589	10.8889	9.6384	8.3052	6.8776	5.3088	3.3608
4500	10.9190	9.2230	7.6789	6.3069	5.0116	3.7794	2.7825	1.9304

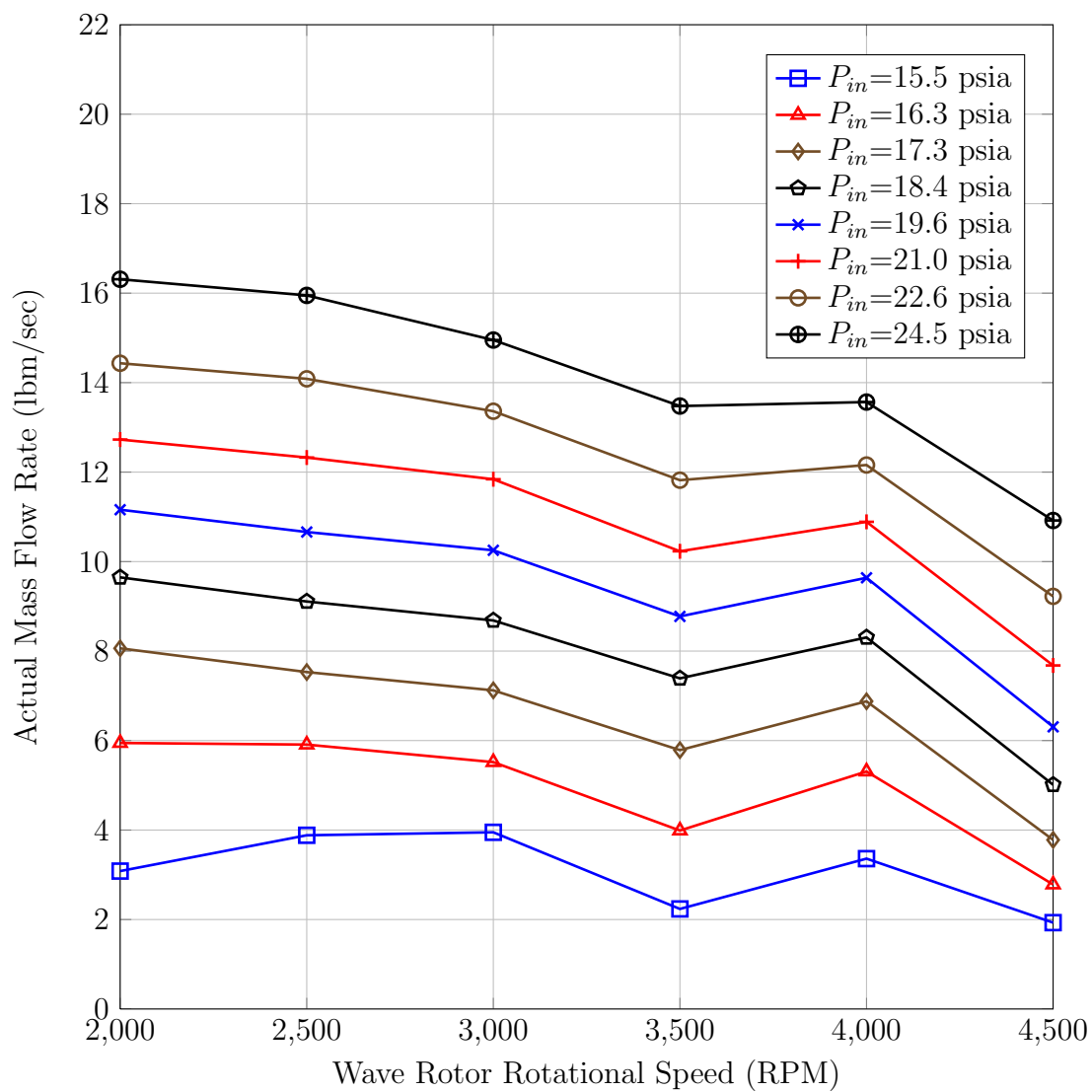


Figure B.1. Figure 12: Channel mass flow for various pressure ratios.

VITA

VITA

Keith C Smith was born in Columbus, Ohio. After completing his work at Walnut Ridge High School, Columbus, Ohio, in 1975, he entered Lincoln Technical Institute in Indianapolis, Indiana, graduating in 1976 with a Certificate in Diesel Truck Technology. After working three years for Cummins Ohio, he attended Purdue University in West Lafayette, Indiana, winning a General Motors Scholarship with Allison Engine Company, and graduating in 1982 with a Bachelor of Science in Mechanical Engineering.

Keith worked for 15 years in the Aerospace industry, starting in 1982 with McDonnell Aircraft in St. Louis, Missouri, specializing in advanced propulsion system design, aircraft mission analysis, and aircraft/engine integration. While there he co-authored AIAA-84-2398 "Techniques to reduce exhaust gas ingestion for vectored-thrust V/S-TOVL aircraft". In 1985 he joined the Aerothermal Methods group at GE Aircraft Engines in Evendale, Ohio, and co-developed a full stall simulation of the XF120 core compressor which correlated with high frequency time series test data in both rotating stall and surge events. This technology was used in the development of the YF120 dual cycle engine used in the YF-22 Raptor demonstrator. In 1992 he joined Allison Engine Company in Indianapolis, Indiana, as a Test Engineer, designing and developing test instrumentation for Allison's full line of engines. Later he joined the Test Electronics group after the sale of Allison to Rolls Royce and developed automated test cells and other projects.

In 1997 Keith joined the International Projects team at Delphi Automotive in Kokomo, Indiana, as a Software Technical Lead, and lead the development of demonstrator and prototype powertrain control units for Toyota products. From Delphi to Thomson Consumer Electronics to Roche Diagnostics, Keith has contributed to many project teams in the areas of software development, systems integration, project

management, and sales. He currently is a Principal Systems Analyst for the Midwest ISO, an independent, non-profit company which ensures the reliability of, and access to, the high voltage power grid for the Midwest.

This thesis was typed in its entirety, excepting quoted portions, by the author, and typeset using LaTeX and the puthesis template.